PhD-FSTM-2022-002

The Faculty of Science, Technology and Medicine

DISSERTATION

Defence held on 17/01/2022 in Luxembourg

to obtain the degree of

DOCTEUR DE L'UNIVERSITÉ DU LUXEMBOURG

EN Sciences de l'Ingénieur

by

Karthik MATHIVANAN

Born on 05 August 1991 in Vellore, Tamil Nadu (India)

LASER FUSION WELDING OF CU TO AL WITH SPIRAL TRAJECTORY AND MONITORING OF PROCESS SIGNALS

Dissertation defence committee

Prof. Dr Peter PLAPPER, dissertation supervisor
Professor, Université du Luxembourg

Prof. Dr Stefan KAIERLE
Executive Director, Laser Zentrum Hannover e.V.
Professor, Leibniz University, Hannover

Prof. Dr Stefan MAAS, Chairman
Professor, Université du Luxembourg

Prof. Dr Konrad WEGENER
Professor, ETH Zurich

Prof. Dr Slawomir KEDZIORA, Vice Chairman
Professor, Université du Luxembourg

Acknowledgement

The presented thesis is a result of my research work at the University of Luxembourg on Laser welding of Cu and Al. Although the journey was challenging it gave me valuable experience and will be useful in my future career. As a doctoral candidate, I had the opportunity to learn, present and publish my research study which was very rewarding. Firstly, I would like to thank Prof. Plapper for giving me the opportunity to pursue PhD on laser welding. I would also like to thank all the jury members Prof. Maas, Prof. Kedziora, Prof. Kaierle and Prof. Wegener for reviewing and evaluating my work. I would also like to extend my thanks to Prof. Greger who was my CET member for reviewing my work and providing valuable comments.

The collaboration with Luxembourg Institute of Science and Technology (LIST) to do perform self analysis and measurements using SEM-EDS was greatly helpful during my study. I would also like to thank Michael Engstler Group leader Advanced Microstructure Characterization, Chair of Functional Materials, Saarland University" for SEM-EDS measurements in the beginning of my PhD. I would like to thank Dr. Gunter Amborosy from TRUMPF, Ditzingen for providing access to welding trials with the green laser system (515 nm disk laser) in 2019.

I would like to thank all my colleagues at the University of Luxembourg for the support and advises. Especially, the research study with Pascal resulted in best paper award for publication in Metallography, Microstructure, and Analysis. I must also acknowledge the experience of supervising and working with bachelor and masters students (Fanni, Christian fry, Charel, Nithesh, Steven, Shiva, Hossein and Pierre).

Lastly, I am very grateful to my lovely wife, parents and sister to receive much needed support throughout my PhD. Without them my PhD journey would have been very difficult.

Abstract

Welding of Aluminium (Al) and Copper (Cu) in a dissimilar fashion is required for the manufacturing of solar thermal absorbers, battery modules and refrigeration applications. The high strength, thermal and electrical conductivity of Cu combined with the lightweight property of Al material enable the high performance of the product. A laser is a precise tool, which can increase the productivity and quality of the welding process. Welding Al and Cu is considered difficult because of the formation of complex intermetallic phases which reduce the strength of the joint. Laser brazing from low melting Al sheet to Cu sheet is the traditional technique to reduce the intermetallic phases. This thesis focuses on irradiation of laser beam from copper sheet to aluminium sheet in overlapped configuration. The approach is to form a large amount of intermixing to obtain (Cu) solid solution and Al-rich phase $Al + Al_2Cu$ in the interface. By this approach, it was found that a fusion zone with a large number of good phases was formed. The intermetallic compounds $Al_2Cu, Al_3Cu_4, Al_4Cu_9$ are intermixed and small. Such a microstructure is beneficial for joint strength. The characterization was done by light optical microscopy and scanning electron microscope. EDS analysis was used to estimate the composition and identify the phases. It was found that a beneficial Cu solid solution phase is present in the joint.

To qualify the joint and identify the weld status, melting characteristics during laser welding by observation of the optical emission in Ultraviolet-visible wavelength was studied. The Al melting peak at 396 nm and Cu melting peak at 578 nm was found to correlate to the welding process parameters. The signals correlate to the actual melting of Cu and Al sheets, which was investigated by the cross-sectional images and the weld images on the top of the Cu-Al weld. Therefore, the possibility for real-time analysis to identify different welding conditions is shown.

Abbreviation

Al: Aluminium

Cu: Copper

IMC: Intermetallic compound

Al-Cu : Aluminium-Copper joint

HAZ: Heat affected zone

FZ: Fusion zone

LOM: Light optical microscope

SEM: Scanning electron microscope

EDS: Energy Dispersive X-Ray Spectroscopy

UV: Ultraviolet

IR: Infrared

CNN: Convolutional neural network model

RGB: Red green blue

Contents

List of Figures

List of Tables

Chapter 1

Introduction

The joining of dissimilar metals together is highly desired in the automotive industry for lightweight construction and high performance. In particular welding of Aluminium (Al) to Copper (Cu) [14], Al to steel [88], Cu to Steel [58] and Al to magnesium [35] is increasingly used. One of the main applications of Al to Cu joints is in the manufacturing of batteries. Electrification of automobiles is the future of transportation to tackle pollution and global warming. Projections are that by 2030, global electric vehicles sales will reach 23 million and the automotive industry is already transforming from an internal combustion engine to electric drive technology. The key to successful electric vehicle technology is battery development, for the storage of electricity [10, 74]. A schematic of the main parts of the electric drive is shown in the figure 1.1.

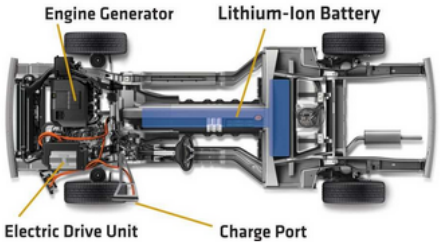

Figure 1.1: Schematic of electric car [74]

Lithium-ion battery (Li-Ion) plays a very important role in the electrification of the automotive sector. The cells used are often equipped with two conductors made of copper and aluminium for anode and cathode respectively. Li-Ion battery requires several connections of highly conductive Al, Cu bus bars to be joined to the electrode cell ends of the battery. Multiple such cells are interconnected to form a battery pack as shown in the figure 1.3. The simplest method to connect

such combinations in a battery is by mechanical screwing or bolts as shown in figure 1.2. But the mechanical fastening technique is obsolete as it adds more to the weight of the battery and is already replaced with other joining processes such as laser beam welding (LBW), friction stir welding (FSW), ultrasonic welding (USW) and resistance spot welding (RSW) [22, 53, 84].

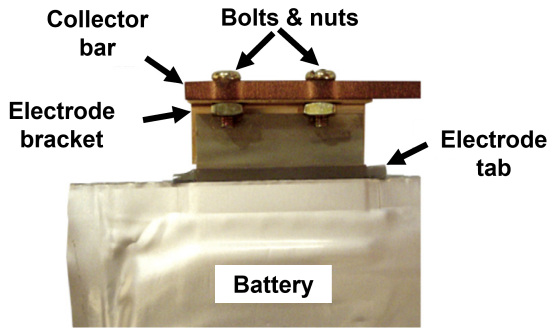

Figure 1.2: Bolted connections in the battery to join copper collector to electrode [102]

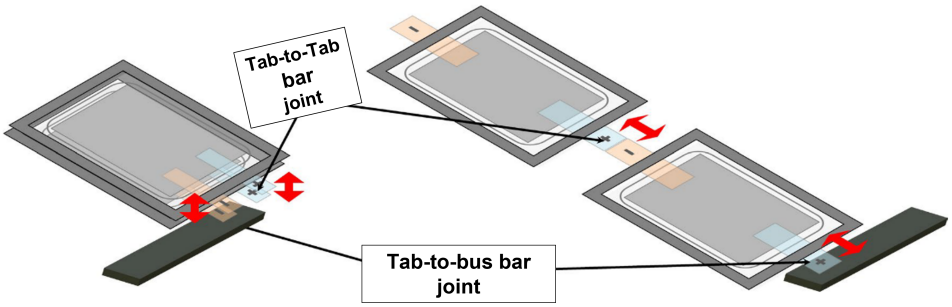

Figure 1.3: Al and Cu connections for battery packs [23]

The USW is one of the common joining techniques used for battery production which utilizes high-frequency ultrasonic vibration, typically 20 kHz or above to join the substrate by creating solid-state bonds by applying clamping pressure. However, the technique is not suitable for terminal-to-busbar joints of the pouch cells because the applied pressure damages the structural integrity. The resistance spot welding (RSW) is challenging for Al and Cu joining due to the high electrical and thermal conductivity as the RSW works on the principle of electrical resistance at the mating surfaces to create localized heating and fusion of materials under pressure.

Ultrasonic welding and laser welding have a high potential for welding dissimilar materials [44]. Laser welding is characterized by localized energy delivery, high precision and high throughput[14,

78]. Laser technology is preferred for welding Cu and Al as it is contactless, has high processing speed, reasonable quality of joint and is highly autonomous for production lines.

This thesis focuses on the analysis of the laser welding process for overlapped copper and aluminium sheets. Copper and aluminium connections are required not only in automotive batteries but also in solar cells and the refrigeration industry where copper tubes are joined to aluminium tubes. In general joining, dissimilar materials are essential for a complex product design and superior performance of a product. The motivation of using dissimilar metals in a product is to combine the advantages from either of the materials. Utilization of new metal alloys or dissimilar metal combinations requires suitable joining techniques.

In addition to the precise control of heat input, the laser beam can be applied to the material at high speeds in the range of 300 mm/s with different trajectory motions, thereby giving design flexibility. The main concern with using laser for dissimilar metal welding is that it is a thermal process, which involves melting, and eventual intermixing of the two base metals. In laser processing, the absorption of laser radiation by the metal is essential. Each metallic surface has a different absorption coefficient for laser radiation, which is very critical. For such a thermal process, the metallurgical incompatibility of Al and Cu results in intermetallic phases that are brittle. Hence, the resulting joint is brittle with reduced mechanical strength and increased electrical resistance. In this thesis, Cu and Al are joined by irradiation of laser beam from the copper sheet placed on top of the Aluminium sheet and joined by fusion of the molten Cu and Al metals together rather than brazing. Early works in laser joining of Al and Cu sheets focused on irradiating the laser beam on the Al sheet, since the melting of Al sheet (660 °C) is easier in comparison to Cu sheet (1080 °C). However, for design flexibility, irradiation of laser beam from either side of the metals is required i.e., flexibility in selecting Aluminium or Copper sheet to be placed on the top. But only limited literature exists on welding from the Cu side. With the availability of high power Near-Infrared lasers, very high intensity of 10^7 W/cm^2 provides sufficient energy to melt the Cu sheet. In this thesis, the Cu is selected as the top sheet to melt to take advantage of the higher solubility of Al in Cu. The laser beam is moved in a spiral trajectory resembling a spot weld and analogous to the bolted connection (as shown in the figure 1.2) in contrast to linear welding or line welds. Therefore this approach can be a replacement in applications where a circular weld profile like a bolted joint is desired. The chosen profile can be considered similar to spot welding processes and it is a very good alternative to spot welds performed with RSW and USW.

For Cu-Al welds and dissimilar metal joining, analysis of the joint quality and indication of the welding status is required by the industry. Very sparse literature addresses the methodology for fast and non-destructive analysis. This thesis proposes using weld images to predict a strong or a

weak joint which is a non-destructive technique. Furthermore, an artificial neural network model is presented to predict the welding status for automatic quality inspection. In addition, real-time analysis of the signal is presented to identify the excessive melting of Al during the welding process which is used to qualify the welds, i.e., strong or weak weld.

In this research work, industrial requirements such as flexible joint configuration, reliable inexpensive quality analysis techniques are addressed for Cu and Al welding. The flow chart in figure 1.4 shows the organization of the thesis in different chapters.

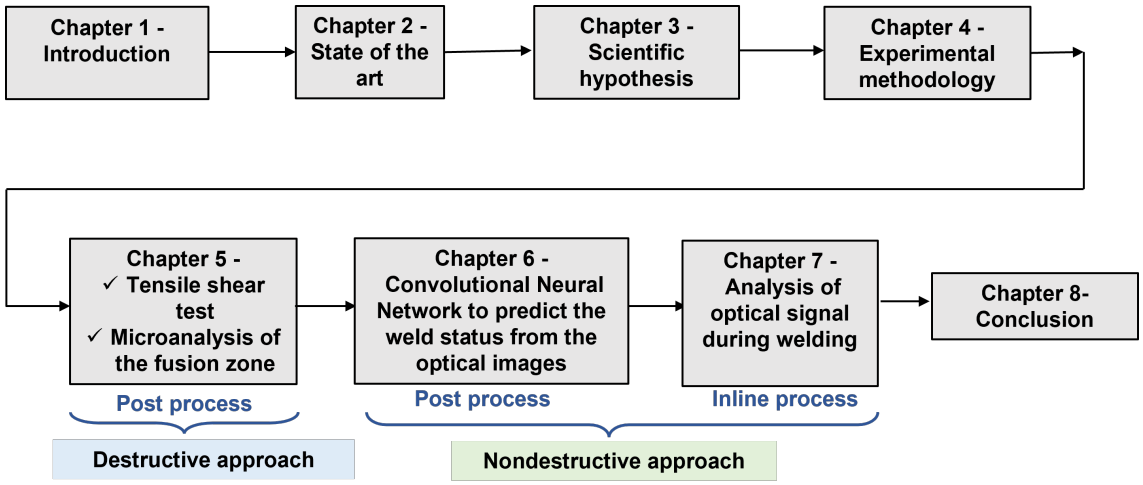

Figure 1.4: Flow chart showing the structure of the thesis

This thesis is organized as follows, the discussion concerning laser-metal interaction is discussed in Chapter 2. The challenges from the metallurgy and laser processing perspective are discussed. This section also summarizes the laser welding research of dissimilar aluminium and copper. The chapter 3 outlines the research gap and the scientific hypothesis of the thesis. The experimental methodology and approaches for the welding process and analysis techniques for microscopy are explained in chapter 4. The experimental results of the tensile shear test welded with spiral trajectory are discussed in chapter 5. This chapter includes the microstructural analysis and the chemical composition estimation in the joint, which are performed by destructing the samples after the welding process i.e, post-welding process and destructive analysis. The analysis of the Cu-Al weld images acquired from the top of Cu and the CNN (Convolutional neural network model) model to predict the welding status is presented in chapter 6. The weld images in this chapter are classified based on the experimental results from the chapter 5. The trained CNN model can be implemented after the welding and is a non-destructive analysis (post-process and non-destructive). The process analysis using photodiodes for Cu-Al welding and the correlation of the signals to the welding status is presented in chapter 7. The technique proposed in this chapter can be performed in real-time and is

a non-destructive analysis (Inline process analysis and non-destructive). Finally, the summary and future works are described in chapter 8 and chapter 9 respectively.

Chapter 2

State of the art

In this section, the laser welding process-related information is discussed starting with the issues from the metallurgical perspective which is the central problem of joining this combination and the discussion extends to the laser-material interaction.

2.1 Welding of Aluminium - Copper

Copper and Aluminium is widely used for their superior electrical conductivity and thermal properties. Some of the applications are in aerospace and automotive parts (weight reduction), electrical and electronic components e.g. battery connections requires joining Al, Cu, Ni. Other industries that require this material are sensors and automation systems. Some material considerations are density, electrical conductivity, thermal conductivity, yield strength, melting point and thermal diffusivity. The thermal joining of metals typically results in the formation of distinct regions or zones such as fusion zone, heat affected zone (HAZ), defects like pores, undercut as shown in figure 2.1.

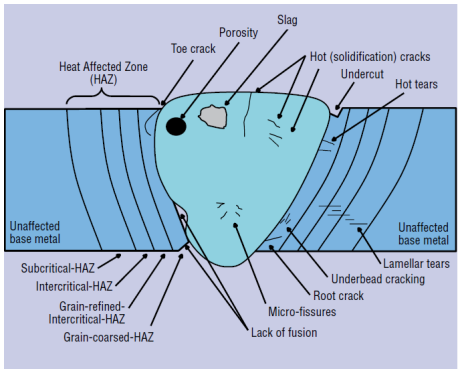

Figure 2.1: Regions in the thermal joining of metals [16]

The HAZ is the region that did not undergo melting but is affected by the heat from the joining process. Beyond the HAZ is the unaffected base metal. The fusion zone is the region where the melting of the base material and solidification occur for a joint. The fusion zone can be classified as autogenous, homogeneous and heterogeneous depending on whether or not a filler metal is used and the composition of the filler metal with respect to the base material [57].

Autogenous weld:

Autogenous welds are those where no filler metal is added and the fusion zone is formed by the melting and resolidification of the base metals. The composition of the fusion zone is essentially the same as the base metal, except for possible losses due to evaporation or pickup of gases from the shielding atmosphere. Not all materials can be joined autogenously because of weldability issues.

Homogenous weld:

Homogenous welds involve the use of a filler metal that closely matches the base metal composition. This type of fusion zone is used when the application requires that filler and base metal properties must be closely matched.

Heterogeneous weld:

Heterogeneous welds are fusion welds made with filler metals whose composition is different from that of the base metal. In many situations, matching filler metals may not exist or the weld properties desired may not be achievable with a matching composition. it should also be recognized that many base metal compositions may have inherently poor weldability and that dissimilar filler metals are required to achieve acceptable properties or service performance. Some considerations that would require the use of a dissimilar composition filler metal include strength, weld defect formation (e.g., porosity), weldability/solidification cracking resistance, heat treatment response, corrosion resistance, filler metal cost, and operating characteristics of the consumable.

The thermal joining of Al to Cu leads to the heterogeneous weld fusion zone as dissimilar metals are fused in the weld zone. This results in the formation of intermetallic compounds that are brittle. Welding of dissimilar materials can introduce a number of defects caused by the difference in mechanical and physical properties. One of the most serious involves the formation of intermetallic compounds in the fusion zone which can lead to microcracking. Figure 2.2 shows a microweld between copper and aluminium showing microcracks in the fusion zone.

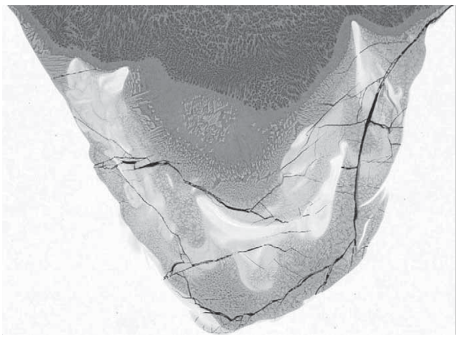

Figure 2.2: SEM micrograph of the root of the weld between aluminium alloy and pure copper. This shows the formation of intermetallic compounds in the fusion zone leading to microcracking [90]

2.2 Al-Cu intermetallic compounds

The Al-Cu intermetallic compounds formed are non-metallic covalent bonds, which are brittle and highly resistive to electric current[70]. The formation of such compounds is due to the solubility issues of Al and Cu which are described by Hume-Rothery rules [15]. The rule describes that the formation of complex compounds is due to large differences in the atomic radii, type of crystal structure, number of valance electrons and the electronegativity between the metals. The Solubility map for Al based on the electronegativity and atomic radii is given by the Darken-Gurry map (figure 2.3). The solubility of elements within the first ellipse is higher and as it gets farther outside of the ellipse, the solubility is poor. As can be seen in figure 2.3, copper is one of the farthest elements for Al. This describes the metallurgical incompatibility between the Al and Cu metals.

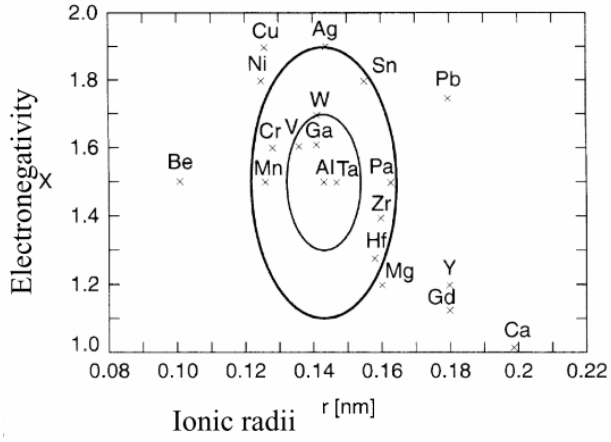

Figure 2.3: Darken-Gurry map for Al [4]

The approaches for joining the Al and Cu are based on controlling the depth, amount of in-

termetallic phases by different process and oscillation techniques [96, 97, 30, 87]. Alternatively, researchers have also shown that the use of interlayers or additional elements such as nickel can mitigate the formation of brittle IMC (intermetallic compounds) in many dissimilar material systems [111, 91, 7]. Aluminium and copper alloys are potential materials used in electrical and electronic applications, so numerous studies on joining them together (dissimilar material welding) by different techniques have been undertaken. The key problem with all dissimilar metal joining techniques for Al to Cu is the easy formation of intermetallic compounds. The formation of hard and brittle IMCs have a detrimental effect on joint strength. Using a solid-state process such as friction stir welding and ultrasonic welding improves the IMC variety and distribution. Other techniques are to reduce the reaction of Al and Cu by applying less energy to increase the Cu/Al strength [68, 39].

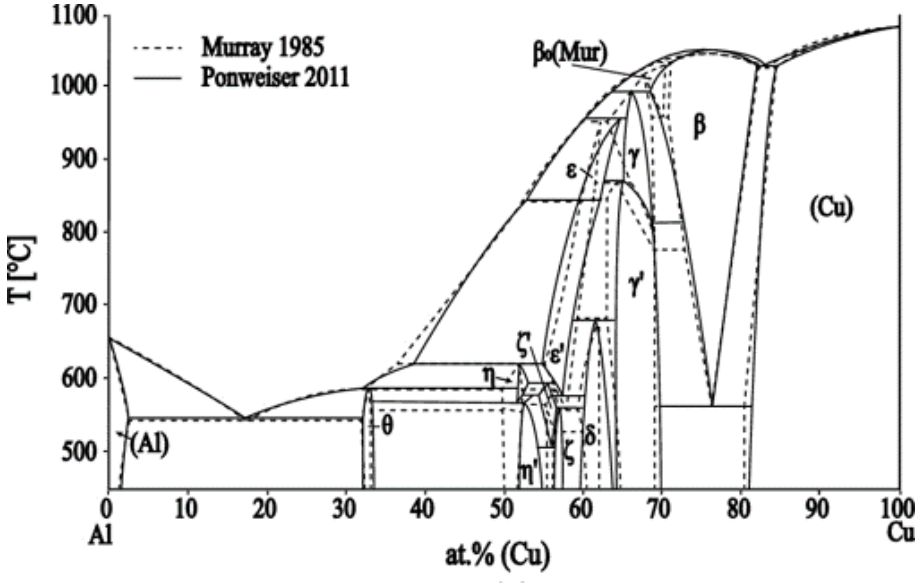

Figure 2.4: Al-Cu phase diagram [119]

The Al-Cu equilibrium phase diagram is shown in figure 2.4 [77, 119]. From the Cu-Al phase diagram, IMC's $CuAl_2, CuAl$, Cu_3Al_2, Cu_4Al_3 and Cu_9Al_4 are likely to be formed in the Cu-Al joint.

Phase	Composition	Crystal structure	Atoms/unit cell	Hardness HV(10 g)
Cu	Cu	Face-centered cubic	12 Cu	75
γ'	Al_4Cu_9	Body-centered cubic	36 Cu, 16 Al	770
ζ'	Al_3Cu_4	Monoclinic	12 Cu, 9 Al	930
η'	$AlCu$	Body-centered orthorhombic	10 Cu, 10 Al	905
Θ	Al_2Cu	Body-centered tetragonal	4 Cu, 8 Al	630
Al	Al	Face-centered cubic	12 Al	36

Table 2.1: Details of selected Al-Cu intermetallic phases, its crystal structure and hardness [77, 11]

The table 2.1 shows the main properties and characteristics of four selected intermetallic compounds which commonly occur in Al-Cu welding. The intermetallic compounds have very different mechanical properties compared to pure aluminium and copper. The increased hardness is due to increasing ionic, covalent and the reduced amount of metallic bonding phenomena. Furthermore, the complex crystal structure restrains the reduction of stress which leads to high brittleness. The reduced metallic bonds and the non-existence of electron gas also results in higher electrical resistance compared to the high-conductive base materials [96, 49, 42, 118, 46]. The table 2.2 shows the electrical resistivity of Al-Cu intermetallic phases. The Cu phase has the least electrical resistivity or highest electrical conductivity in comparison to Al and other intermetallic phases such as $CuAl_2, CuAl$, Cu_3Al_2, Cu_4Al_3 and Cu_9Al_4.

Phase	Cu	$Al_4Cu_9(\gamma')$	Al_3Cu_4 (ζ')	$AlCu(\eta')$	$Al_2Cu(\Theta)$	Al
Electrical resistivity($\mu\Omega cm$)	2.0	14.2	12.2	11.4	8.0	2.4

Table 2.2: Electrical resistivity of Al-Cu intermetallic phases [95, 93]

Typical fusion zone during laser beam welding and the presence of Al-Cu intermetallic phases are shown in figure 2.5. Application of heat onto the Al and Cu materials results in intermixing of Al/Cu and several intermetallic phases are formed in the joint, which are detrimental for mechanical strength.

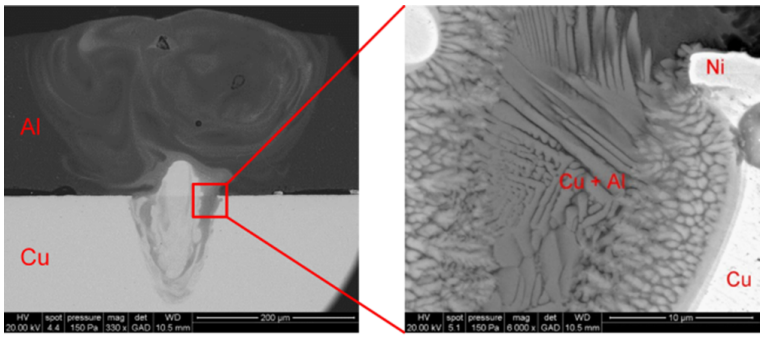

Figure 2.5: Fusion zone of aluminium laser welded to nickel coated copper [96]

It was shown by [116, 96, 3] that minimizing the amount of IMC, the performance of the joint is ductile. The mechanical strength is high when the size of intermetallic width is small about 2-3 μm.

Solid-state processes involve comparatively low welding temperatures such as ultrasonic welding [51, 117, 116, 108], friction stir welding [81, 33, 82], magnetic pulse welding and diffusion bonding can achieve relatively high strength [110, 99, 56, 79]. The IMC reaction layer could be significantly reduced due to the low welding temperature, but the formation of brittle Al-Cu IMCs cannot be completely avoided [42, 73]. In order to decrease the formation of undesirable IMCs, a variety of

filler metals were applied with the fusion welding processes, such as laser welding, TIG welding and laser-arc hybrid welding. Using filler metals effectively reduced the Al-Cu IMC and improved the mechanical properties of the Al/Cu joints. Weld bonding is a combination of adhesive bonding with a welding process to gain the advantages of each joining method. In the laser weld bonding and the friction stir spot adhesive bonding process, the decomposition of the adhesive changes the flow behaviour of the fusion zone and the diffusion between the Cu and Al elements, which influences the distribution and the thickness of the Cu-Al intermetallic and improves the property of the joint [75, 49].

Paper by Lee et al. [53] points out that for the joining of battery cells, several series and parallel connections between the battery tabs are required. Battery tabs are typically made from Aluminium (positive tab) and Copper (negative tab), and they have to be connected to bus bars which are made from copper, aluminium, brass and steel. It was stressed that proper joining technologies should offer a large joint area. The demand for a large joint area for the battery packs in battery electric vehicles (BEV) is because of the high current that flows through the joints between the cells to deliver electricity. Large joint areas serve two purposes such as to increase the mechanical strength of the joints, but also to reduce the temperature and thermal stress at the joints due to the flow of large current. With this aspect, the author suggested ultrasonic welding is more suitable for battery tab joining than the other welding, for example, resistance welding.
Therefore the joining process for dissimilar metals like Al and Cu should be flexible and offer a large joint area. A robust system for automation is also required as the battery pack joining process is mass production. Further, weld quality analysis is also desired.

2.3 Laser welding process

Laser is an amplified light generated by stimulated emission of radiation. It differs from the normal light in terms of special properties as mentioned below; therefore, it is a tailored light with unique properties. The properties of LASER are:

- Monochromatic: the light of single wavelength or colour
- Coherent (spatial and temporal)
- Low divergence. i.e., focusable to a very small dimension.

The central idea of laser processing is the use of high-intensity laser radiation to perform thermal processing by rapid vaporization or melting that results in the below-mentioned processes which are of interest in manufacturing engineering and the context of this thesis [80, 101, 64]. Some of the typical laser bases processes are:

1. Material removal: Cutting, Ablation, drilling
2. Joining: Welding-micro and macro welding, spot welding [5], brazing, soldering
3. Material enhancement/treatment: Heat treatment, cleaning, Annealing, restoring the lost superelastic properties due to cold working [8], surface texturing (in nanoscale)[12, 29].
4. Additive manufacturing: Selective laser melting (SLM), cladding, 3D printing

For laser welding of metals two main aspects have to be considered namely laser process and material properties. Some examples of the parameters are listed below.

1. Laser process
   (a) Wavelength of the laser: IR lasers(1030 nm, 1064 nm), Green laser (515 nm, 532 nm) and blue lasers (450 nm)
   (b) Optics used: resulting spot diameter depends on the focal length of the lens and the diameter of the fibres used.
   (c) Power: laser power output in kW.
   (d) Velocity: scan velocity of the laser beam in mm/s
2. Material properties
   (a) Absorption of the laser beam by the metal (or Reflectively)
   (b) Melting temperature
   (c) Thermal conductivity
   (d) Latent heat of fusion and vaporization

Laser beam welding (LBW) is a welding technique used to join multiple pieces of metals with a laser source. The laser beam provides a concentrated heat source, allowing for narrow and deep welds with high welding speeds. This process is frequently used for high volume applications, especially in the automotive industry. The welding process occurs when the movement between the laser beam and workpiece happens. The laser beam heats the material till the melting point of the material, then the material cools down and solidifies to form a welded connection. Shielding gas is sometimes used to cover and protect the working area [80, 64]. The laser welding can be classified based on the energy density input to the material as listed below:

1. Conduction welding
2. Transition keyhole welding

3. Keyhole welding

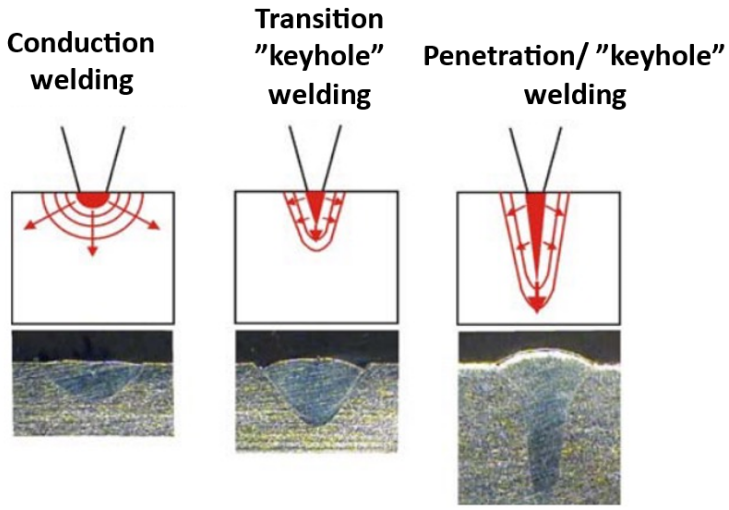

Figure 2.6: Modes of welding with a laser beam [92]

A schematic of different welding modes and the corresponding cross-sections is shown in figure 2.6.

Conduction mode: Conduction mode welding is performed at low energy density, typically around 1×10^6 W/cm^2 , forming a weld nugget that is shallow and wide. The heat to create the weld into the material occurs by conduction from the surface. Typically this can be used for applications that require an aesthetic weld or when particulates are a concern, such as certain battery sealing applications.

Keyhole or penetration mode: Increasing the peak power density beyond 1×10^7 W/cm^2 shifts the weld to keyhole mode, which is characterized by deep narrow welds with an aspect ratio greater than 1.5. Figure 2.6 shows how the penetration depth rapidly increases when the peak power density is beyond 1×10^7 W/cm^2, transitioning the weld mode from conduction to keyhole/penetration welding. The important physical properties like resistivity and thermal conductivity is a function of the state of metal i.e., solid, liquid or in the vapour phase [26]. The thermal conductivity is high in solid-state and rapidly reduces at vapour state. The mode of welding has a strong influence on the heat flow being conducted.

Transition mode: Transition mode occurs at medium power density, around 1×10^7 W/cm^2, and results in more penetration than conduction mode due to the creation of what is known as the "keyhole." The keyhole is a column of vaporized metal that extends into the material; its diameter is much smaller than the weld width and is sustained against the forces of the surrounding molten

material by vapour pressure. The depth of the keyhole into the material is controlled by power density and interaction time (welding speed). Because the optical density of the keyhole is low, it acts as a conduit to deliver the laser power into the material. Conduction welding can be thought of as a point source heating from the surface and the keyhole can be thought of as a line source heating from within the metal providing a more efficient welding source. In transition mode, the interaction time or power density is just sufficient to create a keyhole but not extend the keyhole deep into the part. Therefore, the welds exhibit shallow penetration with a typical weld aspect ratio (depth/width) of around 1. This mode of welding is used almost exclusively by pulsed Nd: YAG, disk and fibre lasers for many spots and low heat input seam welding applications.
One of the advanced techniques in laser beam welding is conducted in a vacuum chamber where it was shown to be beneficial for a stable high depth keyhole welding process. Such a process could be considered similar to electron beam welding in the sense that both processes are performed in a vacuum environment [27, 28, 103]. The resulting joint in a vacuum is very narrow and has a high depth of fusion.

2.4 Laser keyhole welding

For the keyhole-based process, the laser power intensity and the processing speed for a given material are important factors. In keyhole welding, the laser vaporizes the metal and the vapour pressure forms a cavity or keyhole as shown in the figure 2.7. The keyhole mode of welding results in the laser beam is highly absorbed into the material because it interacts multiple times with the metal and the metal vapour as it propagates through the material. However, initiating the keyhole with the Near-IR (Near-infrared) laser requires a substantial incident laser intensity, especially when the material being welded is highly reflective like Cu or Al. As the melt becomes rapidly heated by the laser, a severe thermal gradient is set up. The centre of the melt approaches the boiling point and the edge, which is in contact with solid material, remains at the melting point. This thermal gradient is associated with a surface tension gradient.

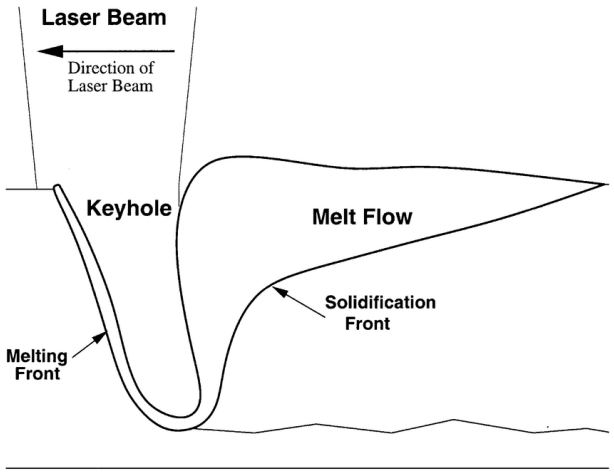

Figure 2.7: Keyhole welding process [45]

The higher surface tension at the relatively cool edges of the melt acts to pull the liquid away from the centre, which causes the geometry of the melt to change. The increase in central temperature amplifies the depth of the central depression by a combination of surface tension effects and the initiation of surface boiling which increases the pressure on the centre of the melt. This depression depth amplification continues until a keyhole is formed. This narrow deep hole is prevented from collapsing by the vapour pressure of the boiling liquid surrounding it.

Once the keyhole is formed, the absorption rises dramatically and the laser power or weld speed has to be carefully controlled to prevent excessive spatter from being ejected from the weld puddle. The different phases during the process are given by [25, 101, 45]. In the first phase, the laser heats up the solid material. The energy coupling is given by the material's absorption in solid-state under normal incidence. When the surface of the material reaches the melting temperature the second phase (heat conduction welding) starts. By changing the aggregate state from solid to liquid the absorption behaviour of the material changes i.e, absorption increases. The deep penetration welding process starts when the material surface reaches the evaporating temperature and the vapour pressure forms a keyhole. As a consequence, the irradiated laser energy is coupled into the workpiece by multiple interactions with the liquid keyhole wall as well as by propagating through the metal vapour in the keyhole as shown in figure 2.8 (d). The absorption mechanism is responsible for a significant enhancement of the energy coupling. As the keyhole depth increases further, the energy (laser radiation) coupling into the material rises again.

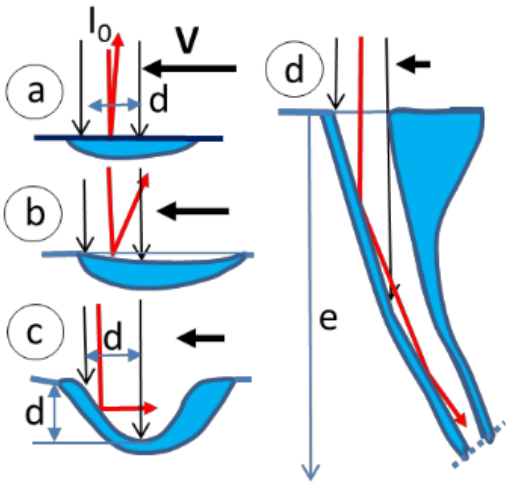

Figure 2.8: Absorption of laser light into the keyhole for different stages [28]

Keyhole generation and depth were studied by [28] [50]. The authors showed the effect of velocity influencing the melt pool geometry. The equation provides a relationship of the weld depth (e) as a function of velocity (V), laser power (P), absorption coefficient (A), enthalpy necessary to the melt the incoming solid (H) and laser beam diameter (d).

The model used by the authors are based on the penetration depth (e) and laser beam diameter (d). The e/d ratio is given by:

$$\frac{e}{d} = \frac{4 \times A \times P}{\pi \times H \times V \times d^2} \tag{2.1}$$

The above relation shows the aspect ratio (e/d) increases as the welding speed decreases. Conversely, the aspect ratio of the weld increases as the laser power increases. Therefore the laser power and the velocity have a strong influence on the keyhole formation and the aspect ratio of the weld i.e., weld depth to width ratio [28].

For laser welding of metals especially Cu and Al, having a keyhole based process is very efficient to solve the absorption problem. In addition to the high laser intensities, the process allows for a very high aspect ratio, narrow heat-affected zone (HAZ) and thermal damage zones. For metals, the absorption of laser radiation is very low. However, exceeding a certain threshold (i.e., melting phase) the reflectively is reduced as shown in the plot (figure 2.9).

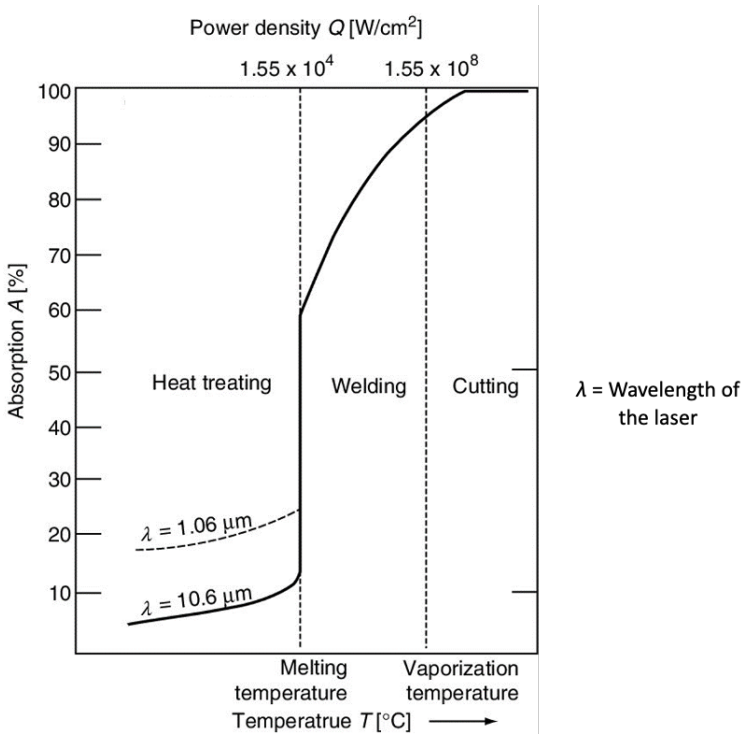

Figure 2.9: Absorption as a function of temperature or phase of the material [24]

The increased absorption is also attributed to the formation of plasma (ionisation). The plasma absorbs a great part of laser radiation. From high intensity to low-intensity irradiation two phenomena happen. They are:

- Plasma stays
- Plasma detaches

Such a phenomenon is described by [101] as shown in figure 2.10. If the laser intensity is in the range of $10^6\ W/cm^2 < I < 10^7\ W/cm^2$, the plasma stays in contact with the workpiece surface and the laser energy is absorbed in the plasma near the surface and is subsequently partly transferred to the workpiece. However, at higher intensity ($I > 2 \times 10^7\ W/cm^2$) the vapor density and the absorption increases. The laser energy in this case is entirely absorbed in a thin plasma at the side remote from the workpiece surface. Thus only a small fraction of the laser energy reaches the specimen. The plasma is strongly heated and accelerated away from the workpiece and gets detached. The detachment of plasma interrupts the laser processing [78]. With the application of suitable laser intensity, the energy coupling (also called 'plasma-enhanced coupling') can be increased. But with very high laser intensity the plasma shielding can occur and the laser energy cannot reach the workpiece surface.

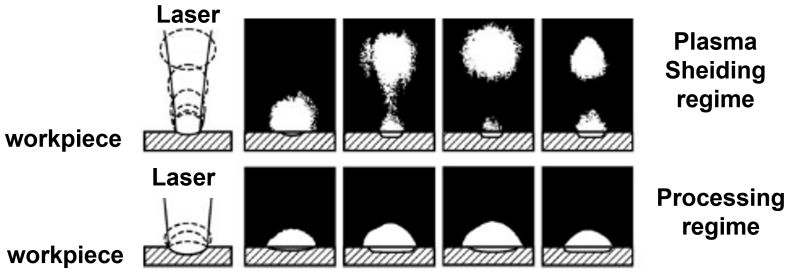

Figure 2.10: Plasma formation on the workpiece. Images of the laser-induced plasma above a steel specimen during processing with a pulsed CO_2 laser beam with 50 ns time interval. Top row: plasma shielding, laser intensity $I > 2 \times 10^7\ W/cm^2$, the plasma detaches from the workpiece surface. Lower row: laser processing, laser intensity $10^6\ W/cm^2 < I < 10^7\ W/cm^2$, the plasma stays in contact with the workpiece surface [101]

2.5 Laser trajectory

With the advancement of laser head scanners, the laser beam trajectory can be programmed to oscillate or move in a certain way so that weld width can be expanded without losing the power intensity or defocusing the laser beam.

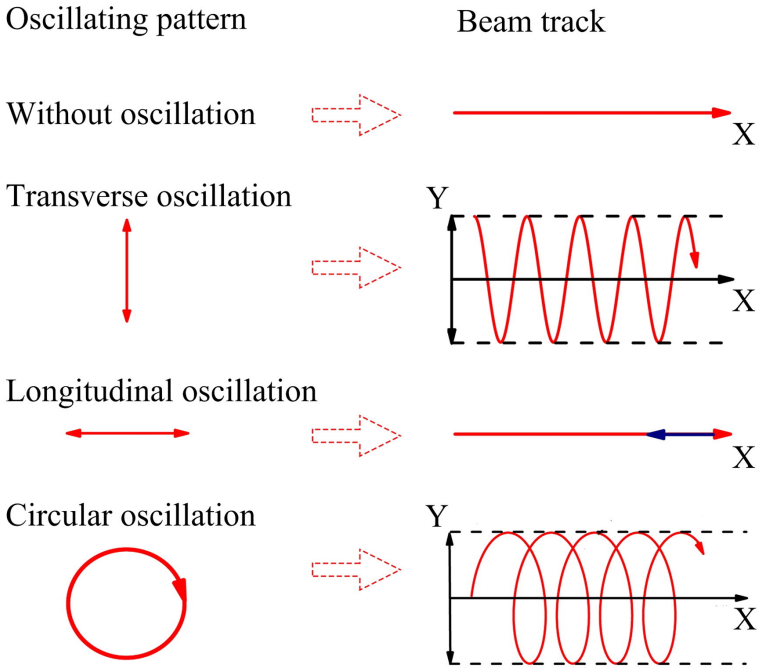

Figure 2.11: Laser beam trajectory for welding [106]

Such a beam oscillation technique is very popular in joining dissimilar metals to control the intermixing, control the porosity, spatter and increase the stability of weld bead. Some of the very popular wobbling techniques are transversal oscillation, longitudinal oscillation, circular oscillation and sinus oscillation as shown in figure 2.11.

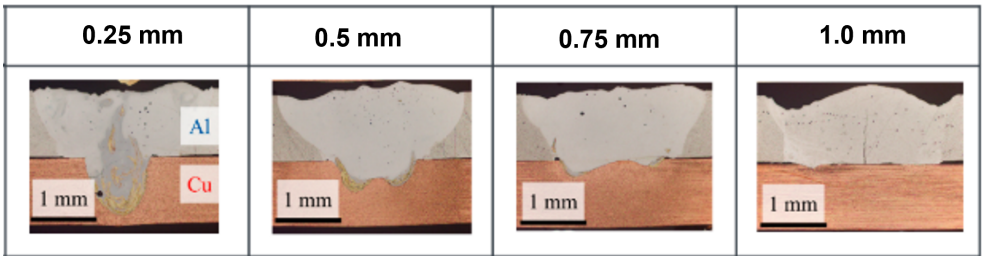

Figure 2.12: Effect of oscillation amplitude on weld pool [41]

The effect of wobbling with sinus oscillation for different amplitudes (0.25 mm – 1.00 mm) was studied by [41]. The author was welding with the Al placed on the top of Cu and the resulting weld cross-sections for different amplitudes are shown in figure 2.12. The depth of penetration into the Cu sheet can be influenced by increasing the oscillation amplitude. Therefore, with such a technique the depth and the intermixing can be controlled [6, 38, 30, 32, 96]. Thus, it is very beneficial for welding dissimilar metals e.g. Al and Cu joining. However, a control mechanism based on diffusion is not very widely studied, as it requires complex models [57] involving diffusion at high temperatures. The Cu-Al welding (Cu placed on the top) with the manipulation of the welding trajectory is not well studied.

2.6 Brittle behaviour of the Cu-Al joint

A typical weld with full depth into aluminium leads to the formation of excess intermetallic compounds and results in reduced shear strength. The failure is in the fusion zone where there is a large concentration of brittle phases as shown in figure 2.13.

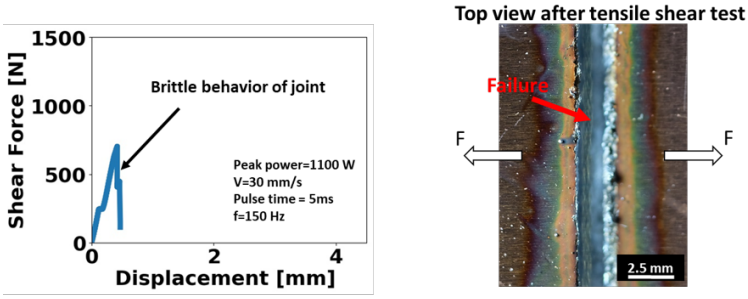

Figure 2.13: (a) Plot of tensile shear force (N) and crosshead displacement (mm) [59] ; (b) Top view of the joint fracture after tensile shear test

The laser process parameters such as laser power and velocity are very important factors in deciding whether the weld is brittle or ductile. The plot in figure 2.14 shows that the joint archives a high shear force and high cross-head displacement (i.e., high ductility) for samples welded with laser power of 1900 W, beam oscillation frequency of 100 Hz and velocity of 100 mm/s. The brittle weld (laser power of 1600 W) fails at low shear force and cross-head displacement.

The laser power required for welding Cu to Al also depends on the wavelength of the laser used, as the absorption of the laser radiation is dependent on the laser wavelength. The commercially available laser wavelengths for processing Cu are 1030 nm (near IR laser - disk laser), 515 nm (green laser - disk laser) and blue laser (480 nm - diode laser). The laser wavelength of 480 nm has higher absorption in comparison to green and near IR lasers. It was shown by [60] that for welding Cu-Al with a green laser wavelength of 515 nm, a laser power of 700-750 W was required and for 1030 nm laser power of 950 -1000 W was required. Welding with a green laser wavelength of 515 nm requires lower laser power in comparison to the near IR laser wavelength of 1030 nm. The IR laser is generally available at high powers up to 16 kW while the green lasers and blue laser are typically available with 1 kW and 0.5 kW respectively. However good penetration into the Cu can be achieved with all three laser types but at different laser powers.

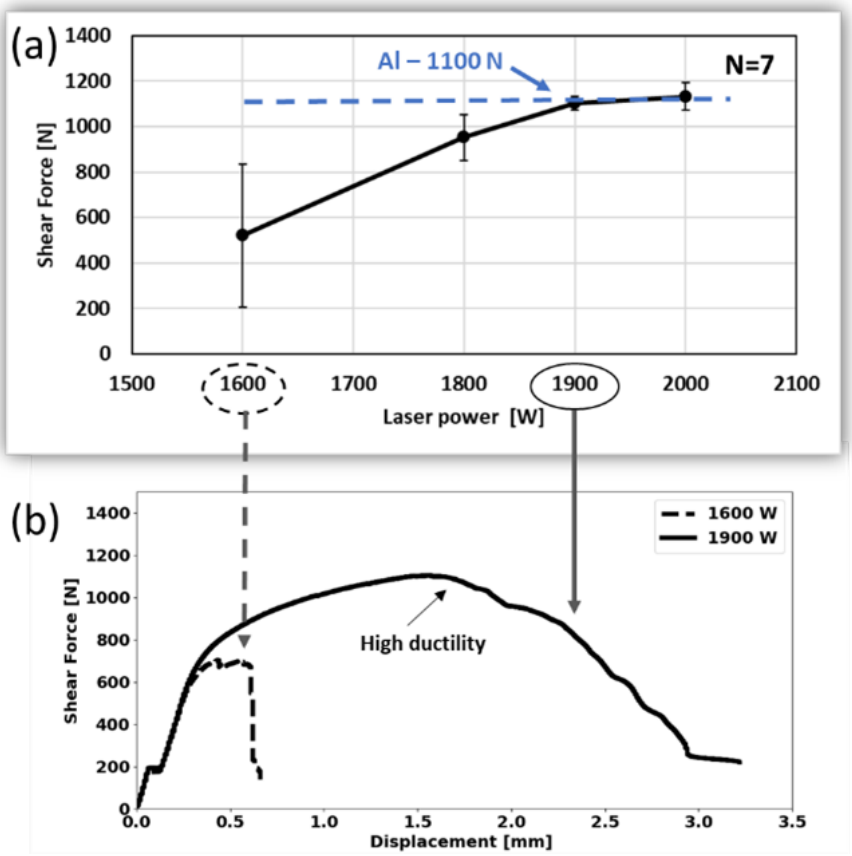

Figure 2.14: (a) Shear force of Cu–Al welds at different laser powers and feed rate of 100 mm/s; (b) Shear force and displacement plot for the Cu–Al welds at feed rate of 100 mm/s with laser power of 1600 and 1900 W [61]

For welding, Al and Cu different strategies are employed and are summarized as below.

- Selective melting of Al metal and Cu remains in solid-state – reduced intermixture [95, 85]
- Selection of laser process parameters such as laser power, velocity for continuous wave and the pulse duration, pulse shape, pulse frequency for pulsed wave laser is very influential [54, 34].
- Selection of Al or Cu metal on the top has a high influence on the laser power required [55, 59, 31, 52, 83].
- Sufficient melting and intermixing is important for the Cu-Al weld strength [62].
- Melt pool oscillations by power modulation result in a stable weld. A copper content either below 50 at.% or above 80 at.% is suggested by [100].

2.7 Monitoring of welding process

The interaction of laser beam and material is strong in the keyhole mode of welding. The online monitoring and quality inspection of the welding process are essential for high-quality production [112, 47]. The ability to perform contactless monitoring during the actual welding process is very attractive for implementation into industrial automation. Laser process monitoring for identification of the defects have been investigated for a long time but the industrial application is hindered by the considerable cost of the sensor, low device accuracy and poor detection efficiency. The process information can be observed by the spectroscope, in-situ X-ray [66], acoustic techniques, high-speed camera, photodiode and CCD detectors [37, 98, 113, 48]. The idea behind online monitoring is to extract welding information such as weld depth, keyhole dynamics, spatter, melt ejection to identify weld defects in real-time. The schematic of the optical radiation during the keyhole mode of welding is shown in the figure 2.15.

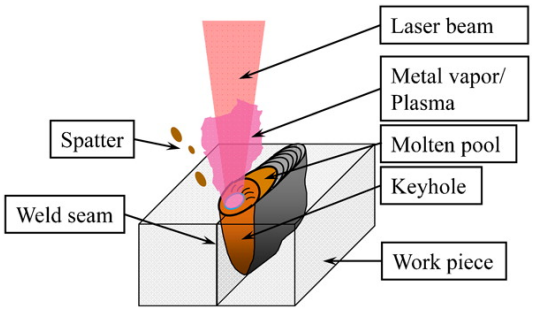

Figure 2.15: Schematic diagram of keyhole mode laser welding and the associated process emissions [112]

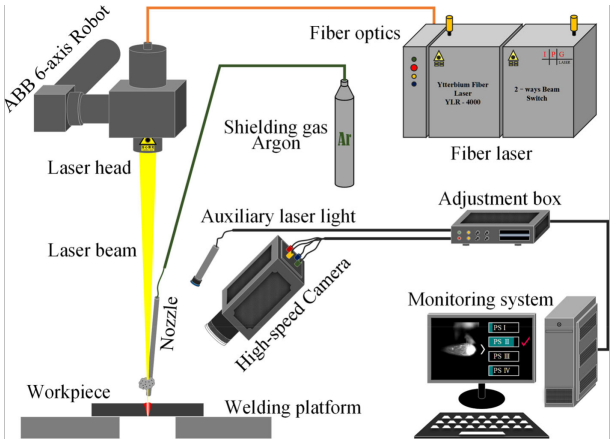

Figure 2.16: Imaging of vapour plasma, melt pool using high-speed camera with illumination from a auxiliary laser light [13]

In the keyhole mode of welding the metals, the laser interaction with the base metal results in the phase change of the material from a solid phase to a liquid phase and then to the vapour phase and to plasma phase. The rapid vaporization of the metal during keyhole welding is accompanied by metal vapour or plasma plume of the metal. The process dynamics of plasma plume and molten weldment are captured on a high-speed camera and further data analysis is performed. More recently, such approaches are based on the image processing techniques as shown in the figure 2.16 [21, 65, 13].

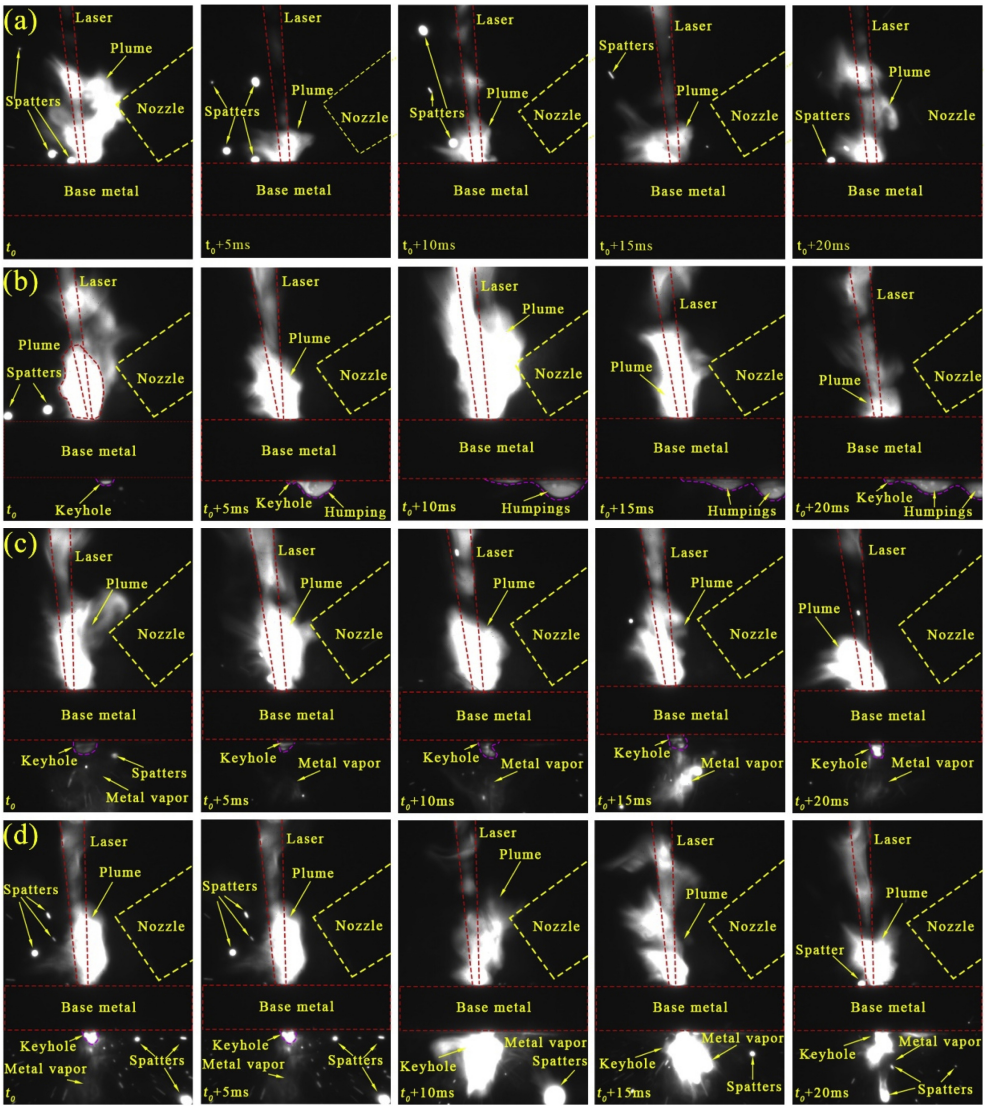

Figure 2.17: High speed camera images observing the top and bottom surface of the laser welding process at v=0.8 m/min (right to left welding direction): (a) P = 3kW; (b) P = 4 kW; (c) P = 5 kW; (d) P = 5.2 kW [114]

The figure 2.17 shows the high-speed recordings of the laser welding process and the plasma plume emission for the velocity of 0.8 m/min and laser powers of (a) 3 kW, (b) 4 kW, (c) 5 kW,

(d) 5.2 kW. The images show the observation of metal vapour on the top and bottom surface of the welding process for different time intervals starting at 0 ms, 5 ms, 10 ms, 15 ms, and 20 ms. It can be seen from the images that for laser powers of 4 kW, 5 kW and 5.2 kW the keyhole reached a full depth of the base material and the vapour plume can be seen in both the top and bottom of the base metal. The plume shape also depends on the keyhole depth as it can be seen in figure 2.17 (a) at a laser power of 3 kW for time intervals of 5 ms, 10 ms and 20 ms the plume is deeper in the base metal in comparison to the initial time value of 0 ms (beginning). In the full penetration mode in figure 2.17 (d) for laser power of 5.2 kW, the keyhole reaches the bottom of the base metal and the metal vapour is clearly visible in the bottom sheet.

A schematic representation of the laser keyhole welding process and melt flow behaviour is shown in figure 2.18. For partial penetration, the melt flow is contained within the base metal and it results in a limited penetration. Further increasing the penetration depth humping occurs at the bottom of the sheet. Further increasing the penetration depth to full penetration fine results are obtained without any humping. However further increasing the penetration from the fine penetration condition, leads to over penetration and spatters. Therefore based on the applied laser power the melt flow conditions and the keyhole behaviour change.

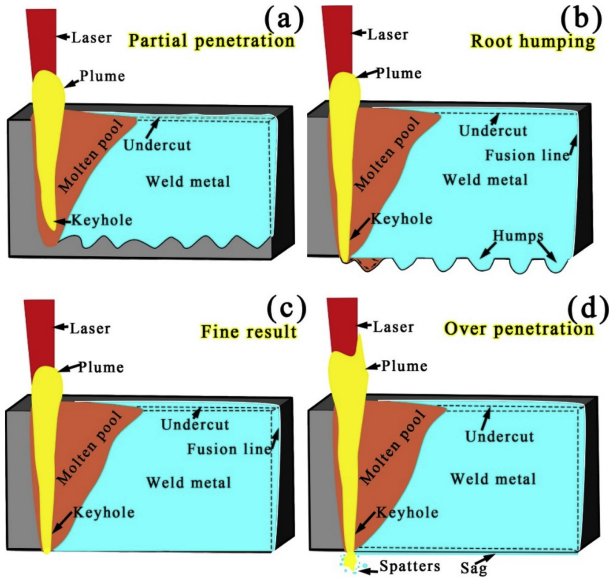

Figure 2.18: Schematic illustration of melt flow behaviors: (a) partial penetration; (b) root humping; (c) fine result; (d) over penetration [114].

The figure 2.19 shows the photodiode signal and the corresponding cross-section for full and partial penetration. The authors used camera observations of the welding zone to distinguish the partial and full penetration. The photodiode signal for the partial penetration weld is higher in

intensity than the full penetration weld. As it can be seen in the cross-sections for the partial penetration weld the depth of the keyhole is limited to the base metal and the plume is present at the top. As the depth of penetration is full, the keyhole is in the bottom of the base metal and the plume intensity on the top of the base metal is decreased.

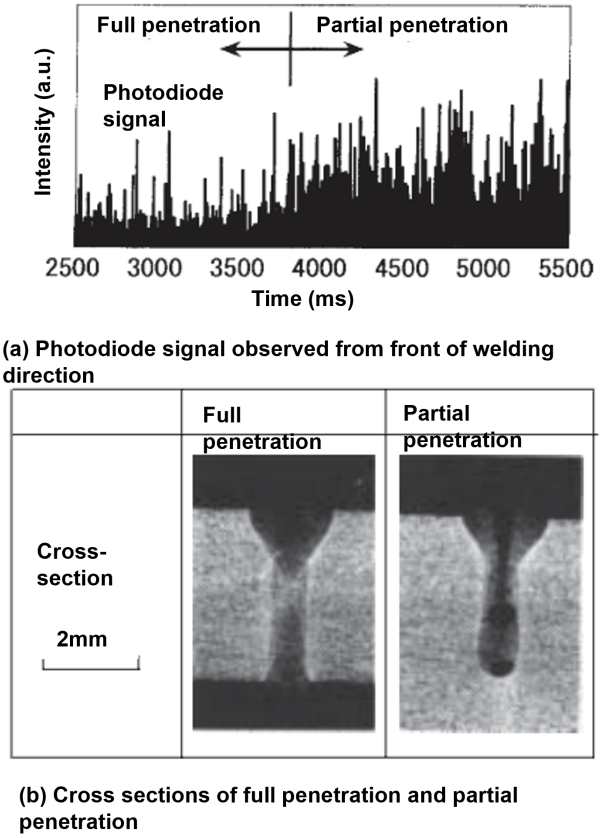

Figure 2.19: (a) Photodiode signal observed from the front of welding direction; (b) Cross sections of full penetration and partial penetration [43]

A schematic representation of the keyhole welding process from the bottom of the keyhole is shown in figure 2.20. For the partial penetration and full penetration case (a) and (b), the keyhole is closed. As the keyhole reaches the bottom in case (c), the metallic vapour also reaches the bottom sheet. For further increase in laser energy, the keyhole is collapsed (case d) and results in melt ejections. The laser-MAG hybrid welding process is presented in figure 2.20 only to illustrate that metallic vapor is formed in the bottom keyhole.

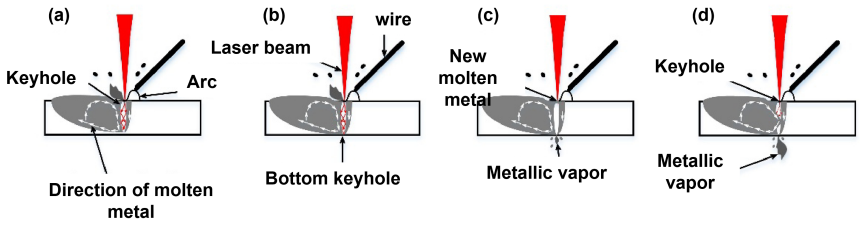

Figure 2.20: Four different laser-MAG hybrid welding process status; (a) weldment is melted by laser heat and is in a partial penetration welding status, (b) full penetration is obtained by increasing the absorbed energy of keyhole and the keyhole bottom is closed, (c) new molten metal from droplet transition is covering the top surface of the keyhole and the keyhole bottom is opened, (d) the equilibrium of keyhole is broken resulting in a keyhole collapse [107]

The authors in [107] concluded from the high-speed observation of the welding process from the top and bottom of the keyhole that the continuous opened or closed keyhole (case b and c in figure 2.20) are most likely to occur during the welding process and is a stable welding process.

The laser beam oscillations and the plume ejections can be monitored. Such an optical emission can be used as a tool to understand the molten pool oscillations due to the wobbling trajectory [67]. Extensive research is also conducted in the modelling of plasma heating by ultrashort laser pulses on a nanosecond scale [20] . Other possibility for the process monitoring is to combine physical modelling and in-process information to create a closed loop control that is highly responsive [71]. Most of the real-time systems for weld monitoring are used to measure the weld bead dimensions [76].

The main interest of monitoring techniques is to detect a metallurgical defect, loss of alloying elements, uncontrolled ejection of the melt material (figure 2.21) and intermixing in case of dissimilar welding [40, 86, 71, 72, 19, 18, 1]. For welding dissimilar materials, identification of the melt from the lower sheet in overlapped configuration is very challenging due to poor signal.

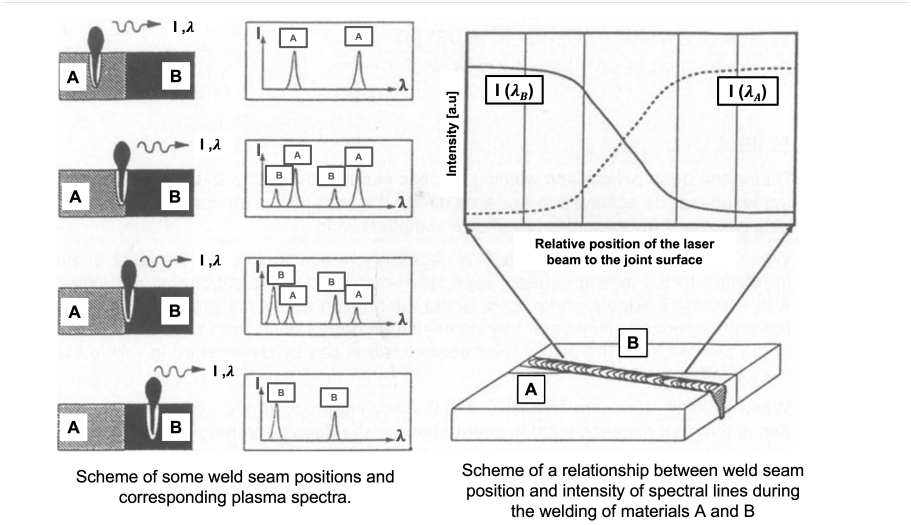

Figure 2.21: Laser Welding process by means of spectroscopic data [94]

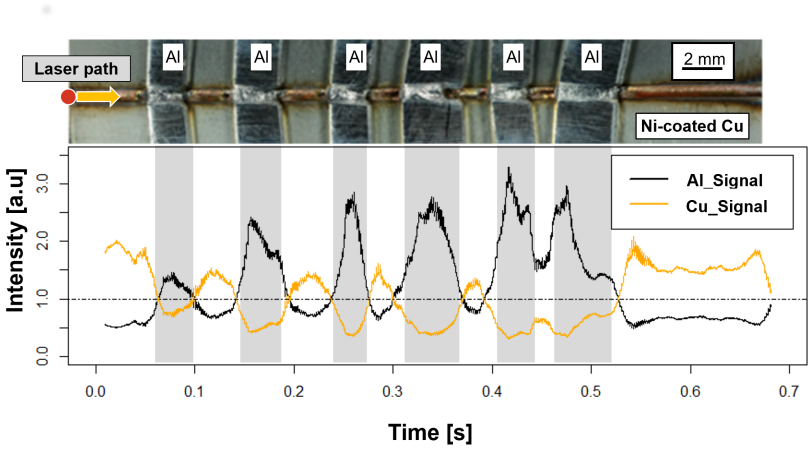

Figure 2.22: Chromatic filters with CWL 395/400 and varying FWHM 5/10 was used to detect Al-characteristic peaks at 394/396 nm [86]

Detection of melt during welding was shown for butt configuration [94] and sheets arranged in series [86]. But there is a lack of understanding of the signal intensities formed and their correlation to the melting. Identification of strong and weak signals related to energy intensity is not well studied in the literature.

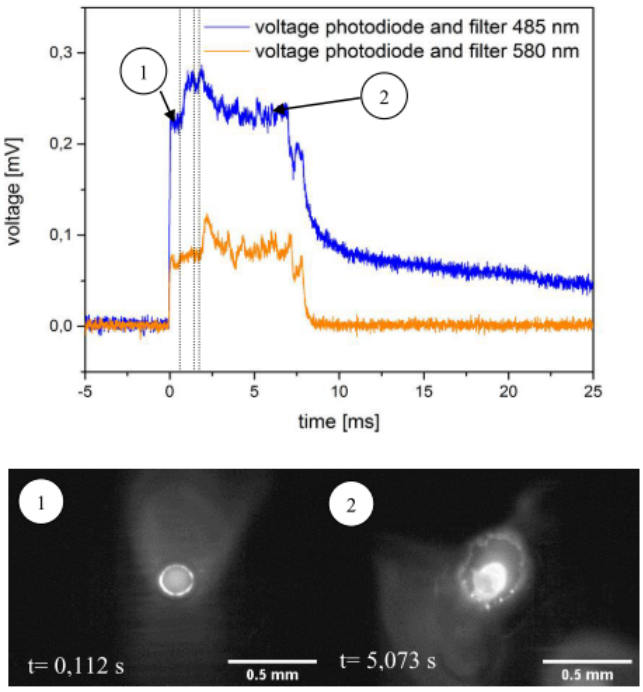

Figure 2.23: Process stages recording of the photodiode and high-speed camera of Al-Cu laser welding [89]

The authors in [89] studied the Al-Cu spot welding using the specific wavelengths of 485 nm and 580 nm with an acquisition speed of 100 kHz. The setup was a simplified version of the actual welding process representing only a single spot. Therefore the time domain data shown in figure 2.23 is a representation of the laser beam penetration in the depth direction (Z) only. In reality, the laser beam moves in the x-direction (linear welding), the x-y direction in case of wobbling for actual seam welding in addition to penetration depth. However, the research could not prove a relation of the welding status to the process parameter, or strength of the weld.

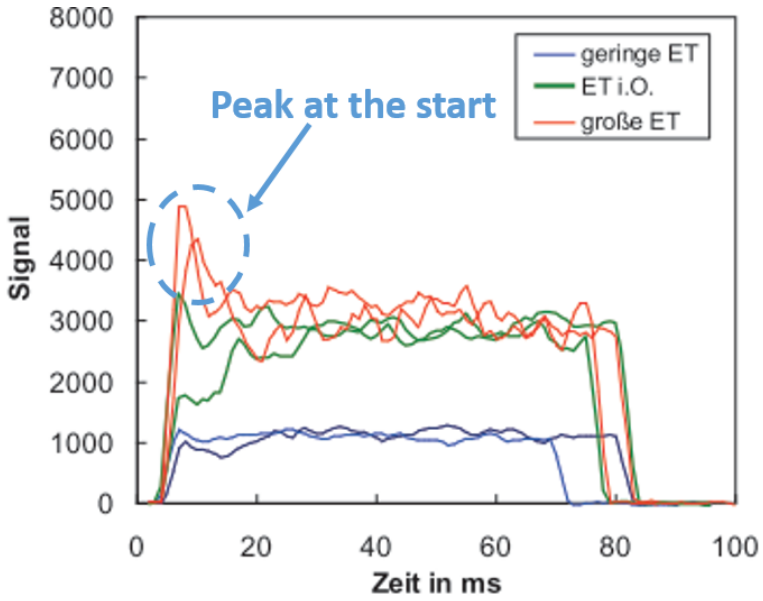

Figure 2.24: Time-resolved emission curve during laser welding of the aluminium-copper mixed compound for the wavelength of 470 nm [54]

Research work by [54] used 470 nm specific wavelength to study the Al-Cu laser welding process recorded at 1000 Hz. The sampling rate of 1000 Hz was too low to capture the process dynamics. The experiment results were demonstrated in the time domain and no conclusive correlations were shown to the actual weld. Authors studying welding of Zinc coated steel and Ti alloy found that the frequency features of weld pool oscillations are in the range of 300-500 Hz. Strong fluctuation of the keyhole was found to be in the range of 1600-2400 Hz. These approaches are based on the analysis of a range of wavelengths in the visible wavelength bands (400 nm-700 nm). However, features of wavelengths specific to the material being welded are not well studied. These approaches have only been studied for similar metal welding in identifying defects like pores, lack of penetration. No indication of the welding status for dissimilar Cu-Al welds was studied. It was shown by [114] from the observation of high-speed recordings that the plasma plume and keyhole behaviour is highly dependent on the depth of penetration into the weld. However, there is a lack of studies focusing on the plume observations using photodiode from the bottom sheet.

2.8 Convolutional neural network

For the laser welding process, automated quality analysis is desired to increase the reliability of the joint. With the advancement of sensor technology and the availability of high-resolution cameras, the image processing of the weld beads can provide a good indication of the status. For image processing with the recent advancement in the field of deep learning and increased availability of computing power, large image data can be utilized for quality purposes. This section introduces the Convolutional Neural Network (CNN) and literature related to its application in laser-based processes. Deep learning is a subfield of machine learning that learns based on the provided examples or data. CNN is a variant of a neural network that extracts higher features or representations of the content in the subjected images. The CNN extracts the image features automatically based on the data or examples rather than writing a set of rules to extract the features manually. The motivation of the CNN is the availability of the data and the ability of the system to intelligently extract the features in the images. CNN takes the raw pixels from the images, train the model and then extracts the features.

The basic architecture of the CNN model consist of sequences of one or more of the following layers namely

- Convolutional layer
- pooling layer
- Activation function
- Fully connected layer

For the laser welding process, the CNN model is applied to high-speed camera images of the plasma plume observations, melt pool images, images from the thermal camera and acoustic signals [50] [105] [115]. The figure 2.25 shows the melt pool images and the corresponding images of the specimen for different laser powers of 100 W, 150 W, 200 W, 250 W, 300 W and 350 W. The melt pool images were obtained by high-speed camera co-axial to the laser beam. The melt pool images are distinct in terms of the size of the bright spot, representing the laser-material interaction for different laser powers. Such images were further fed to the CNN model for training and prediction of laser power. The authors mainly focused on the prediction of laser power [50].

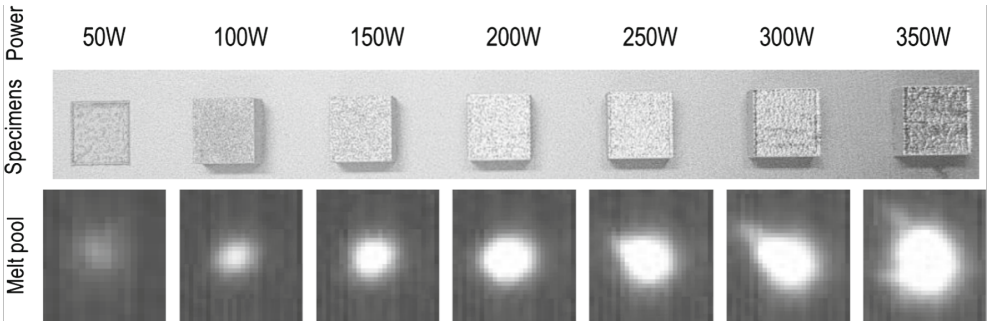

Figure 2.25: Example of melt-pool images for each laser power condition used for prediction with CNN model [50]

Similarly, thermal images during the welding are also used for the prediction of the weld type such as good or bad weld. The figure 2.26 shows the structure of the CNN model used for training and prediction of the weld based on the thermal image as an input. The authors used a resistance spot welding process for joining dissimilar materials namely dual-phase steel (DP600) to austenitic stainless steel (AISI304) and achieved an accuracy of 97.3% for predicting 3 different classes such as good weld, acceptable weld and bad weld.

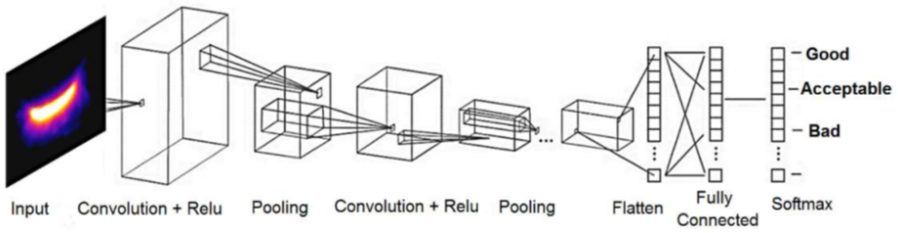

Figure 2.26: Basic structure of a CNN used for quality prediction in dissimilar spot welding DP600-AISI304, using an infrared image [105]

Other works based on the high-speed images captured during welding in visible range were applied to capture the geometrical features of the plume, keyhole and spattering [115]. With such an approach defects such as blowout, humping and undercut were predicted with an accuracy of about 92-94%. The overview of typical defects that were detected is shown in figure 2.27.

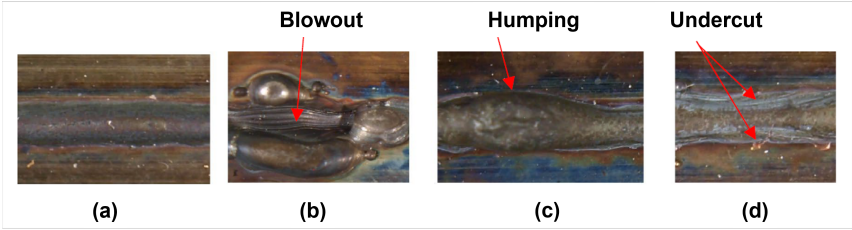

Figure 2.27: The typical top views of the four welding status. (a) good weld; (b) blowout; (c) humping; (d) undercut [115]

In literature for compiling the CNN model, some of the common optimization algorithms used are Adam optimizer ([62],[105],[109]), AdaDelta and Adagrad optimizer [115]. In laser welding application for the classification problem, the prediction accuracy achieved depends on the type of data used, such as melt pool images, thermal images, plasma plume or keyhole observations and the type of defect identified (classes) such as blowout, humping, undercut or weld types such as good weld and bad weld. The typical prediction accuracy range between 92-97 %.

2.9 Summary

- Al-Cu welding results in brittle intermetallic phases which deteriorate the joint performance. The formation of IMC due to solubility issues is described by the Hume-Rothery rule.
- Laser welding of Al-Cu offers many advantages like high processing speed, contactless process, very narrow heat-affected zone, automation.
- For laser welding, the absorption of laser radiation by the material is very critical. A laser-based process can be used to precisely control the heat input and minimize the IMC which results in a ductile joint.

The literature on Al-Cu welding mainly deals with limiting the intermetallic layer thickness to obtain a strong joint. The methodology is to irradiate laser on the Al sheet because of the low melting temperature of 660°C. Therefore with this condition, the formation of phases are layered at the interface and the thickness of intermetallic phases are kept to a minimum value.
However, the melting of Cu to obtain a fusion weld is largely unexplored. From [63, 59], the fusion welding by irradiation of Cu results in a large intermixing of Cu-Al.
Therefore the intermixing to obtain a microstructure which is a combination of brittle and ductile composition is not well explored. The other topic in laser welding of Al-Cu and another dissimilar metal welding, in general, is related to optical monitoring of the process. Approaches are based

on optical analysis of the radiation, like using a high-speed camera, spectrometer and photodiode. Out of these, photodiode implementation is very attractive for its high-speed acquisition at a low price. Automatic quality analysis is highly desired for the laser welding process. Application of convolutional neural network for automatic prediction of the welding parameters such as laser power and velocity is increasingly used. These approaches are mainly driven by the use of weld images or process images for prediction.

Chapter 3

Scientific hypothesis

3.1 Research gap

In joining of Al and Cu for industrial applications, high process speed, precise heat input and an autonomous process are required. The laser is characterized by its excellent control of power over the spatial and temporal domain. With laser beam oscillation also known as wobbling, intermixing is controlled to obtain the best mechanical and electrical properties of the joint. Several early research prior to 2015, as discussed in the literature review section in chapter 2 focus on welding from the Aluminium side to Copper due to the low laser power required to melt the Al metal in comparison to Cu. However, for design flexibility, welding from Cu sheet is also required in several cases as multiple sheets of copper must be welded. In addition to linear welds, spot welds are also of interest for the industry as cylindrical cell configurations are increasingly being used in the automotive industry. With the availability of high-speed scanners, the laser can be directed not only in linear trajectory but also in circular trajectory to make spot welds. With the circular laser trajectory, much more applications are possible that require design similar to mechanical bolting, for example in welding of Copper Bus Bar. However, only a small number of publications address these requirements. The following is identified as a research gap

1. A limited number of studies has been conducted in laser joining of Cu and Al by spiral trajectory resembling a bolted connection or a spot welding and its effects on the interface formation is not well known.

2. Welding from copper side to aluminium side is not well explored. This is partly because of the high reflectivity of copper. However, with the availability of high power near IR and green laser, welding of copper can be achieved now. The fusion zone mechanics of welding copper to

aluminium in dissimilar combination deserves an extended study.

3. Non-destructive interpretation of the weld images and its usage for prediction of weld status is not well studied.

4. There are no reliable non-contact joint qualification techniques for welding of Cu-Al. The light-based emission is a good indicator for extracting information about the process cheap and fast.

Based on the research gaps in the literature, leading research questions are formulated to the scientific understanding of the fusion welding process by laser irradiation of Copper sheets.

1. Is welding from the highly reflective copper side feasible with intermixing?

2. How can fusion welding of copper to aluminium bring a beneficial microstructure?

3. Can the weld images from the top of Cu, be used for non-destructive identification of the weld class?

4. Can the spectral emission during the welding of Cu-Al be used for indicating the weld status?

3.2 Hypothesis

Laser welding is a thermal process, which involves the melting of metals being joined. Dissimilar welding, in particular aluminium and copper, favours the formation of intermetallic compounds (IMC) because of metallurgical incompatibility. However, the laser can be controlled, to precisely deliver heat input into the material. The weld fusion zone formed is highly influenced by the laser process parameters namely the laser input power, velocity and the chosen weld strategy i.e., spiral welds, line welds or linear welds with wobbling. Laser beam movement can influence the formation of IMC by mixing in the shape of the trajectory in a cross-sectional direction. Intermixing an optimum amount of Cu and Al can bring beneficial phases to the joint and mitigate the effect of brittle phases. Moreover, welding from the copper side to the Aluminium side allows for increased weld penetration, which is due to the higher solubility of welding from the copper side (about 18.5 % as shown in the phase diagram in figure 3.1). The maximum solubility of Al in Cu (Cu on top) is 18.5 at.% which is significantly higher in contrast to the maximum solubility of Cu in Al which is equal to 2.5 at.%. Therefore more Al can be melted in Cu-Al welding resulting in a complete fusion welding process.

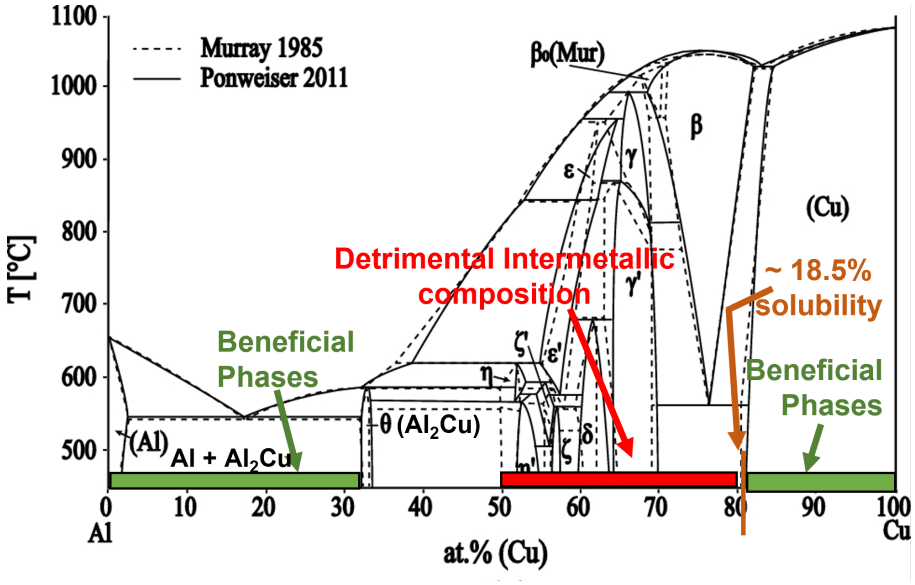

Figure 3.1: Phase diagram of Cu and Al showing beneficial and detrimental phases (composition in the range of 50 - 81.5 % at of Cu such as Al_4Cu_9 (γ'), Al_3Cu_4 (ζ'), $AlCu$ (η')) [69]

Based on the identified research gap, the following hypotheses are formulated.

1. Laser beam welding from the Copper side results in metallurgical bonding by promoting beneficial diffusion of Al and Cu in the weld seam by laser beam movement in form of spiral trajectory.
2. Intermixing in the fusion welding of Copper to Aluminium leads to a stronger joint microstructure, by suppressing the effect of brittle intermetallic compounds.
3. Weld images taken from the top of Cu can be used for the prediction of weld status by modelling a convolution neural network.
4. Welding signals from the top of Cu sheet and bottom of the Al sheets can be used for identification of the weld status such as weak weld, strong weld and excessive weld.
5. Analysis of the optical emission corresponding to the Al peak of 396 nm from the bottom sheet can be used as an indication of an excessive weld.

Chapter 4

Experimental methodology

4.1 Materials

The materials used in the experiments are Aluminium 99.5% pure (AA1050) and Copper 99.95% pure (CuOF). The dimensions of the Cu and Al samples used are 40 × 60 mm and 40 × 55 mm respectively. The thickness used is 0.4 mm. This particular dimension is chosen based on the previous investigations performed by [85] and [54].

Material	Grade	Thickness [mm]	Dimension [mm]
Copper	99.95 % pure - oxygen free	0.4	40 × 60 mm
Aluminum	Al 1050	0.4	40 × 55 mm

Table 4.1: Specification of Al and Cu for laser welding

4.2 Laser welding approach

4.2.1 The spiral trajectory for welding

The laser welding was performed with a disk laser of wavelength 1030 nm and maximum power output of 2000 W. The laser light was guided by an optical fibre of diameter 50 μm to the scanning system. The scanning system used was from Blackbird Robotersysteme GmbH, Garching, Germany. The optics of the scanning system had a focal length of 255 mm and the collimator length of 116 mm, resulting in a spot diameter of 110 μm. The scanning system focused the laser beam onto the working piece via F-Theta optics and laser beam trajectory can be programmed on the Blackbird software interface. The table 4.2 shows the specification of the laser and scanning system used in this research. For a circular welding profile, a spiral trajectory also known as archimidian spiral is

selected, as a continuous weld can be performed from the centre of the circle to the outer diameter. This approach increases the total weld diameter to 5 mm with a smaller laser spot size of 110 μm. The diameter of the spiral is chosen as 5 mm and the laser beam direction is starting from the centre point of the spiral i.e., from inside to the outside as shown in the figure 4.1. The number of spiral turns is selected as 5, i.e., the number of turns equal to the diameter of the spiral. The laser input energy per unit length (J/mm) is influenced by changing the applied laser power (W) and velocity (mm/s). Based on the preliminary experiments, the laser power is chosen in the range of 1500 W to 2000 W and velocity in the range of 100 mm/s - 600 mm/s. The table 4.3 shows the laser power and velocity combinations used.

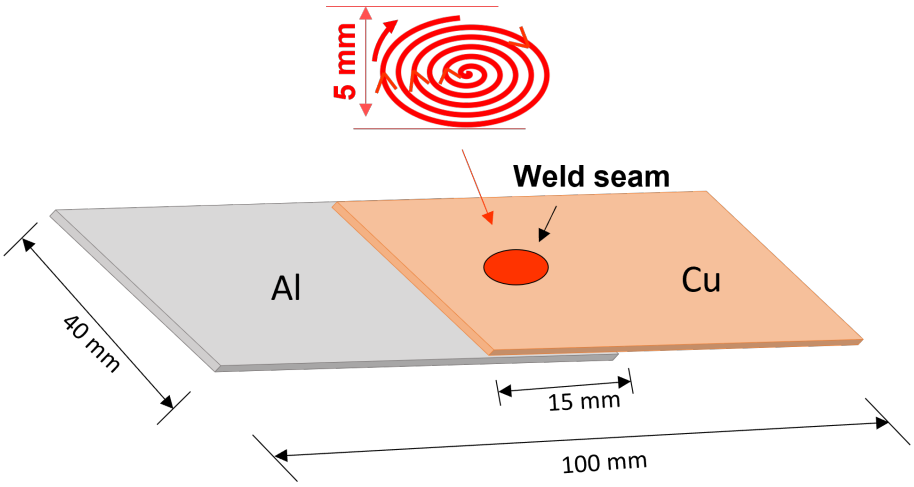

Figure 4.1: Sketch of overlap welding of Cu to Al with spiral trajectory

System	Manufacturer	Specification
Scanner	Blackbird	Optic focal spot - 110 μm
Laser Source	TRUMPF	1030 nm, Maximum power-2000 W

Table 4.2: Overview of laser and scanning system used for welding

Laser power [W]	Velocity [mm/s]
2000	600, 500, 400, 300, 200
1800	500, 400, 300, 200
1700	400, 300, 200
1600	400, 300, 200
1500	300

Table 4.3: Laser power and velocity used for Cu-Al welding experiment

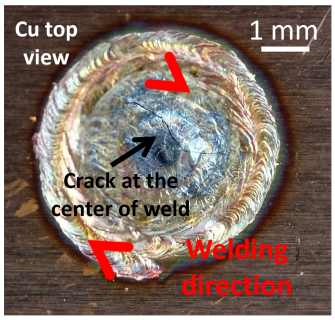

(a) Welding direction:
outside to inside

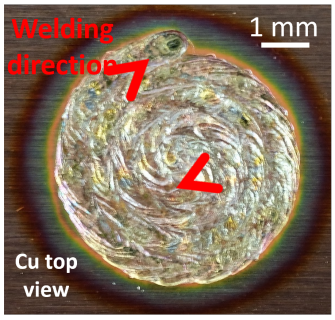

(b) Welding direction:
Inside to outside

Figure 4.2: Top view of Cu-Al spiral welds. (a) Welding direction starts from the outside to inside of the spiral (b) Welding direction starts from the inside to outside of the spiral

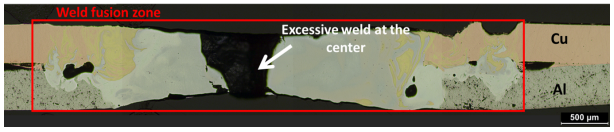

Figure 4.3: Cross-sectional view of the Cu-Al sample welded starting from the outside to inside of the spiral

The Cu-Al weld images for outside to inside direction of spiral trajectory and inside to outside direction of spiral trajectory is shown in figure 4.2 (a) and (b) respectively. The laser trajectory starting from the inside to outside direction (figure 4.2 (b)) is preferred rather than the outside to inside direction because for the outside to inside direction the heat accumulation resulted in excessive weld at the centre as shown in the cross-sectional image in figure 4.3.

4.3 Weld joint analysis

4.3.1 Macroscopic and microscopic analysis

The macroscopic analysis is performed by taking a high-resolution image of the welded sample using the Fujifilm X-Pro2 with ZEISS Touit 50mm f/2.8M macro planar lens. For a higher magnification of the welded sample, the light optical microscope DM4000 M from Leica was utilized.

4.3.2 Metallography preparation

For metallography, the samples are prepared by sectioning the region of interest. A compression mounting system from Buhler (Buhler SimpleMet 4000) with Phenolic powder and TransOptic as mounting media is used for moulding the sample. The pressure, heating time and temperature setting on the moulding machine is set as 180 bar, 4.20 min and 180 °C respectively. The grinding and polishing were performed in steps using semiautomatic grinding machine Buehler MetaServ 250. Firstly coarse grinding with 180 grit SiC grinding sheet was done for 5 min with water as a lubricant. The next grinding steps are performed with 800 grit, 1200 grit and finally with 2500 grit. Between each step, the specimen is cleaned with ethanol in an ultrasonic bath for 2 min. After the fine grinding with 2500 grit, the polishing is performed with 6μm, then with 3 μm for 3 min. Finally, the fine polishing steps are performed with 1 μm and 0.25 μm for 2 min and 1 min respectively. For all the polishing steps water-based lubricant is used. The detailed procedure is shown in table 4.4.

For etching, the Al-Cu weld seam, Keller and Macro etchant Cu (Table 4.5) are used. The etchant is applied by immersing the polished metallography specimen in a chemical solution for a specified time and finally rinsing it with water. For analysis of microstructure light optical microscope (Leica DM 4000 M) is used.

4.3.3 Scanning electron microscope

The scanning electron microscope (SEM) equipped with Energy-dispersive X-ray spectroscopy(EDX) is utilized to analyse the morphology and the local chemical composition in the Cu-Al joint. Hitachi SU-70 with 20 keV was used to take SEM images of the welded Cu-Al joints. An energy-dispersive (EDS) detector from Oxford Instruments is used for the identification of the elements in the joint. The evaluation of the data was performed with INCA software from Oxford Instruments. For identification of the phase, the composition of the element in atomic % is used.

Step	Description of the Procedure	Time[min]	Speed [RPM]	Force [N]	Lubricant
Grinding	SiC paper 800 grit	4 min	250	20-25	Water
	SiC paper 1200 grit	4 min	250	20-25	Water
Polishing	Hard, woven cloth with 6 μm diamond suspension	3 min	150	20-25	Water based
	Short napped velvet cloth with 3 μm diamond suspension	3 min	150	20-25	Water based
	MicroFloc-Soft, long napped cloth with 1 μm diamond suspension	2 min	150	20-25	Water based
	MicroFloc-Soft, long napped cloth with 0.25 μm diamond suspension	1 min	150	20-25	Water based

Table 4.4: Grinding and polishing procedure

Etchant name	Chemical composition	Etching time [s]	Temperature [°C]	Etching method
Keller	950 ml H2O; 25 ml HNO3; 15ml HCl; 10 ml HF	10	25°C	Immersion
Macro Etchant (Cu)	150ml Ammonium persulfate; 850ml H2O	5-10	25°C	Immersion

Table 4.5: Chemical composition of the etchant used for Cu-Al joints

4.3.4 Tensile shear test

The samples for the tensile shear test are prepared by placing the Cu and Al in overlapped configuration with an overlap distance of 15 mm. The schematic of the welded sample for the shear test is shown in figure 4.4. For the tensile shear test, the sheets are held in position by clamps at each end. The tensile shear test is carried out in the Zwick Z010 machine at room temperature (25°C) with 1.2 mm/min as feed rate of the crosshead. This particular value of feed rate is selected based on the works of [85] and [54]. The tensile shear strength of the materials is reported in terms of the shear force in Newton. The resisting cross-sectional area depends on the mode of failure. For weaker joints, the failure is in the interface and the resisting area is the area of the weld seam interface. If the failure is on the Al side the resisting area is the thickness and the joint failure is in tensile mode.

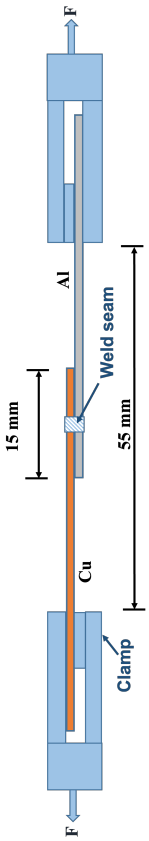

Figure 4.4: Schematic of tensile shear test for Cu-Al joints

4.3.5 Setup for process monitoring

The online process monitoring of the laser welding process (chapter 7) is demonstrated with disk laser (1030 nm) from TRUMPF, integrated with a high-speed scanner optic system from blackbird

(manipulation of laser beam trajectory), which is available at the University of Luxembourg. This particular scanner system was selected because of the integrated air cooling system and it provides better accuracy of mirror movement which is needed for beam oscillation in a production environment. The positive airflow inside the optic system protects the lens against spatter, which is commonly formed while welding Al and Cu. High power 1030 nm lasers in combination with an air-cooled scanning system are widely used for industrial applications.

Welding of metals with high-intensity laser is accompanied by emission of vapour plume/ metal vapour of the metal that is welded. For the analysis described in Chapter 7, a spectroscope is used for detecting the whole range of wavelengths and their associated peaks. Since the data sampling rate is only 1000 Hz, the analysis only aid in the study of the peaks that are formed during the welding that can form the basis for high-speed data acquisition with photodiodes. For this purpose, a spectrometer from Oceanoptics (HR2000+) with a resolution of 0.3 nm is used. The range of wavelengths measured is from 200 nm to 1100 nm. The process light is collected from the welding area from the off-axis position (Position 2 in figure 4.5) and analysed by the spectrometer.

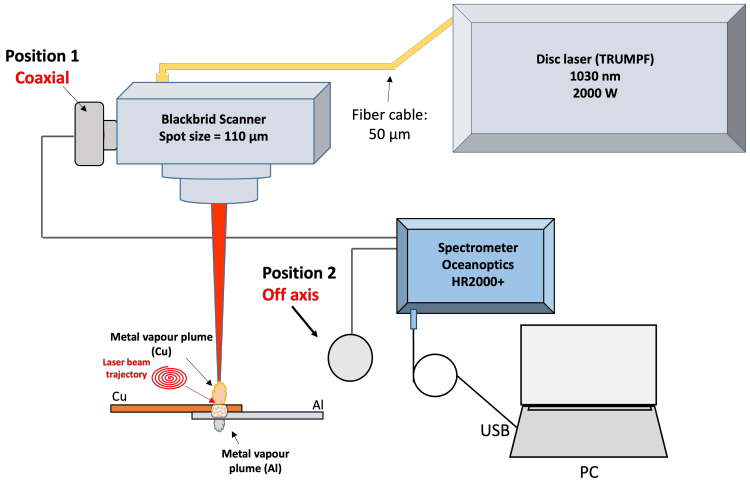

Figure 4.5: Schematic showing the off-axial and coaxial locations for analysis of emission spectrum during welding of Cu-Al

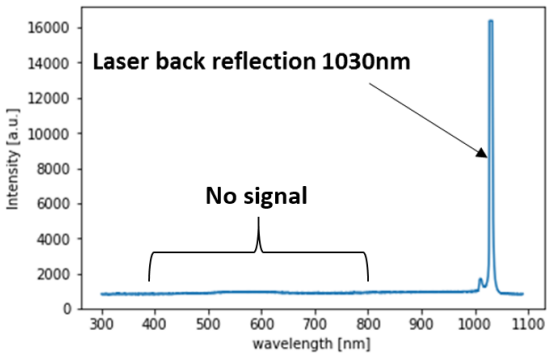

Figure 4.6: Spectrum of Cu-Al laser welding, measured by the spectrometer at coaxial position (position 1) could not detect the process emission in the wavelength range of 390-700 nm.

The plot in figure 4.6 shows the spectrum collected from position 1 (figure 4.5), which could not show the specific peaks of Al-Cu welding. So, coaxial measurement of the process light through the laser optic (Position 1) was not suitable because of the coating applied on the lens of the scanner system for protection against back reflection and UV radiation. Furthermore, the signal was found to be very weak. Therefore the off-axis method (position 2 in figure 4.5) was chosen in this thesis and the experimental results at this position can be easily implemented across different laser systems and manufacturers.

For high-speed data collection of specific wavelengths, filters are applied to the photodiode. The figure 4.7 shows the setup and the locations of the photodiodes for analysis of optical emission during welding. The process light is collected away from the optic head, i.e., an off-axis position. Data sampling is done at 100 kHz. The photodiodes used were from Thorlabs (PDA 100A) and the data acquisition was done using a National instrument device (NI cDAQ-9171). A summary of the spectrometer and photodiode specifications used in this thesis are reported in table 4.6

Device	Sampling rate	Position	Data acquision
Spectrometer(Oceanoptics HR2000+)	1 kHz	Off-axis	Seabreeze, Python
Photodiode (Thorlab-PDA 100A)	100 kHz	Off-axis	Python interface-NIDAQmx

Table 4.6: Specification of the sensors used

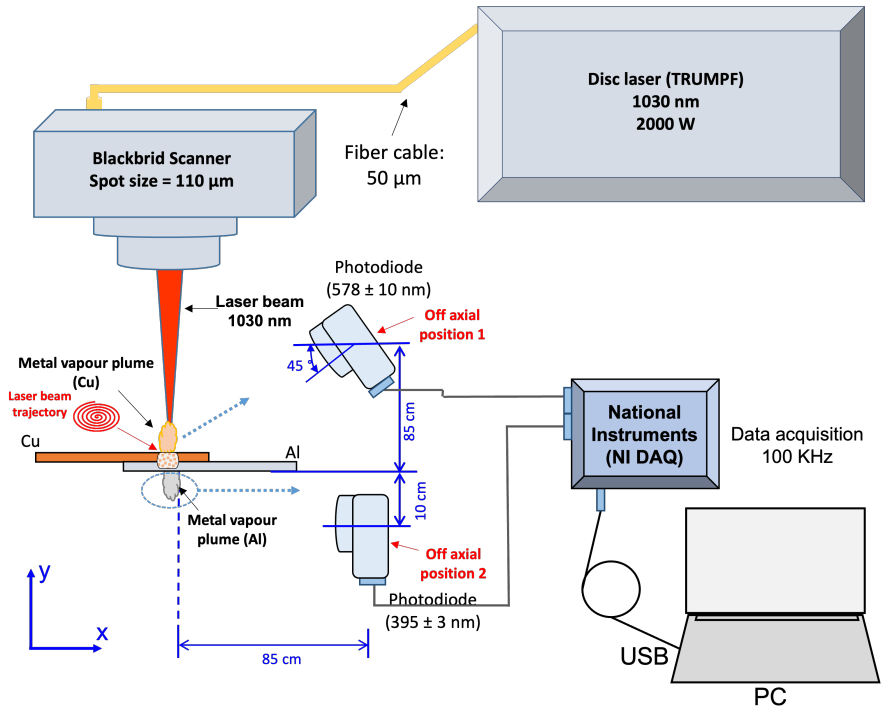

Figure 4.7: Schematic showing the locations of the photodiode to record the optical emission during welding of Cu-Al

A band-pass filter of 578 nm (578 +/- 10 nm) was fixed to the photodiode (off axial position 1) which is placed on the top side of the overlapped sample (Cu top) as shown in figure 4.7. The photodiode was placed at a height of 85 cm from the base of Al sheet. The photodiode was inclined at a angle of 45 ° to the x-axis (horizontal axis) as shown in the figure 4.7.

A band-pass filter of 395 nm (395 +/- 3 nm) was installed to the photodiode (off axial position 1), which is placed under the Al sheet at a height of 10cm to collect the process light (weld plume) from the bottom side of the overlapped Cu-Al sheets. Both the photodiodes were placed at a distance of 85 cm from the weld zone in the x-axis.

The measurement point is not static, i.e., the sensor is not moving but the laser beam moves across the workpiece. This approach is maintained because high-speed laser trajectory or beam manipulation currently is not possible with the moving table (setup with moving the fixture). Only fast scanning optic systems can achieve high-speed manipulation of the laser trajectory as the fixture unit is stationary. Integration of the diodes into the optical path of the laser blocks a certain wavelength of light. Therefore, the sensor is maintained static as the laser beam moves.

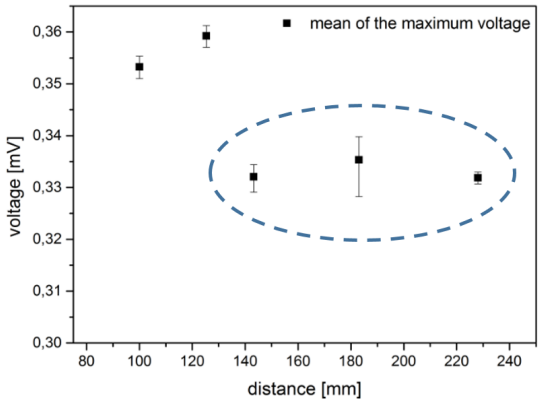

Figure 4.8: Influence of distance from the weld zone to the photodiode [89]

The distance from the sensor to the welding point has a small influence on the signal value for the distance greater than 140 mm [89]. As shown in the figure 4.8, for changing the location of the photodiode from 140 mm to 180 mm, the mean value of the signal is not changed significantly. In this research, the positions of the diodes with respect to each sample (for different welding parameters like laser power and velocity) were never changed during the entire experiment, i.e., the distance between the welding zone to the photodiode is not changed.

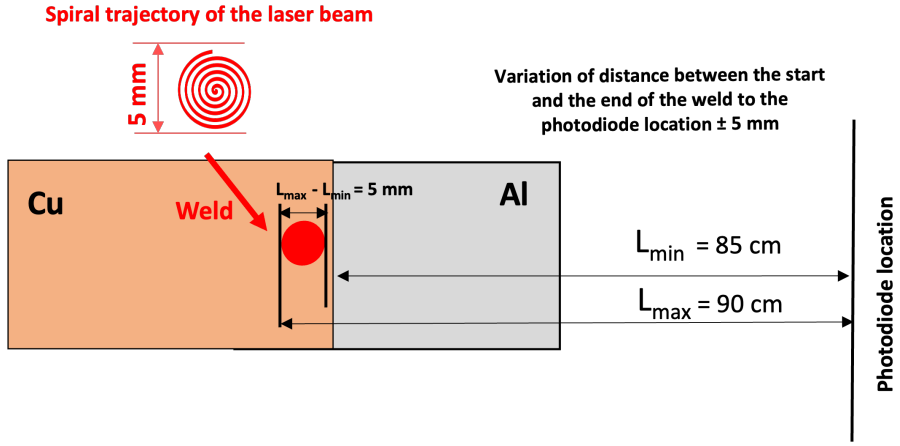

Figure 4.9: Sketch of changing distance from the welding zone to the diode location

The spiral laser trajectory is used for welding because the weld zone is confined to a small field of 5 mm x 5 mm by selecting the spiral diameter to be 5 mm. This particular welding trajectory is selected so that the variation of distance from the welding zone to the photodiode is small, i.e., a spiral diameter of 5 mm as shown in the figure 4.9. The chosen setup and welding approach minimizes the variation of the distance between the welding zone and photodiode location.

Therefore the selected spiral trajectory (laser movement) and photodiode setup (static position)

allow for both creating a good weld and at the same time allows for signal acquisition with minimal distance variation during the welding process. The figure 4.10 shows the clamping of Cu and Al sheets using a support plate. The support plates are pressed on to the Cu-Al sheets using toggle clamps on either sides of the sheets. The clamping was employed only to avoid the air gap between the Cu-Al sheets.

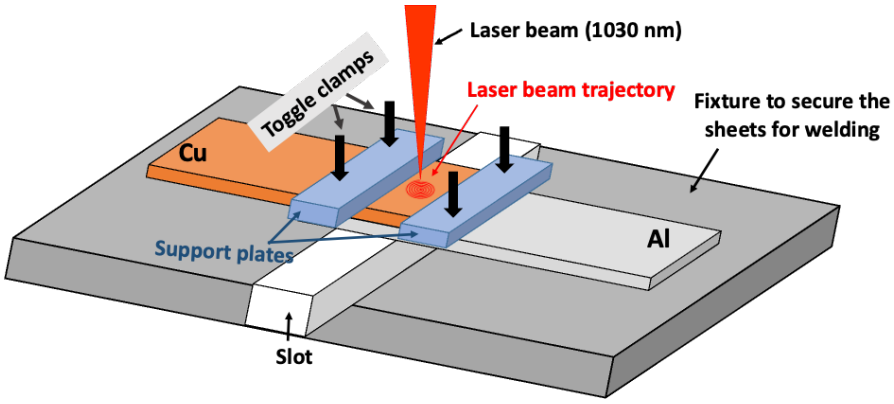

Figure 4.10: Schematic showing clamping of Cu-Al sheets

In addition to the spiral laser trajectory, a simple line trajectory is also investigated in chapter 7. A simple linear movement of laser from the start point to an endpoint is shown in figure 4.11. The length of the weld is selected to be 5 mm so that the field of view of the photodiode sensor is always facing the weld zone. Moreover, with the small weld length of 5 mm the variation of distance from the welding point to the sensor is small (5 mm).

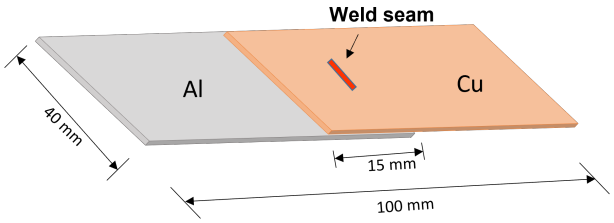

Figure 4.11: Schematic of line trajectory

The plot in figure 4.12 shows an example of applying the mean window to the raw signals (Al and Cu signals at 396 +/- 5 nm and 578 +/- 10 nm respectively). In order to smooth the acquired raw photodiode signal, averaging of the signal was performed by a moving average method (rolling average) over 25 data points or a window of size 0.25 ms (also known as moving mean). This step is done only to smooth the raw signal. However, the trend of the signal over time is not altered significantly.

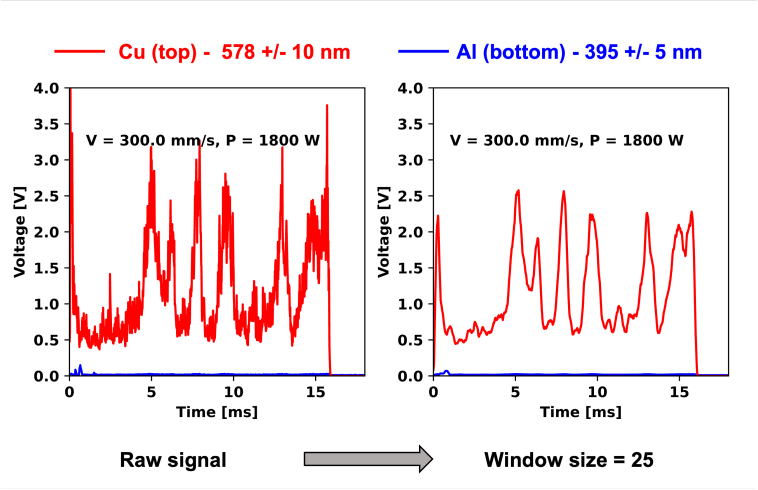

Figure 4.12: Example of applying a rolling mean window of size 25 (0.25 ms) to the Al and Cu signals obtained during welding with laser power of 1800 W and velocity of 300 mm/s

4.4 Experimental approach for image classification by a convolutional neural network (CNN)

A schematic representation of the workflow for the convolutional neural network (CNN) model training and prediction is shown in figure 4.13.

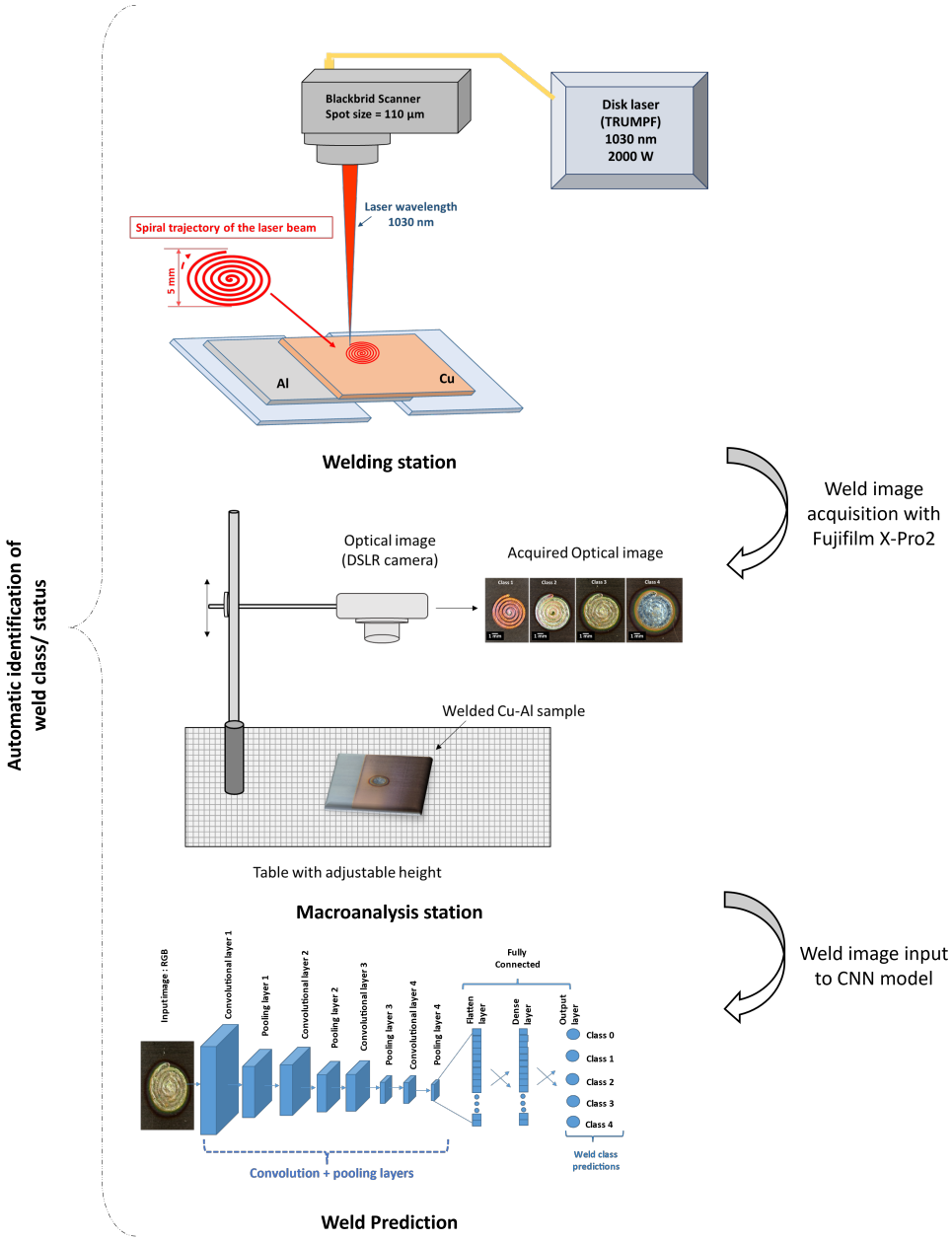

Figure 4.13: Workflow for prediction of weld class using CNN, starting from the digital image acquisition and model training

The first step in the non-destructive identification of the weld class/ weld status is the laser welding process itself, which is done in the laser cabin or welding station. After the welding process is completed, the sample is transferred to the macro-analysis station which is equipped with a height-adjustable stand where the digital camera is securely mounted. The digital camera from the company Fujifilm model "X-Pro20" is used for acquiring the images at a resolution of 6000 $\times$ 3376 pixels. The acquired images are exported to a commercial laptop in PNG (Portable Network Graphics) format. Then the raw images are resized to a final size of 540 x 550 pixels which is an input for the CNN model architecture for the prediction of the weld status.

Chapter 5

Welding Copper to Aluminium with spiral trajectory

The results of welding Cu-Al with spiral trajectory is discussed in this section starting with the tensile shear test, cross-sectional analysis and SEM (Scanning Electron Microscope)- EDS (Energy-dispersive X-ray spectroscopy) analysis of the fusion zone. Some of the terminology used for different weld types are insufficient weld, low weld, good weld and high or excessive weld. The insufficient weld is a condition where the Cu and Al melted is not sufficient to form a joint. A low weld condition is a result of melting a small amount of Cu and Al at the interface and the weld is weak. A good weld is a condition where the melted Cu and Al are optimum and result in a strong joint. The high and excessive weld is the weld condition where the more than optimum Cu and Al is melted to form a welded joint. Some of the names for different weld conditions are interchangeably used as described below.

1. Insufficient weld - low weld - weak weld
2. Good weld - optimum weld - acceptable weld - strong weld
3. Excessive weld - High weld - unacceptable weld

These conditions will be explained in the following sections in detail.

5.1 Tensile shear force

The tensile shear force of the weld is shown in figure 5.1 for different laser powers of 1600 W, 1800 W, 1900 W and 2000 W and laser velocities of 200 mm/s, 300 mm/s, 400 mm/s, 500 mm/s, and

600 mm/s.

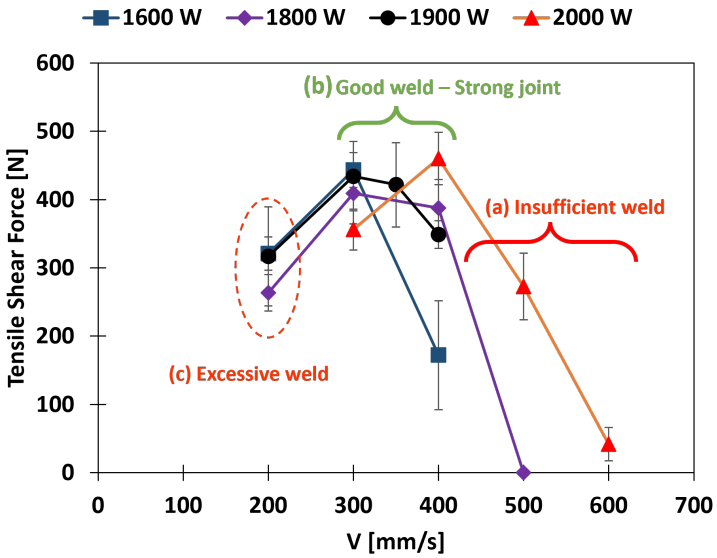

Figure 5.1: The tensile shear force of Cu-Al laser welded for different laser powers and velocities

For the low laser velocity of 200 mm/s, the mean tensile shear force is in the range of 280-320 N. Increasing the laser velocities to 300 mm/s and 400 mm/s, the mean tensile shear strength of the weld is in the range of 380 - 460 N, except for low laser power of 1600 W. Further increasing the velocities to 500 mm/s and 600 mm/s, the mean weld strength is reduced below 300 N for all the laser powers. From the tensile shear test results, it can be concluded that the velocity of 300 mm/s and 400 mm/s resulted in a high value of tensile shear force in the range of 360-480 N.

The laser energy input per unit length (J/mm) is calculated by the laser power (W or J/s) divided by the velocity (mm/s) ie. laser power/laser velocity. Depending on the laser velocity and power, different energy per unit length is obtained. Different weld types are identified from the tensile shear force value and the laser energy per unit length input as shown in figure 5.2. The figure 5.3 shows the top view of the Cu sheet for different weld types such as insufficient weld, good weld and excessive weld. For low laser energy of 4 J/mm, the weld is weak (low tensile shear force value) and less amount of Cu and Al is melted in the weld zone. This condition is termed as an insufficient weld. For laser energy of 4.6 – 6 J/mm, the weld is strong and a sufficient amount of Cu and Al is melted in the fusion zone and this condition is termed as a good weld. For energy over 6 J/mm, the weld is weak, excessive Al and Cu is melted in the fusion zone and the weld is termed as an excessive weld.

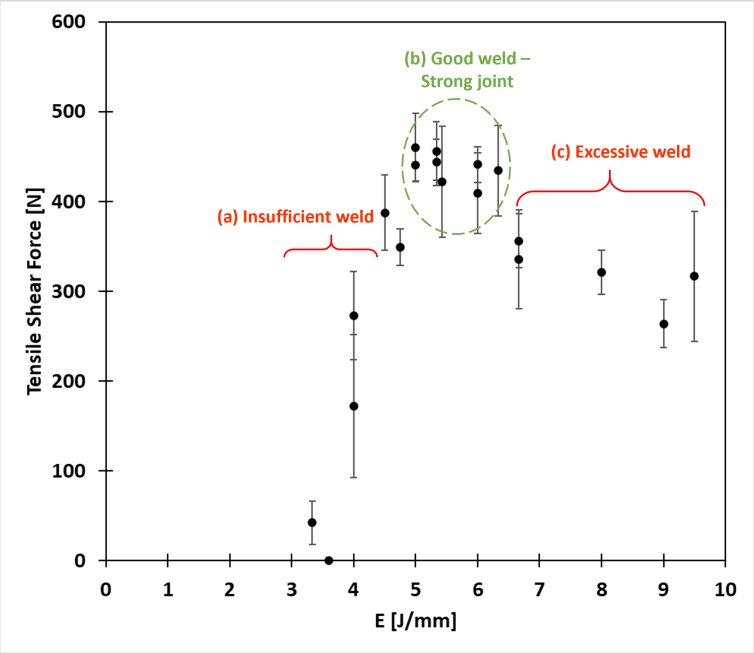

Figure 5.2: Effect of laser energy input per unit length on the tensile shear force

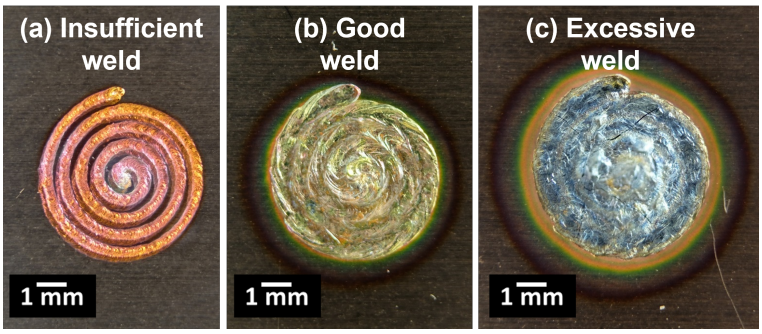

Figure 5.3: Images of weld on top of Cu for different weld conditions like (a) Insufficient weld, (b) Good weld and (c) Excessive weld

5.2 Elongation during the tensile shear test

The cross-head displacement or the elongation of the welded sample is a good measure of the weld ductility. The plot of tensile shear force and the cross-head displacement at maximum force is shown in figure 5.4.

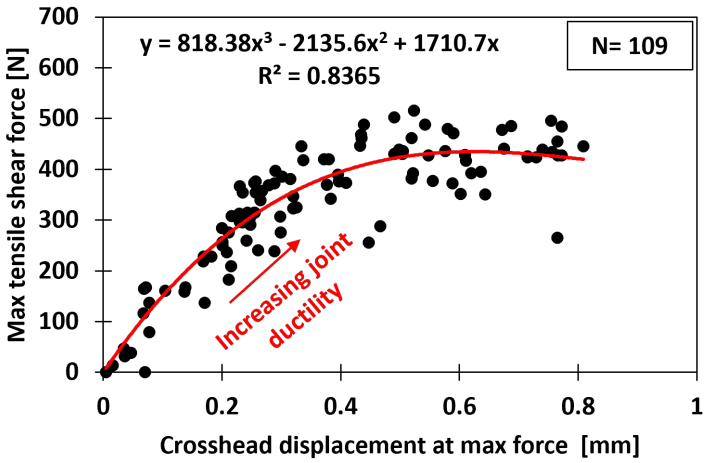

Figure 5.4: Plot showing the relation of crosshead displacement to the tensile shear force

The tensile shear force and the cross-head displacement is fitted with a polynomial function as shown in the figure 5.4 with the R-squared value of 0.83, which is a good fit of the line to the data. The results show that the tensile shear force is proportional to the cross-head displacement. The welds with high tensile shear force tend to have higher cross-head displacement. For an insufficient weld, the tensile shear force is less than 300 N and the cross-head displacement is lower than 0.2 mm. In contrast for a strong joint both tensile shear force and the cross-head displacement is very high with values of over 400 N and 0.38 mm respectively. For the excessive welds, the tensile shear force is less than 400 N and the cross-head displacement is less than 0.4 mm. The insufficient weld has a lower tensile shear force and cross-head displacement. On the contrary, the strong joint has both the values of tensile shear force and the cross-head displacement very high. However, for the excessive weld, the tensile shear force is high and in some cases comparable to the strong joint but the cross-head displacement is low. Therefore the tensile shear force, cross-head displacement or combined values can be used for indication of a good (ductile) or bad weld (brittle).

The plot (figure 5.5) shows the tensile shear force value and its corresponding cross-head displacement (elongation) during the tensile shear test for different weld conditions. For a good weld, the shear force-displacement curve is significantly larger in comparison to the low weld and high weld conditions. The tensile curve for a good weld shows that the behaviour of the good weld is ductile in comparison to the low weld and high weld.

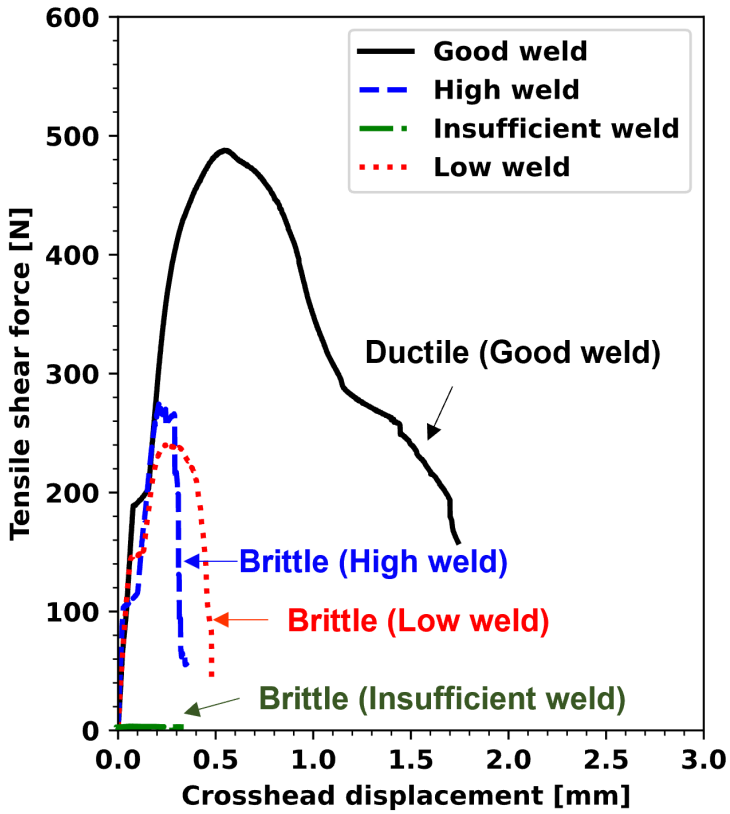

Figure 5.5: The plot of crosshead displacement [mm] versus the tensile shear force [N] for different weld conditions such as insufficient weld, low weld, good weld and high weld

5.3 Beneficial composition in Cu-Al welding

The laser welding of Cu and Al results in the formation of different phases such as Al, $Al + Al_2Cu$, $Al_2Cu, Al_3Cu_4, Al_4Cu_9$, Cu as outlined in the phase diagram (figure 5.6). Among these phases, the Cu rich phase (81.5-100 atomic % of Cu) and the Al-rich phases (0-30 % at of Cu) are beneficial phases, since these phases are ductile. The composition of 50 - 81.5 atomic % of Cu results in detrimental composition (detrimental intermetallic compounds). These phases are identified by SEM-EDS analysis and marked in the SEM (figure 5.7(a)) and the corresponding optical image (figure 5.7(b)). The region between 30-50% Cu is not a beneficial composition. Therefore the region between 30-81.5 atomic % of Cu is not a advantageous composition in the fusion zone.

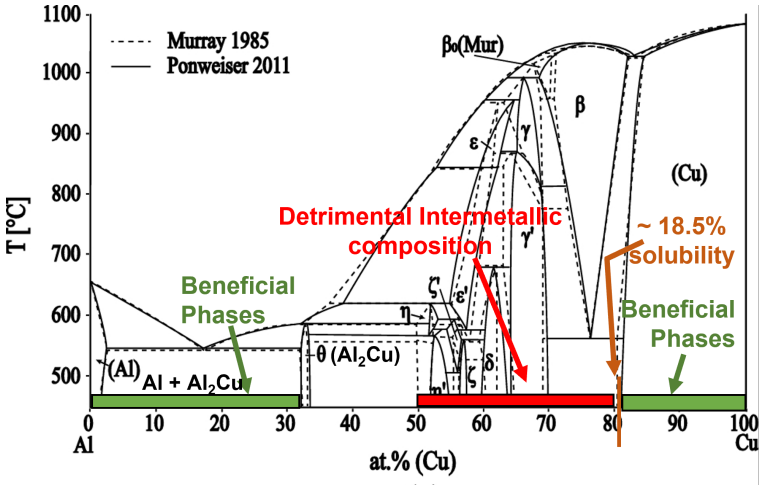

Figure 5.6: Phase diagram of Cu and Al showing beneficial and detrimental phases

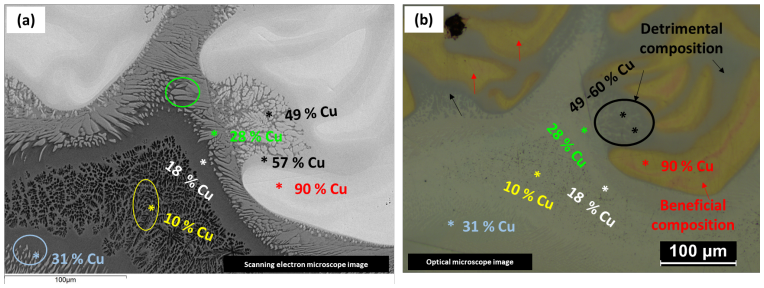

Figure 5.7: (a) SEM and (b) optical image of the Cu-Al weld showing detrimental and beneficial regions

The Al-rich phases appear dark in the SEM image and light grey in the optical microscopic image. The beneficial Cu rich phase (90% at of Cu) appear bright in the SEM image and yellow colour in the optical microscope image. The detrimental phases (50 - 81.5 % at of Cu) appear dark grey in colour in the optical microscopic image. The detrimental phases are mainly found between the beneficial Cu and Al-rich phases as shown in figure 5.7(a) and (b).

5.4 Cross-section analysis of Copper to Aluminium

The welding of Copper and Aluminium by spiral trajectory movement of the laser beam results in a circular profile (in contrast to the linear welds). The mixing of Cu and Al metals across the joint interface is analysed by sectioning at the centre of the weld zone i.e., at the centre of the spiral. Since the weld profile is circular rather than linear, the analysis of the cross-sections can be considered symmetric in comparison to the linear weld trajectory, for cross-sectional view and the

lateral section view i.e., sectioning the weld in the parallel and perpendicular direction to the weld seam.

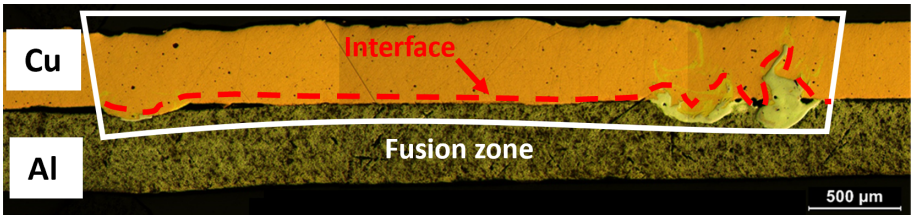

Figure 5.8: Cross-sectional image of the low weld condition

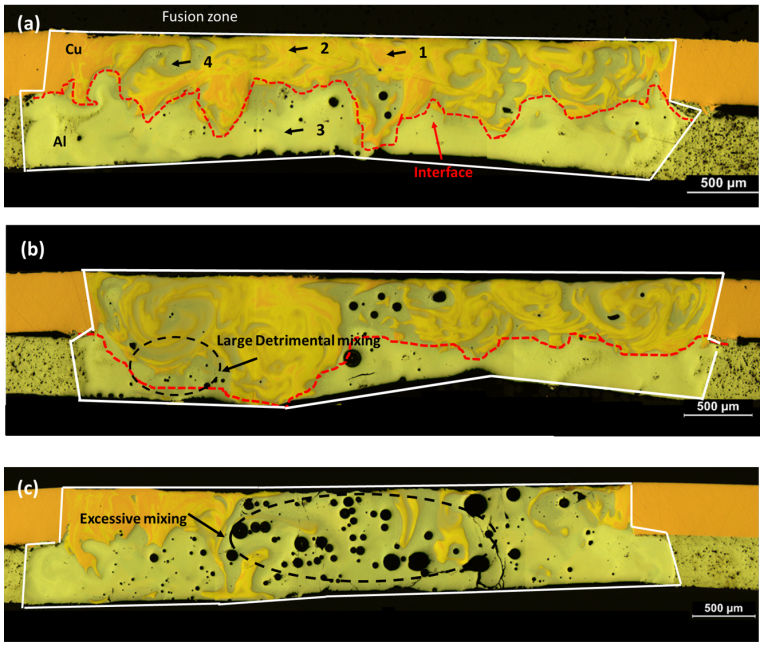

Figure 5.9: Cross-section view of the Cu-Al spiral weld trajectory for (a) good weld, (b) high weld and (c) excessive weld conditions

The light optical microscopic image of the cross-section of the Cu-Al fusion zone for low weld is shown in figure 5.8 . For low weld, the fusion zone formed between the Cu and Al sheet is shallow with a depth of 0.6 mm. A small quantity of Al is melted and mixed with the Cu to form a weld interface. The movement of Al into the Cu and Cu into the Al is low.

The cross-section view of the strong weld (optimum weld) is shown in figure 5.9 (a). For the optimum joint, the fusion zone is formed to a full depth of 0.8 mm. Because of the deeper weld in comparison to the low weld condition, a higher amount of Al and Cu is melted and fused to form the fusion zone. Due to the wider Cu and Al melt and the laser trajectory in a spiral shape, the formed interface appears wavy. several beneficial phases are formed in the fusion zone like Al+Al_2Cu, Cu

and Al. The presence of the Cu phase which is marked by arrow 1 in 5.9 (a) at the interface provides an anchoring effect in addition to metallurgical bonding to the bottom Al sheet. The weld fusion zone formed is a combination of brittle and ductile phases. The total effect of the combined brittle and ductile phases is that a superior joint strength as shown in the tensile shear result is obtained.

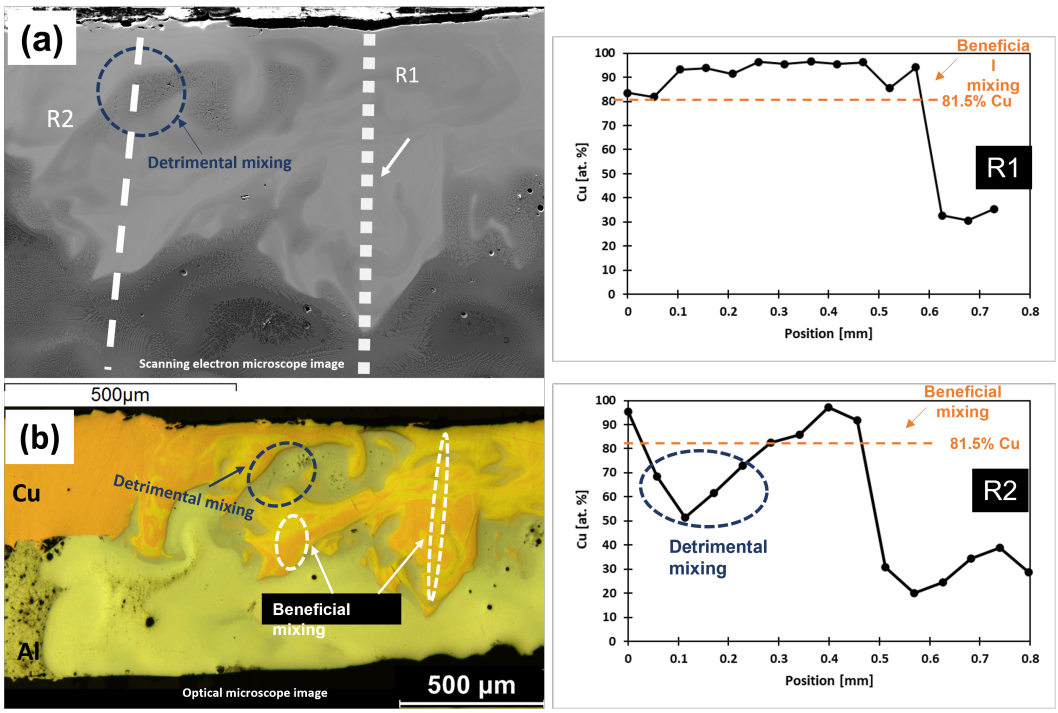

Figure 5.10: (a) SEM and the corresponding (b) optical image of the good weld. The composition of Cu in at% is shown for selected regions R1 and R2

The SEM and optical microscopic images are shown in figure 5.10 (a) and (b) respectively for the optimized weld. Because of the larger melting of Al and Cu, several phases are formed in the fusion zone. To understand the composition of Al and Cu in the fusion zone, EDS line scanning is performed in two different locations (lines R1 and R2) starting from the Cu (top) to the interface and Al (bottom). Fifteen equidistant points are taken for lines R1 and R2 for a total length of 0.7 and 0.8 mm respectively. For line R1 the composition of Cu is over 80 at % until the distance of 0.6 mm. Further passing the interface over the depth of 0.6 mm amount of Cu decreases to 30 at %. The top portion of the line R1 until 0.6 mm the phase formed is Cu (Cu rich - 81.5 %Cu) which is a beneficial phase. Only a small quantity of Al (5- 19.5 %at) is intermixed and the Cu rich phase is present at the interface. In contrast for line R2, the composition of Cu at the start is 96%. After 0.05 mm the Cu content decreases below 81.5 % until 0.3 mm. Over 0.3 mm amount of Cu increases to 81.5 % and continues to increase until 0.5 mm. The Cu % decreases significantly to a value of 30 % after 0.5 mm. The region between the 0.05 to 0.3 mm of line R2 has the Cu content in the

range of 81.5- 50% which is a detriment composition. The region between 0.3 mm to 0.5 mm is a beneficial Cu phase. Therefore the detrimental intermetallic composition is present in between the ductile phases. In the strong joint the melt formed at the interface is a stronger Cu based beneficial phase and the detrimental phases are intermixed and distributed in between the ductile phases.

The SEM image of the strong joint (good weld) is shown in figure 5.11 (c). The figure 5.11 (a) and figure 5.11 (b) shows the selected regions at the interface of the strong joint.

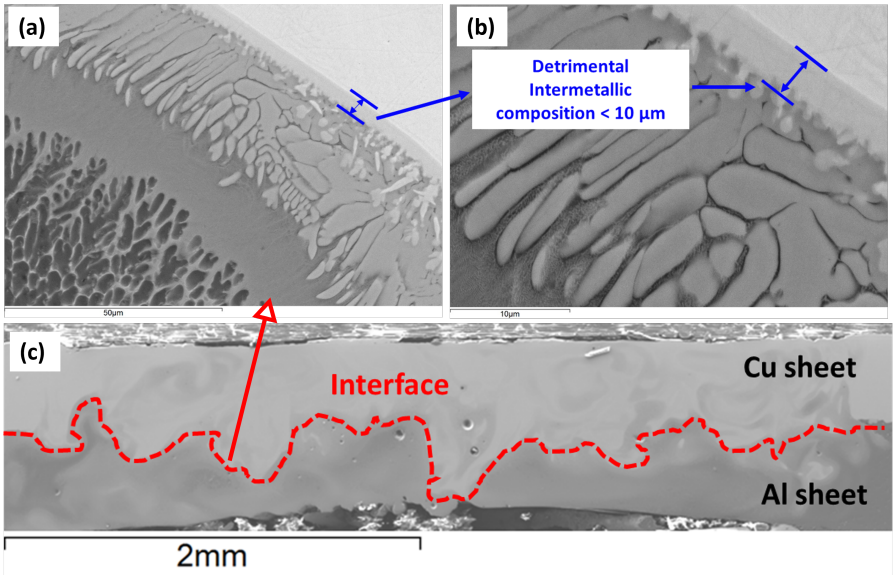

Figure 5.11: (a) Microstructure at the joint interface (b) Detrimental intermetallic composition (Al_3Cu_4) at the interface, (c) SEM image of the good weld showing the wavy interface formed between Cu and Al sheet

It can be seen in figure 5.11 (c) that the interface formed between Cu and Al is wavy. At the interface, the microstructure formed is mainly Al-rich dendrites and the detrimental intermetallic composition (81.5-50% of Cu) are thin as shown in figure 5.11 (c).

As the laser input energy is increased, more Al in the bottom sheet is melted and it intermixed with the molten Cu as depicted in the cross-section of figure 5.9 (b). Because of the increased Al melt in comparison to the condition as shown in figure 5.9 (a), more of the Al and Cu intermix to form an even higher amount of beneficial Cu phase but the amount of detrimental intermixing is also increased in the fusion zone. The wavy interface is not as pronounced as in the previous case 5.9 (a) due to more Al and Cu intermixing, to form mixed phases for the complete fusion zone depth and width.

Complete mixing of Cu and Al happens for further increasing the laser energy as shown in figure 5.9 (c) and this condition is an excessive mixing of Al and Cu in the fusion zone. Complete mixing leads to the formation of a fully mixed composition and the absence of a beneficial Cu phase. The

wavy interface is not present as a result of the complete intermixing of Al and Cu. The fusion zone in this condition has significantly higher pores and cracks. This condition is unacceptable as the fusion zone resulted in excessive mixing of Al and Cu and the absence of beneficial Cu phase providing the anchoring effect as explained in an optimum weld in figure 5.9 (a).

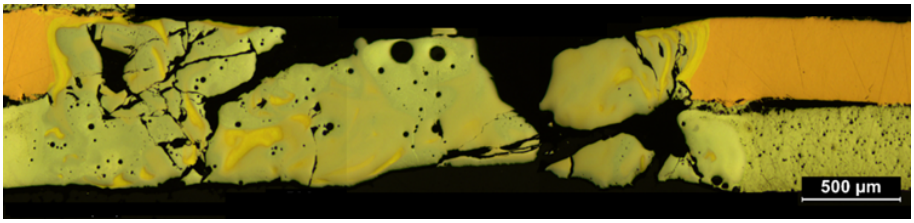

Figure 5.12: Cross-sectional view of excessive weld condition

The cross-section view of an excessive weld obtained by applying even higher laser energy than the previous condition is shown in figure 5.12. In this condition because of high laser input energy, larger melting of Cu and Al happened. As a result, all the Al and Cu are intermixed. The beneficial Cu rich phases are not present in the fusion zone and excessive intermetallic compounds are formed. The high brittleness of the joint led to the formation of large cracks in the fusion zone across the interface. Despite the large cracks and brittleness of these joints, the welded samples did not separate.

5.5 Morphology of weld zone

In this section, the microstructures formed in the Cu-Al weld is analysed to get insights into the morphology and its composition. The SEM image in figure 5.13 shows a selected location where the Cu melt is fused to the Al to form a local interface.

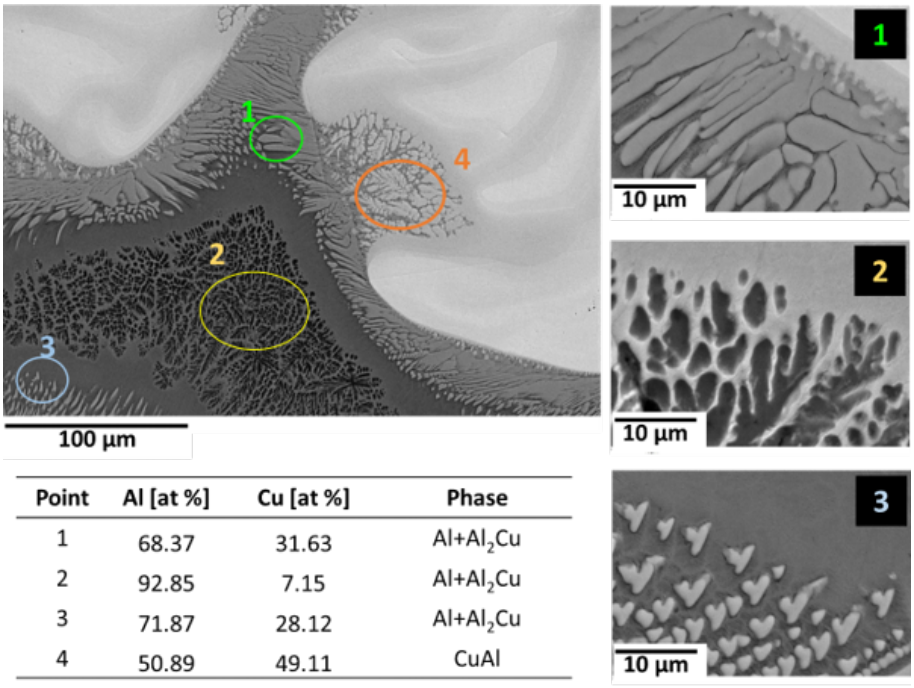

Point	Al [at %]	Cu [at %]	Phase
1	68.37	31.63	Al+Al_2Cu
2	92.85	7.15	Al+Al_2Cu
3	71.87	28.12	Al+Al_2Cu
4	50.89	49.11	CuAl

Figure 5.13: Morphology of Al-rich structures in the fusion zone

The Al-rich phase Al+Al_2Cu in the weld seam has distinct morphology. Because of the strong fluid flow accelerated by the laser beam, local interfaces are formed which appear like a wave along with the Al and Cu sheet. The Al+Al_2Cu phase is found to have distinct structures 1, 2, 3 as shown in the figure 5.13. Structure 1 is formed close to the Cu zone and has a higher amount of Cu content of around 31.63 at%. The size of this dendrite structure is in the range of 10 - 60 μm. Structure 2 has 92.85 % Al and the size of the structure is about 3 - 10 μm which is relatively small compared to structure 1. Structure 3 with 71.7 % Al has a smaller structure of about 2 - 6 μm. These structures are mostly found on the Al side of the fusion zone. Structure 4 with Al and Cu composition of about 50% is the intermetallic phase CuAl and is found just next to the Cu melt zone where a higher mixing ratio of Cu and Al is favourable. Out of these phases, structure 4 is a detrimental phase and the other Al-rich structures 1, 2, 3 are relatively ductile and are desired. As with the laser welding process, a wide range of mixing ratios is possible, the formation of the detrimental phases cannot be avoided. It is important to point out that the combination of the

ductile Al-rich phases 1, 2, 3 and the intermetallic phase strengthen the joint as these phases are mixed to form the welded joint.

5.6 Failure analysis

The schematic representations of the failure locations and the corresponding optical images are shown in figure 5.14.

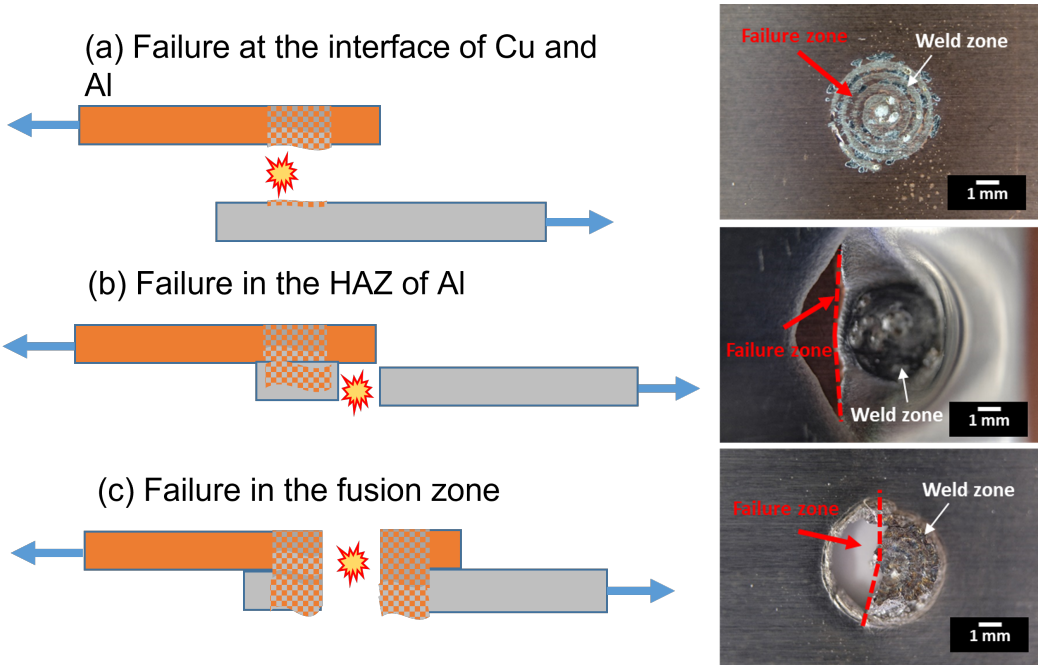

Figure 5.14: Schematic of the failure locations for different weld conditions after the tensile shear test. (a) Failure at the interface of Cu and Al (b) Failure in the Heat Affected Zone (HAZ) of the Al (c) Failure in the fusion zone or weld failure

The mechanical performance of the Cu-Al joint was explained in the previous section (section 5.2) in the tensile shear test. However, it is important to also understand the location of the failure and its relation to the mechanical strength. Three distinct failure locations for the joints are identified for the Cu-Al welds which are (a) failure at the interface, (b) failure at the Al HAZ and (c) failure at the fusion zone.

For insufficient welds the amount of Cu and Al melted in the fusion zone is very low and the joints failed at the interface between the Cu and Al sheets. Figure 5.14 (a) shows the Cu sheet of the failed weld joint, where traces of the fused Al can be seen. The applied pulling force separated the Cu and Al sheet at the interface due to insufficient melt and as explained in the cross-section analysis (figure 5.8 (a)) there is no beneficial Cu phase at the interface providing an anchoring effect.

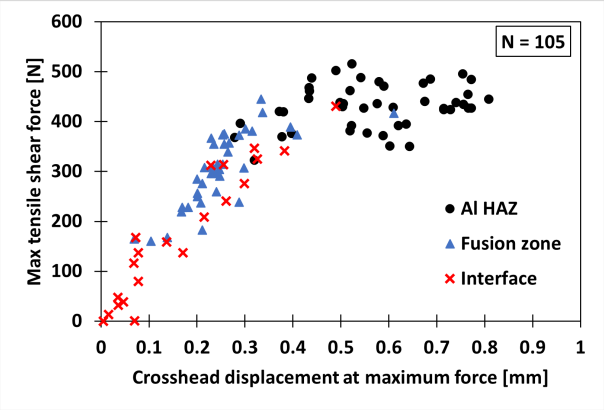

Figure 5.15: The plot of tensile shear force and crosshead displacement for different failure locations such as Al HAZ failure, fusion zone failure and interface failure.

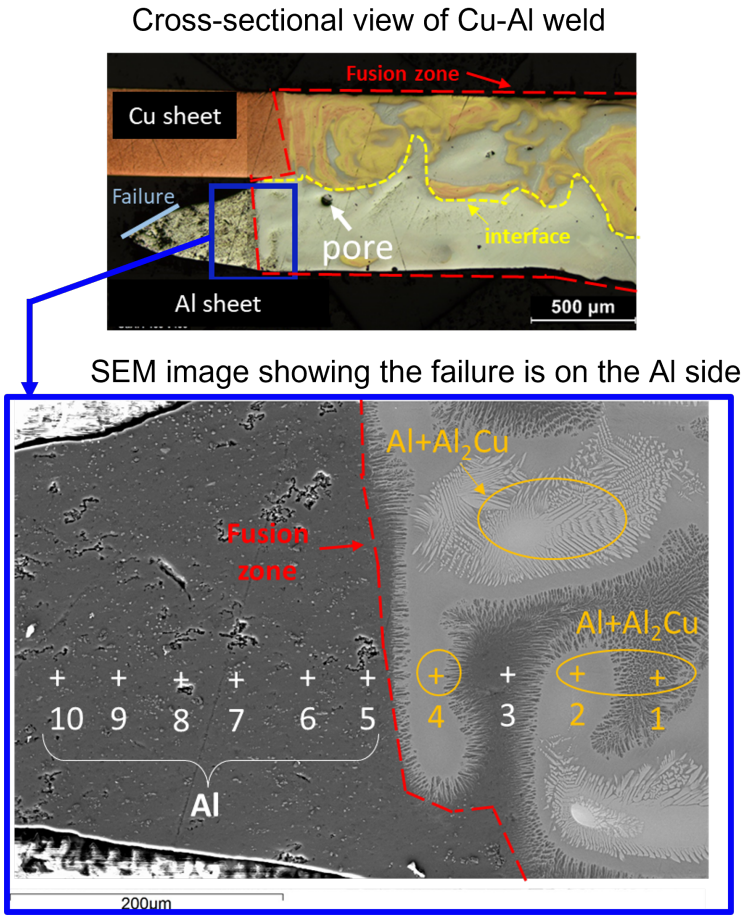

Figure 5.16: SEM image of the Cu-Al joint for good weld (strong joint) showing that the failure region is located on the Al side.

In the case of the strong weld (optimum weld), the high value of shear force over 400 N and the

cross-head displacement at maximum force of 0.8 mm (elongation) was obtained as shown in figure 5.15. It is seen from the analysis of the fracture zone as shown in the SEM image in figure 5.16, the failure happened at Al material in the HAZ rather than the fusion zone. The failure location shifted to the Al material since the weld fusion zone is stronger than the case (a). An explanation for the higher tensile shear force and ductility is due to the fact that Al material is involved during the tensile shear test as the fusion zone was stronger than the Al material. This type of welded joint is preferred over the case (a) as best mechanical performances like the tensile shear strength and the ductility is achieved.

The failure for the Cu-Al joints happened at the fusion zone for the excessive welds as shown in figure 5.14 (c). In this condition, the fusion zone was mainly involved during the tensile shear test rather than the Al material, as the weld fusion zone was weaker than the base Al material due to the presence of excessive intermetallic phases. The fracture happened at the middle of the Cu-Al fusion zone where the excessive intermetallic phases are present as shown by the red line on the Al sheet in figure 5.14 (c) . The presence of excessive intermetallic phases and the absence of beneficial phases like Cu and Al phases increase the brittleness of the joint.

5.7 Optimum melting of Al for strong joint

Welding of Cu and Al has a higher tendency to form various intermetallic phases. However, there are phases that are more ductile than the intermetallic phases which must be the target of the welding process to achieve. In this thesis, the approach used was not to limit the intermetallic thickness but to increase the beneficial phases. It was shown in section 5.3 that the Cu and Al+Al_2Cu are relatively ductile phases in comparison to the intermetallic phases. For welding with the spiral laser trajectory, the weld joint can be summarized as a weak or strong joint depending on the amount of Al melted, resulting in beneficial phases like Cu and Al+Al_2Cu. The optimum melting (good weld) of Cu and Al at the interface is characterized by the formation of wavy appearance and the formation of localized Cu-Al interfaces. The melted Cu mix with Al in moderate proportions up to a maximum of 18.5 atomic % of Al, resulting in the formation of beneficial Cu phases, i.e., Cu content with over 81.5% at in the fusion zone. Such Cu rich phases increase the joint strength and ductility.

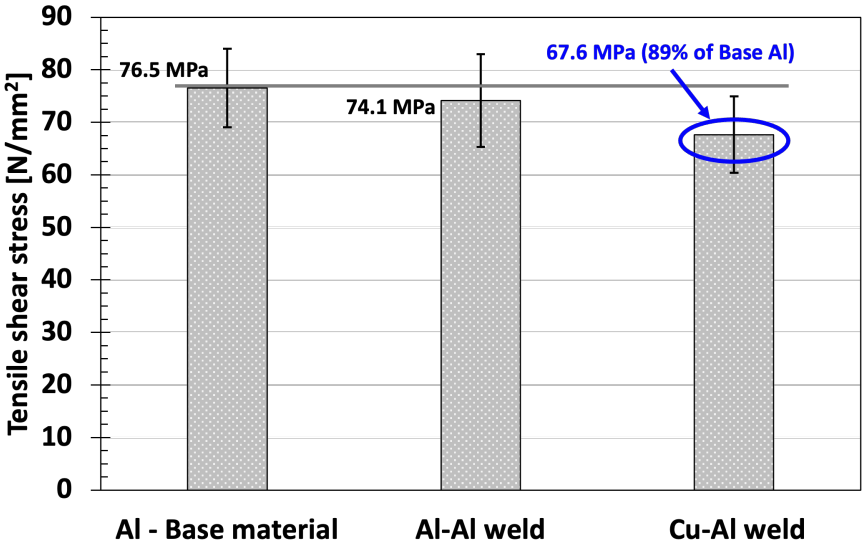

Figure 5.17: The plot of shear stress for Cu-Al weld and Al-Al weld

The plot in figure 5.17 shows the tensile shear strength of Al base material, Al-Al weld and Cu-Al weld. The Al material strength is chosen for evaluation since Al is the weaker material in comparison to Cu. The tensile shear strength of base Al is 76.5 MPa and for Al-Al welded samples the strength slightly reduced to 74.1 MPa. For Cu-Al welds, the tensile shear strength was reduced to 67.6 MPa.

The tensile shear stress in figure 5.17 was calculated by dividing the tensile shear force and the resisting area during the tensile shear test. For the strong joint, the resisting weld area is the product of the weld circumference and the thickness of Al sheet (3.141 $\times$ 5 mm $\times$ 0.4 mm = 6.28 mm^2). For the strong Cu-Al and Al-Al joints, the failure happened on the Al material. Therefore the Al thickness is considered. The mean shear force obtained for Cu-Al joints is 425 N which results in a tensile shear stress value of 67.6 Mpa (425 N/6.28 mm^2 = 67.6 N/mm^2).

From the Cu-Al tensile shear test results for spiral trajectory resembling a spot weld, a strong joint can be achieved. The strong weld achieves a strength of about 67.6 MPa which is about 89 % of base Al and the fracture happens at the Al sheet away from the fusion zone (figure 5.16).

5.8 Summary

The laser beam was effectively applied to Cu-Al joining (Cu irradiation), by fusion mode of welding. A strong metallurgical bonding is obtained by diffusion of Cu and Al as hypothesised, to form a more ductile phase in the weld region. A wavy interface was formed between the Cu and Al sheets and the interface is composed of mixed phases such as Cu (solid solution), Al+Al_2Cu, Al (solid

solution) and intermetallic composition. The effect of the detrimental intermetallic compounds is suppressed by the presence of ductile phases such as Cu (solid solution) and Al+Al_2Cu surrounding it, due to the intermixture in the fusion zone. The SEM-EDS composition study suggested that a mix of the ductile and brittle composition of Al-Cu is beneficial. A strong Cu-Al joint was achieved by welding with the spiral trajectory of the laser beam. The tensile strength of the Cu-Al weld was about 89% of the base Al material.

- Welding from the Cu side provides beneficial microstructure.
- The spiral beam trajectory effectively enlarges the weld seam diameter and provides beneficial intermixing with phases such as Cu solid solution and Al+Al_2Cu at the interface.

An automatic post-process analysis (quality analysis- Chapter 6)) and real-time weld analysis (Chapter 7) is of prime importance for indication of the weld status.

Chapter 6

Identification of the weld classes using the weld images

In welding Cu and Al sheets with a laser beam, it is important to optimize the melting of Cu and Al metals which is the key for a strong joint. Identification of such a strong joint without destruction of the welded sample is very critical for quality control. For mass production and autonomous welding, it is important that a model is required for weld qualification/ status identification. In this section different types of weld classes based on Cu and Al mixing on the top of the weld bead are identified for weld qualification. Optical analysis of the top bead (Cu sheet) is selected for identification, as it is rapid, nondestructive, and relatively inexpensive in comparison to destructive cross-sectional analysis of the weld seam. The use of automatic and nondestructive identification of weld types enables the implementation of quality checks for all the samples, which is expected to improve the product quality.

In the following sections, the analysis of the weld bead images by scanning electron microscope (SEM) and EDS analysis is discussed to show distinct features of the weld bead images. Later, the optical images of the different weld types are described by analysing their red, green, and blue pixel components. Finally, a CNN model is presented which can predict the weld class automatically. In this research high-resolution images of the weld zone are acquired and processed with a computer vision package. Furthermore, the images along with their weld class/types are fed to a convolutional neural network architecture (CNN) for training and prediction.

6.1 Analysis of weld images from the top of Cu

The description of different types of weld classes is provided in the table 6.1 and the top view (Cu) of welded images for different weld classes is shown in figure 6.1. Low laser energy value of less than 3.4 J/mm results in no weld. At low laser energy, the reflection of laser radiation by Cu is very high and there is no coupling of laser energy into the material. This condition is not suited for welding. This condition is termed as "No weld" or class 0. Increasing the laser energy to 3.4 J/mm results in penetration of Cu sheet, but the amount of Al melted is very small. This condition is called "Insufficient weld" or class 1. Further increasing the laser energy to 4.5 – 5.3 J/mm more of Al is melted in the fusion zone and is termed as "Low weld" or class 2. Laser energy of 5.3 - 6 J/mm results in a further increase of Al in the fusion zone and this condition is termed as "Good weld" (acceptable weld) or class 3. Increasing the laser energy to above 6 J/mm results in excessive Al in the fusion zone. This condition is termed as "High weld" or class 4. The laser energy applied per unit length is provided only as an overview to the resulting weld type.

Weld Class type	Description of weld status	Heat input [J/mm]
0	No weld	3.0 - 3.4
1	Insufficient weld	3.4 - 4.5
2	Low weld	4.5 - 5.3
3	Good weld	5.3 - 6.0
4	High weld	6.0 - 17.0

Table 6.1: Description of weld class/ type.

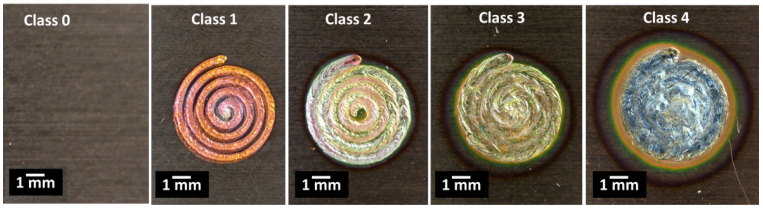

Figure 6.1: Top view of the optical images for different weld class type

6.1.1 Scanning electron microscopy analysis of the weld bead on top of Cu

The bead structures of the "Low weld/class 2", "Good weld/class 3" and "High weld/class 4" are analyzed using a scanning electron microscope (SEM). The weld bead is oriented in the direction of the laser beam as shown by the arrow in the case of a low weld as shown in figure 6.2 (a). The weld bead becomes flat as the intermixing of Al and Cu is increasing in the case of "Good weld" (figure 6.2 (b)), which is an optimum melt condition. Further increasing more of Al and Cu to mix, leads

to excessive intermixing and there is no visible bead track in the weld zone. A large crack of about 1-2 mm is found in the middle of the weld seam as shown in figure 6.2 (c), which is detrimental for the joint strength and is an unacceptable weld.

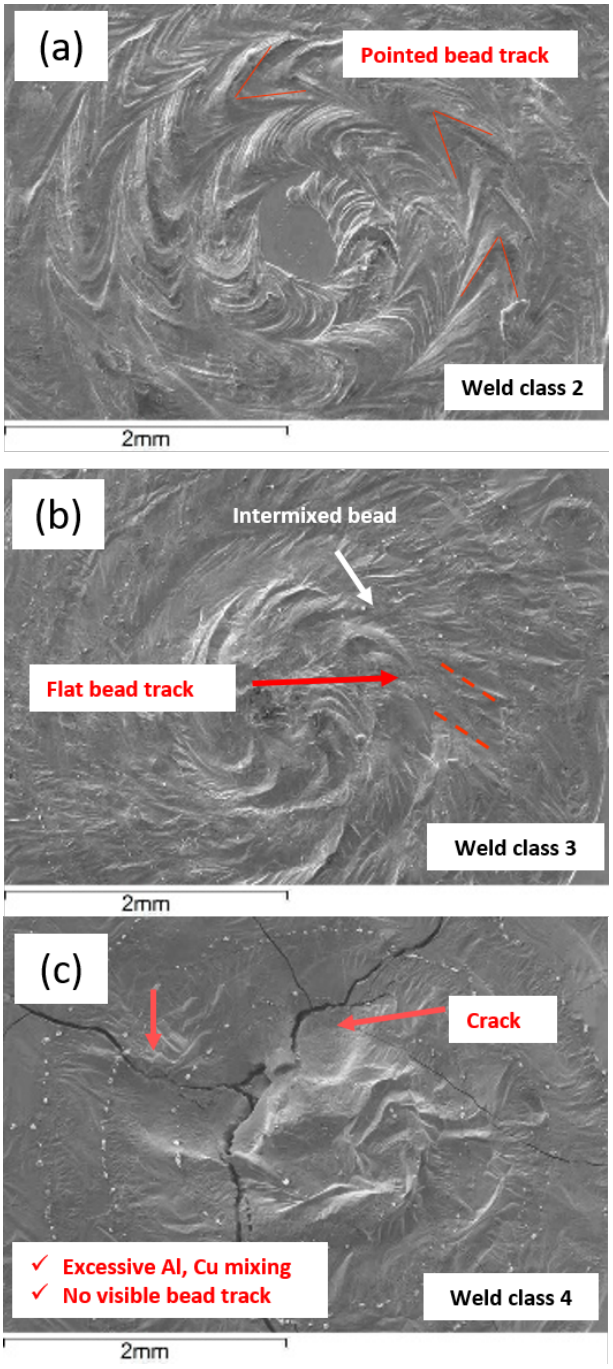

Figure 6.2: SEM images of the weld for class 2 (a), class 3 (b) and class 4 (c) showing bead features

6.1.2 Energy Dispersive X-ray Spectroscopy (EDS) analysis of the weld bead

The amount of Al/Cu diffused to the top of the weld seam is a result of the laser energy input which relates to the weld bead features on the top as shown in figure 6.3. Ten equally spaced points are taken for EDS analysis in the fusion zone along the diameter of the weld zone as shown in the plot (figure 6.3).

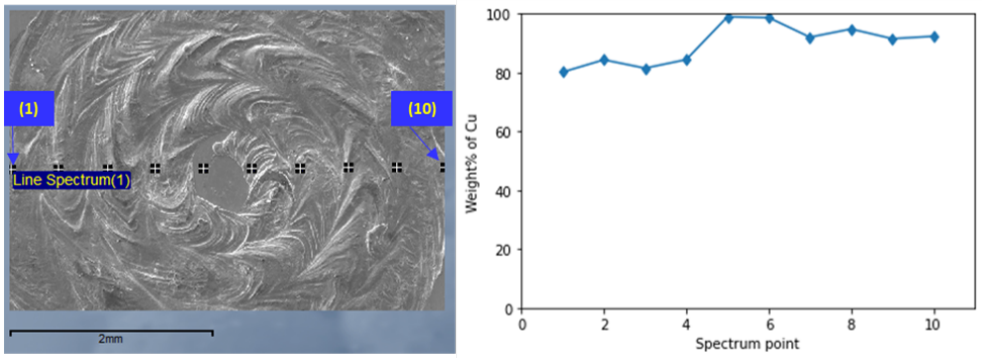

Figure 6.3: SEM image of weld class 2 and corresponding Energy Dispersive X-ray Spectroscopy (EDS) spectrum points showing the variation of Cu composition in weight %

From the EDS analysis, the amount of Cu present in the top of the weld seam is investigated. The weight % (wt%) of Cu in these points are measured and plotted in the figure 6.4. For class 1 weld the amount of available copper is in the range of 90-100 wt%. The amount of copper in classes 2, 3 decreases to a range of 80-100 %. In the class 4 weld seams, the amount of Cu % decreases significantly to 55-85 wt %. The key for a strong joint is to avoid decreasing the mixing percentage of Cu below 80 wt%. As the 70-80 wt% (red dashed line in figure 6.4) results in the formation of detrimental phases like Cu_2Al, Cu_3Al_2, Cu_4Al_3, and CuAl. The amount of Cu and Al intermixed on the top of the weld zone and the bead features are proportional. A simple optical image of the weld bead is enough to identify different weld classes as shown in figure 6.5.

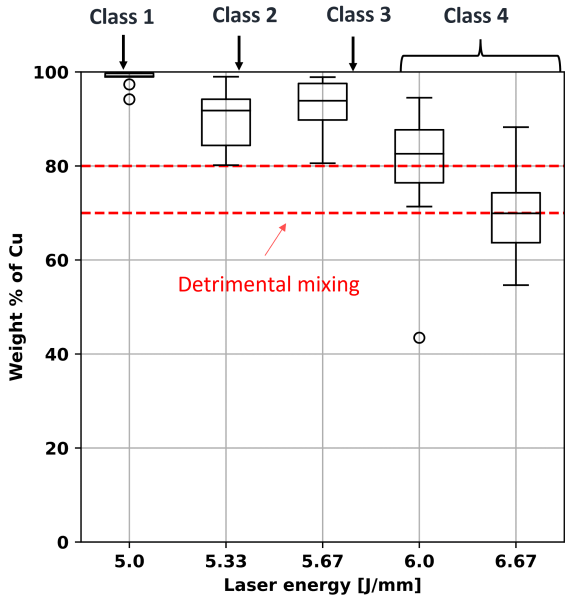

Figure 6.4: Box plot of EDS line spectrum point for different weld classes

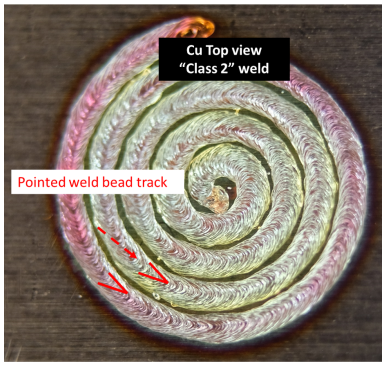

Figure 6.5: Optical image of the weld seam (Class 2) showing the weld bead track

Identification of the weld status from the high-resolution optical images automatically is required to qualify an "Acceptable" (class 2, class 3) or "Unacceptable" weld (class 0, class 1, class 4). The convolution neural network (CNN) model is better suited for this purpose as it can identify the weld types based on automatic feature extraction. The CNN architecture used to predict the weld type is explained in the section 6.4. This technique is non-destructive and relatively inexpensive which can be implemented in the existing production line soon after the welding process. Therefore, this is an alternative quality inspection/analysis technique for the production environment.

6.2 Preprocessing the weld images for the CNN model

High-resolution optical images of the weld seam are acquired by digital camera model number "Fujifilm X-Pro20" for non-destructive investigation. The raw images are prepossessed and fed as input to the convolution neural network (CNN) for the prediction of the weld class. The raw images from the digital camera of size 6000 × 3376 is resized to 960 × 540 and then the weld zone is cropped to a final height and width of 540 and 550 respectively. The height and width of the final image are selected to be 540 x 550 because there is a risk of losing the details of the weld zone if the image size is smaller. On the contrary, if the image height and width is higher than 540 x 550, then the size of the data is larger and training the convolution neural network is computational demanding. The conversion of the weld images for a convolutional neural network is performed with a computer vision package named "OpenCV" [9]. The preprocessed images (features) along with the weld type/label is shuffled for feeding into the CNN architecture. The corresponding shuffled images and the labels (i.e., weld classes 0, 1, 2, 3 and 4) are stored in NumPy array format [36] and saved as pickle file in Python programming language [104].

6.3 Analysis of optical weld images

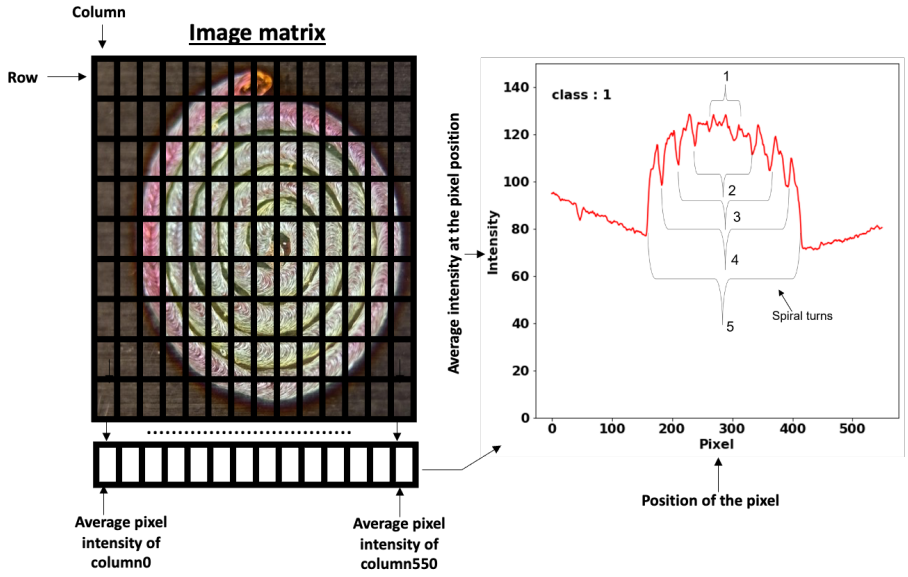

Figure 6.6: Example of the red pixel value (Intensity) distribution for the weld class 1

The analysis of weld images by splitting the RGB (Red, Green and Blue pixel of the image) components provide distinct features related to a particular weld class. As discussed before the addition

of Al content on the top of the weld seam results in different bead patterns from the SEM analysis. Similarly extracting bead patterns from the macro-images is a very rapid analysis. This also provides for a digital representation of the weld bead features. The plot in figure 6.6 shows the average red pixel intensity along the column of the image matrix (i.e., pixel position 0 px to 550 px) for weld class 1. The averaged red pixel intensity decreases at the beginning from 0 until 200 pixels. After 200 px the average intensity increases to 115 then there is a decrease in the intensity to a value of 100. The average intensity increases and decreases until 400 px. Further after 400 px the intensity increases until 550 px. The fluctuation of the average intensity of the pixel i.e., between 200 - 400 px is the weld zone and the other regions in the beginning and end are the Cu base material. The regions marked as 1, 2, 3, 4 and 5 in the weld zone are the number of turns in the spiral. The extraction of the RGB components of the image provides a digital representation of the weld image. With this approach, information related to individual turns of the spiral, the weld dimensions and the pixel intensities can be extracted.

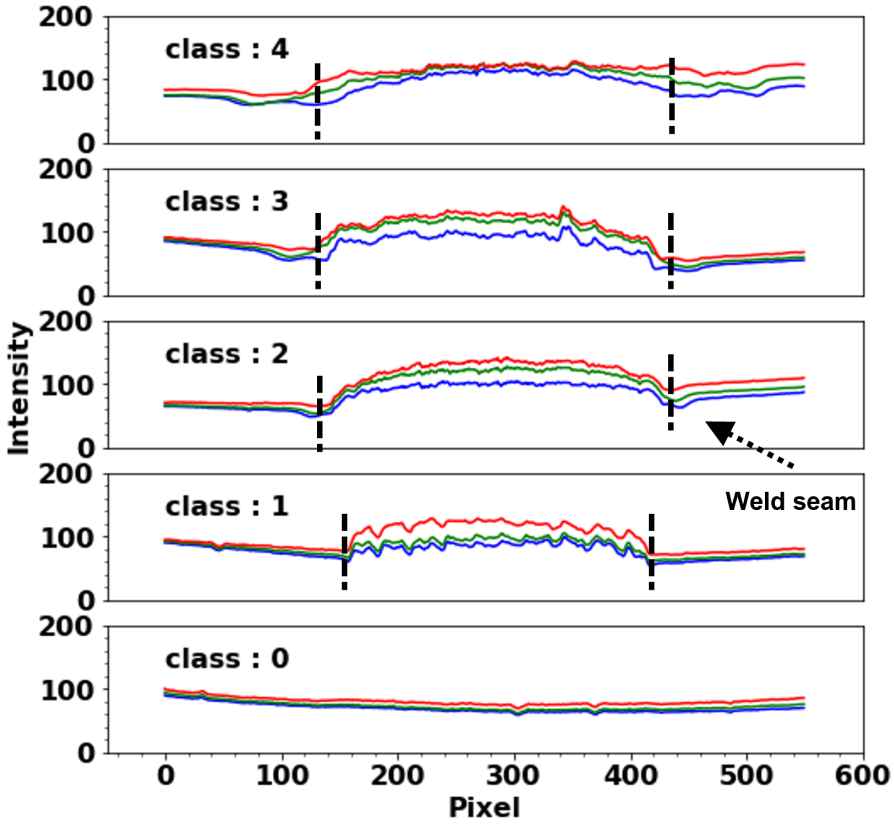

Figure 6.7: Variation of the red, green and blue pixel intensities for different weld classes (class 1, class 2, class 3 and class 4)

The plot in figure 6.7 shows the RGB component of the weld image for different weld classes

from 0 to 4. The mean intensities of the pixels are shown in the Y-axis and the pixel position is shown in the X-axis. For class 0 weld the pixel intensity is a flat line with no fluctuations in the intensity for the change in pixel position. For class 0 weld there is no weld and there is no spiral appearance in the weld seam, hence no information related to the spiral turn is present. For class 1 weld there is a fluctuation of the pixel intensity at the weld location for all the channels such as red, green and blue. The red channel has a higher intensity compared to the blue and green pixels. For class 2 weld the fluctuation is reduced and the weld region is increased in comparison to the class 1 weld. The intensity of the green pixel is increased in comparison to the class 1 weld. The intensity of the red pixel and the green pixel are now nearly the same as class 1 weld images. For class 3 images, the weld region is slightly increased in comparison to the class 2 weld. The value of the red and the green pixel is very close to each other as in class 2 weld. However, the value of the blue pixel is the lowest in comparison to red and green pixel intensity.

In class 4, the pixel length representing the weld zone is increased in comparison to class 3 weld. In contrast to other weld classes, the intensity of the red, blue and green channels in class 4 is nearly the same especially at the centre of the weld seam (pixel location of about 200-250 px). At the outer edges, the value of the red pixel is the highest followed by the green pixel and the blue pixel. Therefore the individual RGB pixel values of the images give more information related to the weld seam status, which can be modelled.

6.4 Convolutional neural network model

As shown in the previous section (section 6.3) that weld images in each class can be distinguished based on the values of red, green and blue pixels. However, the relation of the pixel values for different weld classes and the spatial dimension (width and height of the image) is complex. Therefore a model to automatically extract the relevant features of the weld images for different classes is required. A convolution neural network (CNN) model is designed for this purpose to predict the weld status from high-resolution optical images. The convolutional neural network model for investigation consists of the following layers such as input layer, convolutional layer, pooling layer, flatten layer, dense layer, output layer. In this thesis model architectures with different numbers of convolution and pooling layers were investigated, i.e, the number of conventional and pooling layers were changed. The model with two convolution and pooling layers is N=2 and the model with four convolutions and pooling layers is N=4. The model with six convolutions and pooling layers is N=6. Finally, the model with eight convolutions and pooling layer is N=8. The convolutional layer is followed by the pooling layer in all the architecture used. After the final convolutional and pooling layers (final layer depends on the number of pooling and convolutional layers, i.e., N=2, 4, 6 or 8), the output

is fed into a flatten layer and a dense layer (Fully connected). The final output layer predicts the 5 different classes, i.e., class 0, class 1, class 2, class 3, and class 4. The number of filters for all the model architectures (N=2, 4, 6 or 8) is selected to be 64. An example of the model architecture created with four convolution and pooling layers is shown in figure 6.8. As the number of convolution and pooling layers increases, the depth of the model increases.

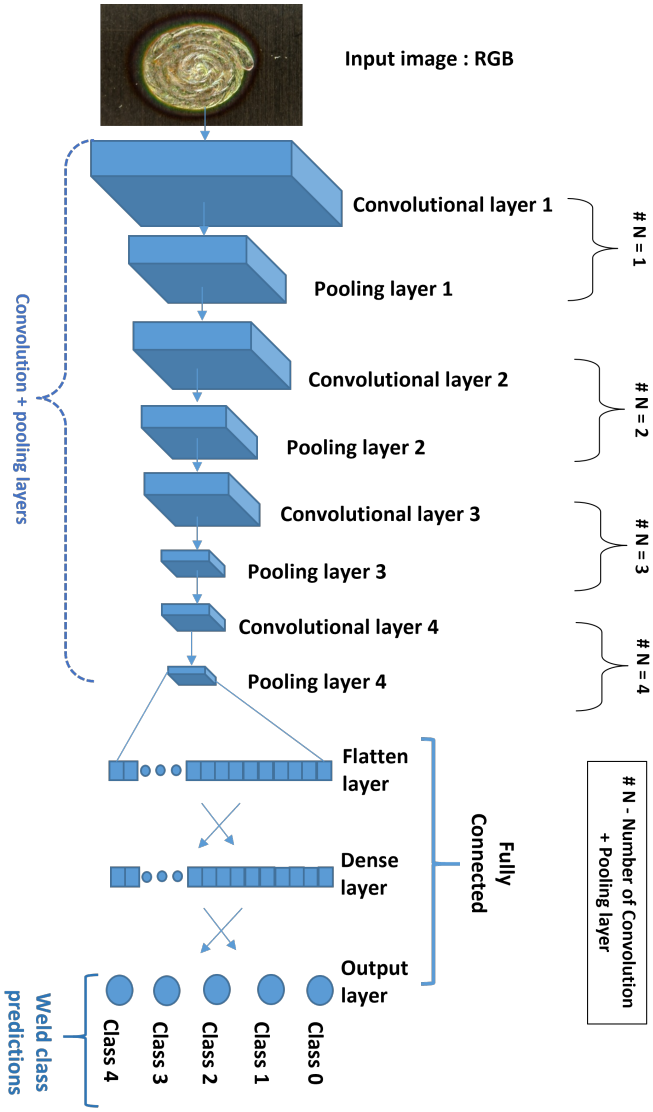

Figure 6.8: Schematic of the CNN architecture with four convolutional and pooling layers (N=4)

The flow of the input image into the model is explained with the model architecture consisting of four convolutional and pooling layers (N=4) as shown in the figure 6.8.

In the convolutional layer the input image of size 540 (width) x 550 (height) x 3 (RGB) is

convoluted (multiplied) with a kernel or a filter of size 3 x 3 x 3. The kernel is basically a matrix that slides across the input image and multiplies with the input. In this case 64 different filters of size 3x3 is selected and the convolution layer outputs a matrix of dimension 540 x 550 x 64 (540 (width) x 550 (height) x 64 (number of filter)) as shown in figure 6.9.

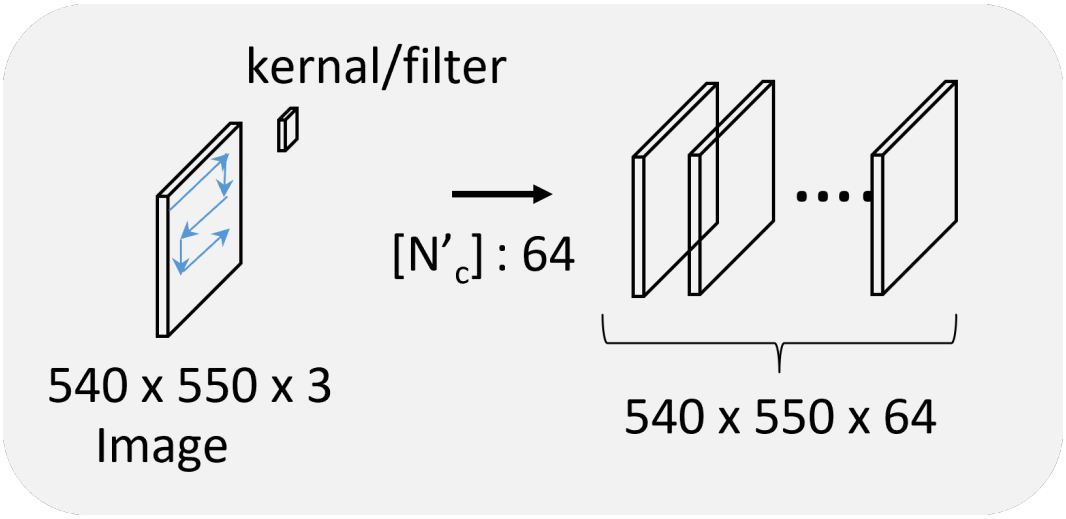

Figure 6.9: Schematic of the convolution operation applied on the input image of size 540 x 550 x 3

The output of the convolution layer is fed to the pooling layer (max pooling) where the maximum value for each patch (2 x 2) of the feature map is calculated. As a consequence of the max pooling operation downsampled output or feature map is obtained. After the max pooling operation, the input matrix of size 540 x 550 x 64 is reduced to 270 x 275 x 64.

The schematic of the model with 4 convolution layers (N=4) each followed by a max-pooling layer is shown in figure 6.8. At the end of the first convolution and max-pooling block (N=1), the input of size 540 x 550 x 64 is reduced to 270 x 275 x 64. After the second convolution and pooling layer (N=2), the input size is further reduced to 135 x 137 x 64. The output size is further decreased to 67 x 68 x 64 after the third convolution and pooling operation (N=3). After the final convolution and max-pooling layer (N=4), the output size of the feature map is 33 x 34 x 64. The output of the feature map (N=4) is flattened to 4595776 (33 x 34 x 64) in the flatten layer and is fed to the dense layer of size 64 which is fully connected. The output of the previous dense layer is connected to a final dense layer of size 5. The size of the final dense layer is selected to be five in order to identify five different weld classes. Each of the convoutional layer is activated with rectified linear unit activation function ("ReLU" in keras). The ReLU function is defined as the positive part of its argument. $f(x) = x^+ = max(0, x)$

The final dense layer is activated with a softmax activation function to normalize the output (

prediction of weld class) of the network to a probability distribution over predicted output classes. It applies the standard exponential function to each element z_i of the input vector z and normalizes these values by dividing by the sum of all these exponentials; this normalization ensures that the sum of the components of the output vector is 1. The standard (unit) softmax function $\sigma : \mathbb{R}^K \rightarrow [0,1]^K$ is defined for $i = 1, ..., K$ (K - number of classes in the multi-class classifier) and $z = (z_1, ...z_k) \varepsilon \mathbb{R}^K$ by the formula:

$$\sigma(z)_i = \frac{e^{z_i}}{\Sigma_{j=1}^{K} e^{z_j}} \tag{6.1}$$

The convolutional network model is compiled with "Adam" optimizer and the loss function used is "sparse categorical crossentropy" [2, 17]. The "sparse categorical crossentropy" loss function is used because our objective is to predict different weld classes or categories. The network is trained for 25 epochs with (total number of samples = 184) 70% data used for training and 30% for validation. An epoch (or iteration) is a term used to indicate the number of passes of the entire training dataset the machine learning algorithm has completed. For model training, the learning rates of 0.01, 0.0001 and 0.00001 were investigated for different model architectures, i.e., model with 2, 4, 6 and 8 convolutional and pooling layers.

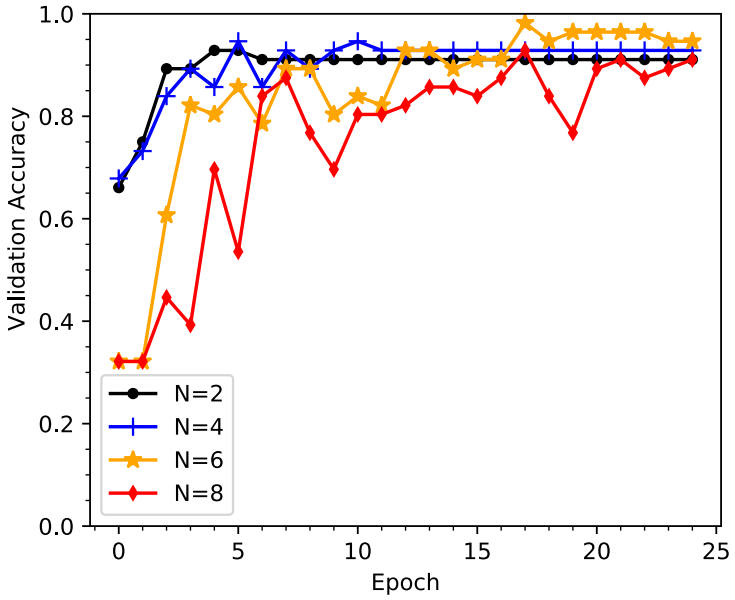

Figure 6.10: The validation accuracy of the model architectures (N=2, 4, 6 and 8) with learning rate of 0.0001 for different epoch

The result of the models (N=2, 4, 6 and 8) trained with a learning rate of 0.0001 is shown in

figure 6.10. The number of training iterations (epoch) is shown on X-axis and the validation accuracy is shown on Y-axis. The plot in figure 6.10 shows the validation accuracy of the model after each training step or epoch. The validation accuracy is calculated on the 30 % data (validation data) which is not used for training but for validation only. After training for 25 iterations (epoch) with a learning rate of 0.0001, the model architecture with four convolution and pooling layers (N=4) achieved 100 % training accuracy (i.e., with training data) and 92% accuracy (validation accuracy) with the validation data. Further increasing the convolution and pooling layers to six (N=6), the validation accuracy increased slightly to a value of about 96%. But increasing the convolution and pooling layers further to eight (N=8) did not improve the validation accuracy.

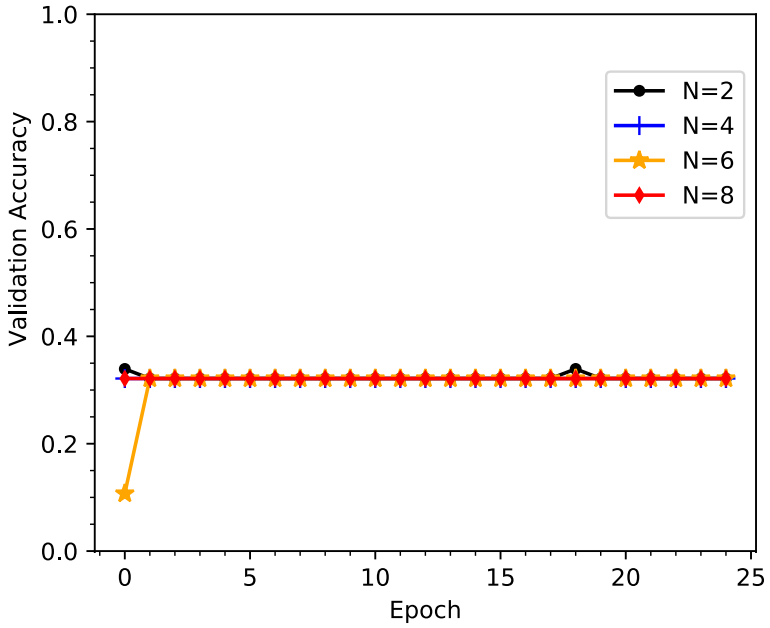

Figure 6.11: The validation accuracy of the model architectures (N=2, 4, 6 and 8) with learning rate of 0.01 for different epoch

It is also very important to select the right learning rate for training the model. The plot in figure 6.11 shows the validation accuracy of different model architectures (N=2, 4, 6 and 8) for a learning rate of 0.01 and for different epochs. A high learning rate value of 0.01 resulted in very low values of validation accuracy of about 40 % for all the model architectures of 2, 4, 6 and 8 convolutional and pooling layers.

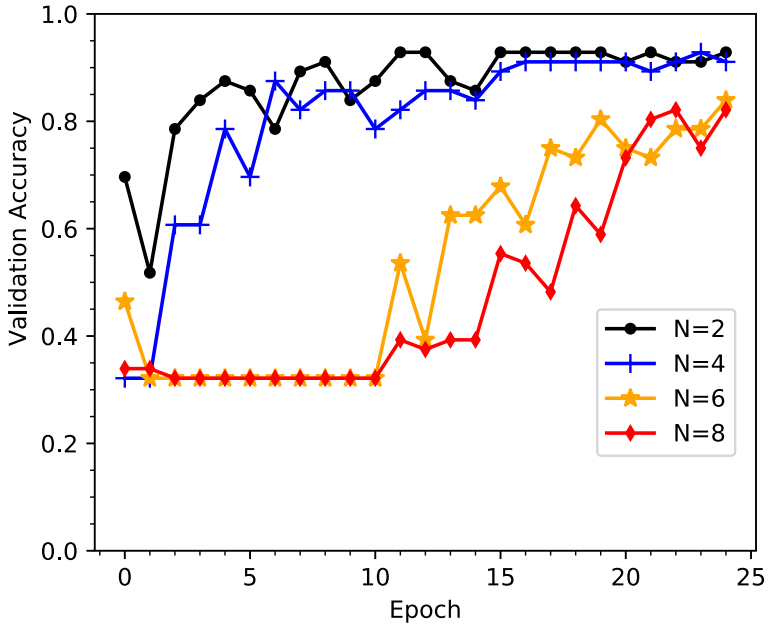

Figure 6.12: The validation accuracy of the model architectures (N=2, 4, 6 and 8) with learning rate of 0.00001 for different epoch

However decreasing the learning rate of the model to 0.00001, the model architecture with a small number of convolutional and pooling layers i.e, N=4, N=2 performed better than the architectures with six and eight layers as shown in the plot figure 6.12. The model architecture with six and eight convolutional and pooling layers achieved a validation accuracy of about 80% which is very less in comparison to the validation accuracy of the model architectures with 2 and 4 layers (about 92%).

From the investigations, the model architecture with six convolutional and pooling layers achieved maximum validation accuracy of about 96 %. The learning rate of 0.001 was found to achieve high accuracy with most of the model architectures investigated i.e., with different numbers of convolution and pooling layers (N=2, 4, 6 and 8).

6.5 Visualization of the features for different weld classes

In order to show that the model prediction is not random and to understand the output of the convolution and pooling layers, the model architecture with six convolution and pooling layers (N=6) is selected for visualization of features. The meaning of visualization here refers to what different filters extract in an image or the features extracted in the selected layer for a particular weld image. Features refer to any shapes or patterns the convolutional neural network extracts from a given image.

The output response after the sixth convolution and pooling layer (i.e., the final convolutional

and pooling layer of N=6) for the weld image of class 4 is shown in figure 6.13. The figure shows the response of all the sixty-four filters (since 64 filters were used) in subfigures plotted at the end of the sixth convolution and pooling layer in figure 6.13. The plotted subfigure image is 8 x 8 consisting of 64 images in total. The first subfigure on the top is the response of the first filter to the class 4 image. Similarly, the last filter is the response of the sixty-fourth filter to the class 4 image. It can be seen that each filter detects certain features of the welded image such as a bright outer circle and dark appearance at the centre as shown in the sub-images in figure 6.13.

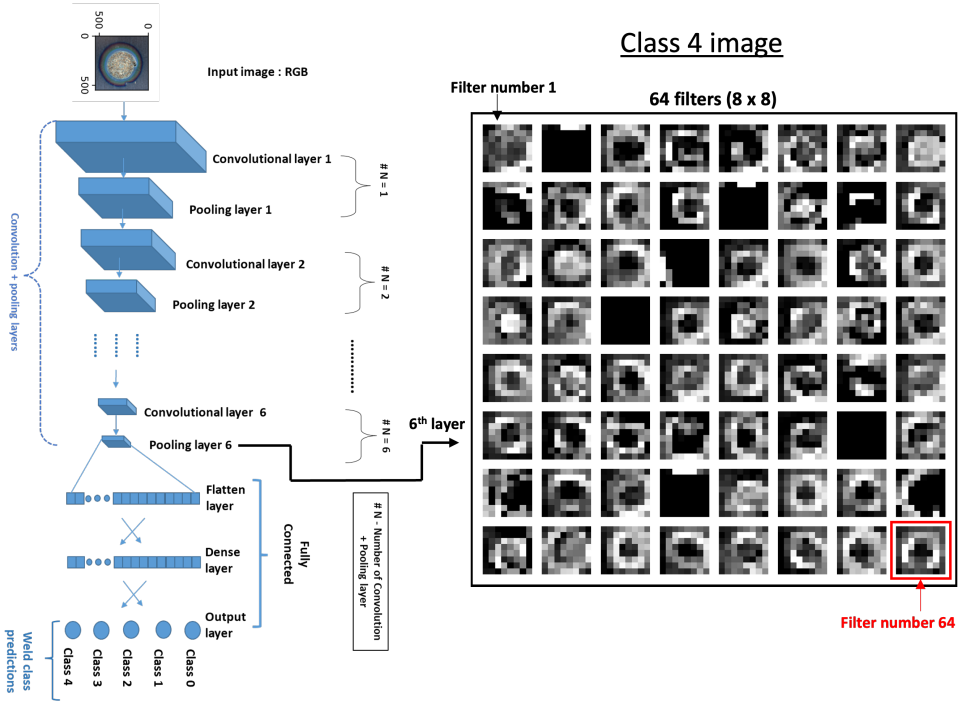

Figure 6.13: Visualization of 64 filters after the final convolutional and pooling layer of model architecture N=6

For detailed investigation, the last filter (sixty-fourth filter) is selected and the response of the filter for different weld images such a class 0, class 1, class 2, class 3 and class 4 is shown in figure 6.14. The class number is shown on the top of each image. It can be seen that the selected filter (filter number 64) detects different features depending on the weld class. For class 0 weld, the model did not detect any interesting feature, as the image was "No weld" condition. For class 2 weld, the model detects a bright circular spot. The brightness in the centre decreases for class 3 and class 4 images. For the class 4 image, the model detects a torus shape (doughnut-like appearance) with a dark spot in the centre and a bright outer circle.

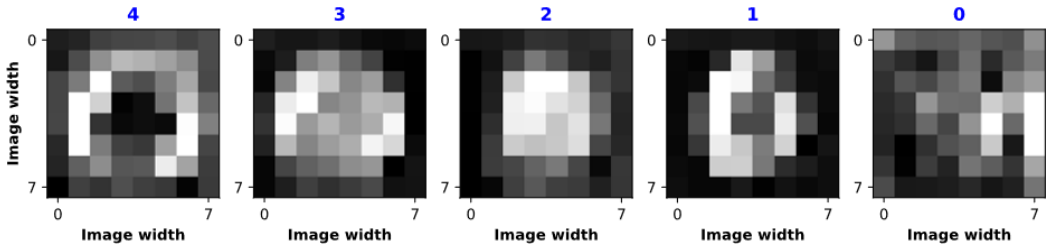

Figure 6.14: Example images of the last filter (filter number 64) detecting different features for weld classes such as 0, 1, 2, 3 and 4

In conclusion, the proposed model extracts the relevant features present in the welds as shown in the images of figure 6.14 to predict the weld classes.

The confusion matrix of the model prediction on the validation data (55 samples) is shown in figure 6.15. The columns in the matrix represent the actual class of the welds and the rows in the matrix shows the prediction of the weld classes by the model (model prediction in y-axis). The diagonal elements and the non-diagonal elements in the matrix show the correct and incorrect prediction by the model for different weld classes respectively.

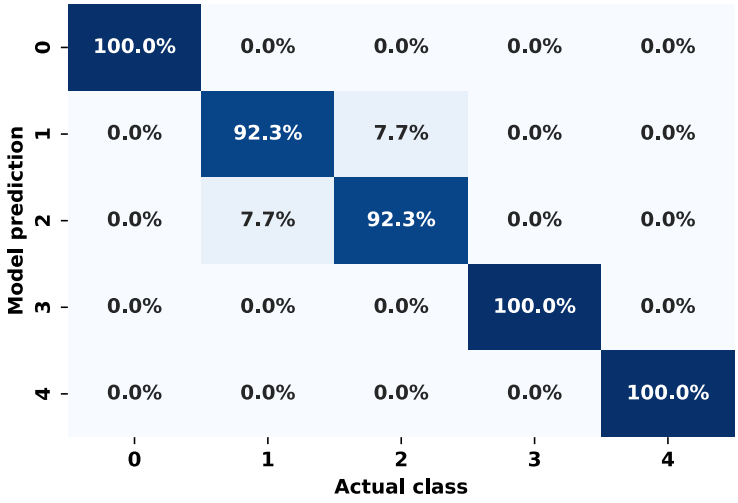

Figure 6.15: Confusion matrix of the CNN model on the validation data

As shown in the confusion matrix, the CNN model performs well with weld class 0, weld class 3 and weld class 4. However, the model has difficulty in discriminating the welds of class 1 and class 2. The correct prediction accuracy for the class 1 and class 2 weld is 92.3% (incorrect prediction is 7.7%).

6.6 Summary

In summary, the high-resolution weld images acquired by the camera were analysed by assessing the red, green and blue components of the images. It was shown that distinct patterns exist for the red, green and blue pixel intensity for different classes. From the SEM-EDS analysis on the top of the weld bead, the aluminium content increased and copper content decreased for increasing the laser energy per unit length or for increasing class number. Therefore it was shown that each weld class appears distinct based on the RGB pixel values, which are influenced by the Al and Cu content melted during the welding process. A convolutional neural network was designed to model the weld images and automatically extract relevant features to predict the weld classes. The proposed model achieved a validation accuracy greater than 92% on the new unseen images.

- The high-resolution weld images acquired by the camera were used for training a convolutional neural network to predict different weld classes. A non-destructive identification of different weld classes were shown.

Chapter 7

Analysis of optical emission during Cu-Al welding

In laser welding of Cu and Al, there is a need to evaluate the weld status non-destructively in real-time. However, the important question is, how to detect a good or bad weld rapidly and cost-efficiently? Welding of Cu and Al metals with a laser beam is accompanied by the emission of optical radiation. The optical radiation emitted during the welding process consists of plasma plumes or gas plasma of the molten metals that are being welded.
The idea is to use the information from the plume to understand the weld status. However, high-speed data acquisition of the plume is required as the welding process is very fast, in the order of 300 mm/s. Therefore, commercial spectroscopes are not useful directly in the context to access weld quality. However, the spectroscopic analysis provides critical information about the characteristics peaks of the welded materials and aids in the preliminary setup. Based on the literature work in the field of process monitoring, the identified research gaps are:

1. Most of the work in monitoring the Cu and Al welds were performed using a spectrometer with a sampling frequency of 1000 Hz and it was suggested that the low sampling frequency was not sufficient to capture the dynamics of the welding process.

2. Al peak at 396 nm is well detected during laser ablation and laser welding process. But there is limited investigation regarding its correlation to the process parameters, especially for Cu-Al dissimilar welding.

3. There is limited work regarding the understanding of the weld signals to the melt status or weld classes, which is of most interest from the application point of view.

Since the traditional analysis methods like tensile shear test and cross-sectional analysis of the weld seam is time-consuming and destructive, a technique for qualification/analysis of weld in-line is of prime importance in production. In this chapter, the above-mentioned research gaps are addressed. As shown in the results section of chapter 5, typical welding speeds for Cu and Al are in the range of 100 mm/s to 600 mm/s. Depending on the interaction of the laser radiation, with the Cu and Al metals, distinct vapour plume signals are generated. In this chapter with the distinct weld signal in the time domain, different weld status like insufficient weld, good weld, and excessive weld status is expected to be identified in real-time.

7.1 The spectrum of Cu-Al welding

The plot of the emitted signal during laser welding of Cu-Al is shown in figure 7.1. The horizontal axis shows the wavelength from 200 nm to 1100 nm and the vertical axis shows the intensity of the signal.

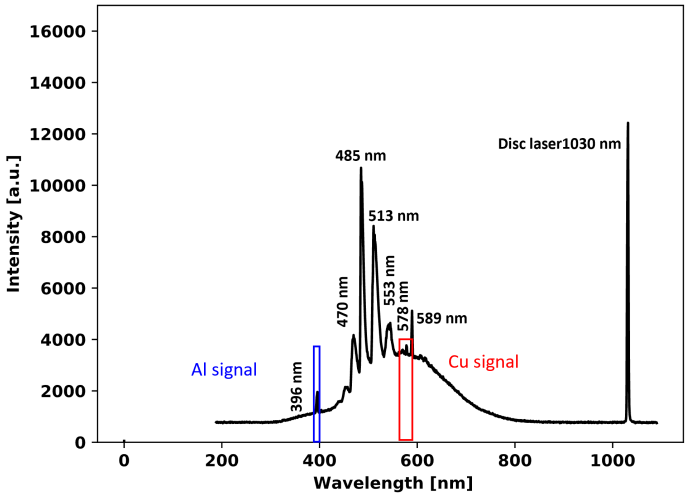

Figure 7.1: The emission spectrum of welding Cu-Al with disk laser, showing Al melting peak at 396 nm and Cu peak at 578 nm

The characteristic Al peak is at 396 nm. Peaks at 440, 454, 467, 487, 514, 544, and 566 nm are the reaction of Al with O forming Al_2O_3. Other peaks at 589 nm, 765 nm and 769 nm are explained by the Na and K, respectively based on the NIST (National Institute of Standards and Technology, United States) database. The peaks at 578 nm and 1030 nm are corresponding to the Cu metal and the reflection of the laser light (disk laser wavelength), respectively [61] [86] [18].

In this research, the wavelength of 396 nm is chosen as an indication of welding Al since it is the

characteristic peak corresponding to Al(I) spectral line. So the research work focuses on the specific peak of Al at 396 nm to qualify that sufficient Al is melted for a weld sample. For monitoring Cu melting, the wavelength of 578 nm is selected. The spectroscope provides information about the wavelength and intensity at the sampling rate of 100 Hz, which is too slow for implementation in laser welding.

7.2 Description of Cu and Al signals acquired by photodiode during laser welding

The schematic of the process monitoring used in this thesis is shown in figure 7.2.

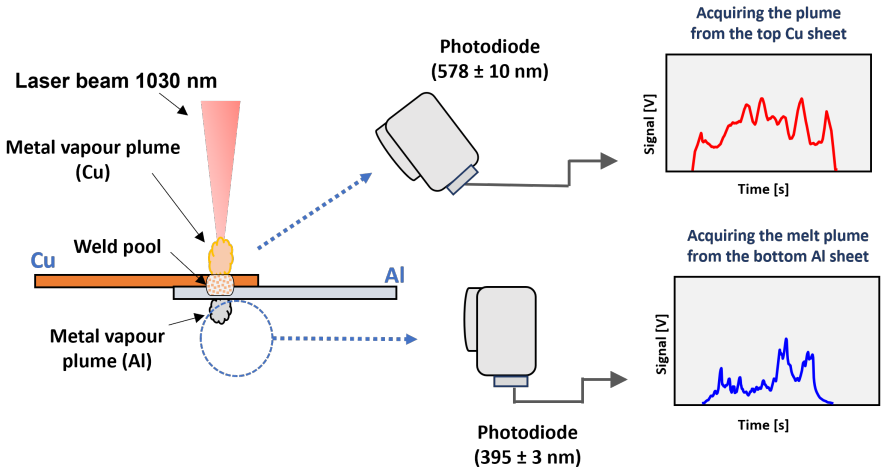

Figure 7.2: Sketch of the monitoring process, employing photodiodes collecting the process emission at the central wavelength of 395 nm

The choice of using the off-axial position is mainly due to the inability of detecting the characteristic spectrum in the co-axial position, which is blocked by the coating on the optic of the scanner. Using the photodiode in the off-axial position allowed to select two different locations as shown in the schematic (figure 7.2). A band-pass filter of 578 (578 +/- 10 nm) is fixed to the photodiode which is placed on the top side of the overlapped sample (Cu top) as shown in figure 7.2. This signal is called "Cu-signal" and is plotted with red colour throughout this chapter. A band-pass filter of 395 nm (395 +/- 3 nm) is installed to the photodiode, which is placed under the Al sheet, to collect the process light (weld plume) from the bottom side of the overlapped sample representing the melting of Al metal from the bottom of Al sheet. This signal is called as Al signal and is plotted in blue colour throughout this chapter. The collected emission light detected using the photodiode is referred to as a welding signal or signal in this chapter. The welding signal is acquired at the

sampling frequency of 100 kHz, which is sufficient to capture the melting activity during the welding process.

Two welding trajectories are selected to show the potential application. First, a simple line welding is also chosen with a welding length of 5 mm. Secondly, the spiral welding strategy of diameter 5 mm is chosen so that the field of view of the photodiode is always in the welding zone.

7.3 Welding signals of the line trajectory

The results of welding signals and their corresponding top view images of the weld are shown in the figure 7.3. The top view images of the Cu-Al weld shown in figure 7.3 were taken after the welding process.

The Cu and Al sheets are welded with the line trajectory where the laser beam moves for 5 mm from the start point to the endpoint. The laser welding direction is marked by the white arrow on the top view images of the Cu-Al weld as shown in the figure 7.3. For welding with line trajectory, the laser power was fixed to 2000 W and the laser velocity was changed from 100 mm/s to 300 mm/s. The laser power of 2000 W and velocity of 100 mm/s (20 J/mm) resulted in excessive Cu and Al melted in the fusion zone as shown in the weld image (figure 7.3, V=100 mm/s). At the end of the weld seam, there is excessive melting of Al which is due to the heat accumulation at the end of the welding process. The Cu signal value in the beginning for about 2 ms is 1.9 V. After 2 ms the Cu signal value drops to 0.5 V and fluctuates for 50 ms i.e., until the end of the weld and further drops to 0 V. Conversely, the Al welding signal obtained from the bottom of Al sheet has a low value of the signal in the beginning for about 2 ms. After 2 ms, the Al signal increases to the value of about 0.5 V and further fluctuates until the end of the weld. The Cu and Al signal fluctuation represent the melting activity during the welding process. There is an increase in Al signal value (about 1 V) at the time interval of 35 - 50 ms marked by the green circle (figure 7.3, V=100 mm/s). This increase in Al signal value for 35 - 50 ms corresponds to the excessive melting of Al which is also observed in the corresponding weld image (excessive melting marked by the green circle).

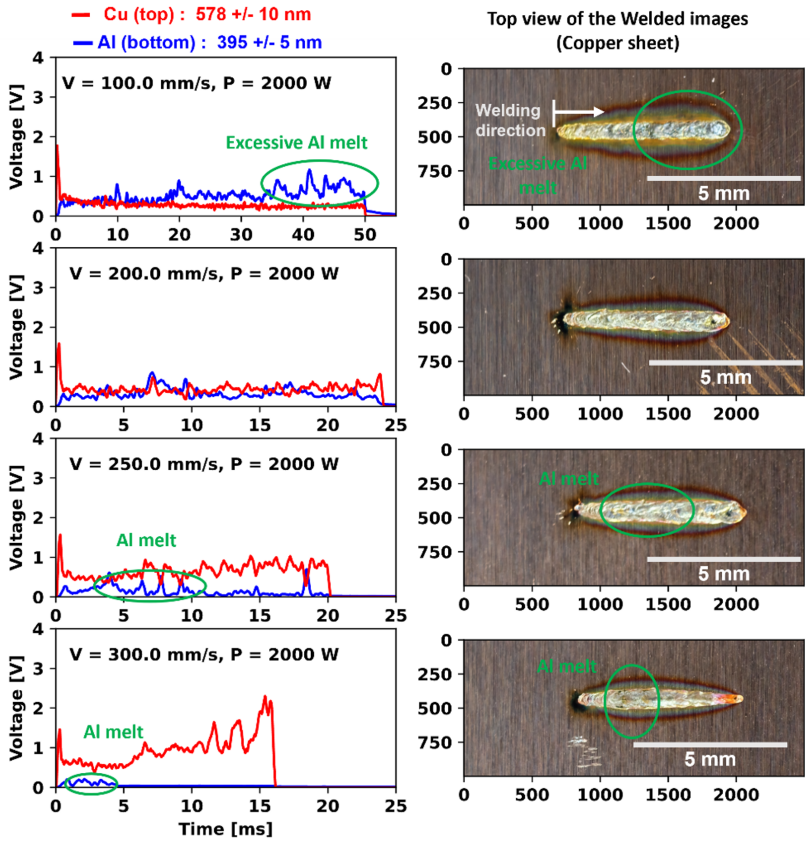

Figure 7.3: Cu and Al signals and corresponding images of the weld seam for the laser power of 2000 W and velocities of 100 mm/s, 200 mm/s, 250 mm/s and 300 mm/s

Increasing the laser speed to 200 mm/s, the Cu signal was similar to 100 mm/s, with the increase in the signal value at the beginning of the welding and the signal value decreasing until the end of the weld. But the value of the Cu signal is slightly higher compared to 100 mm/s. The value of the Al signal for 200 mm/s is slightly lower in comparison to 100 mm/s. However, no excessive Al melting at the end of the weld was observed in the weld image and the Al signal value.
Increasing the laser velocity further to 250 mm/s, the value of the Cu signal is higher in comparison to both 200 mm/s and 100 mm/s. On the other hand, the value of the Al signal is lower in comparison to the former laser velocities of 200 mm/s and 100 mm/s.

For 250 mm/s, the Al signal value between 5 ms to 10 ms was higher in comparison to other time intervals, representing a higher Al meting. Similarly, around the same position in the weld image excessive melting activity was observed. Further increasing the welding speed to 300 mm/s, the Cu

signal value was significantly higher than the lower welding speeds of 250 mm/s, 200 mm/s and 100 mm/s. Contradicting to the Cu signal, very little Al signal was obtained in comparison to the lower welding speeds. The signal value of Al particularly increased between 1 ms - 5 ms. However, for the same time interval of 1 ms - 5 ms, the value of the Cu signal was decreased. From the investigation of Cu and Al signals for different velocities, the value of the Cu signal decreases as the velocity decreases especially from 250 mm/s to 200 mm/s and 100 mm/s. A decrease in the laser velocity leads to increased laser energy per unit length ($E = P/V$). For the increased laser energy per unit length, the Al sheet is penetrated as indicated by the Al signal.

Increasing the applied laser energy per unit length, the laser is penetrated deep into the Cu-Al bottom sheets, which leads to increased melting and mixing of Al and Cu metals. This results in less plasma plume formed on the top sheet, consequently, a lower Cu signal is obtained. It is interpreted from the Al and Cu signals for different laser velocity that the high Cu signal values represents less Al melting and conversely high Al signal values indicate higher Al melting.

7.3.1 Welding signal and the longitudinal cross-sectional view of the line welds

The figure 7.4 shows the Cu signal at 578 nm from the top and Al signal at 396 nm from the bottom sheet and the corresponding longitudinal section of the weld seam in the microscopic image. The sample was welded with laser power and velocity of 2000 W and 400 mm/s respectively. As shown in the longitudinal cross-section, the welding direction is from the left to the right side as marked by the red arrow. It can be seen in the longitudinal cross-sectional image that the melting of Cu and Al varies along the direction of the weld length. In locations 1, 2 and 3, the Al has melted more during the welding process and the fusion zone is formed as a result of Cu and Al intermixing. For the exact locations of Al melts at locations 1, 2,and 3 in the longitudinal cross-section image, there is a decrease in the Cu signal value as shown in the plot (figure 7.4). It can be seen from the cross-section image that at the beginning of location 1 there is a significant Al melt of about 0.25 mm. Similarly, for the Al signal plot, a peak value in the Al signal value is obtained exactly at the beginning of location 1.

However, on the other hand, where the Al was not melted as seen in the longitudinal cross-sectional image(figure 7.4), the Cu signal value was higher in comparison to the locations where the Al was melted. In locations 2 and 3 the Al melt is limited to the interface, as a result this can be identified from the drop of Cu signal value. The Al signal from the bottom sheet did not give any information, as the Al melting was limited to the interface.

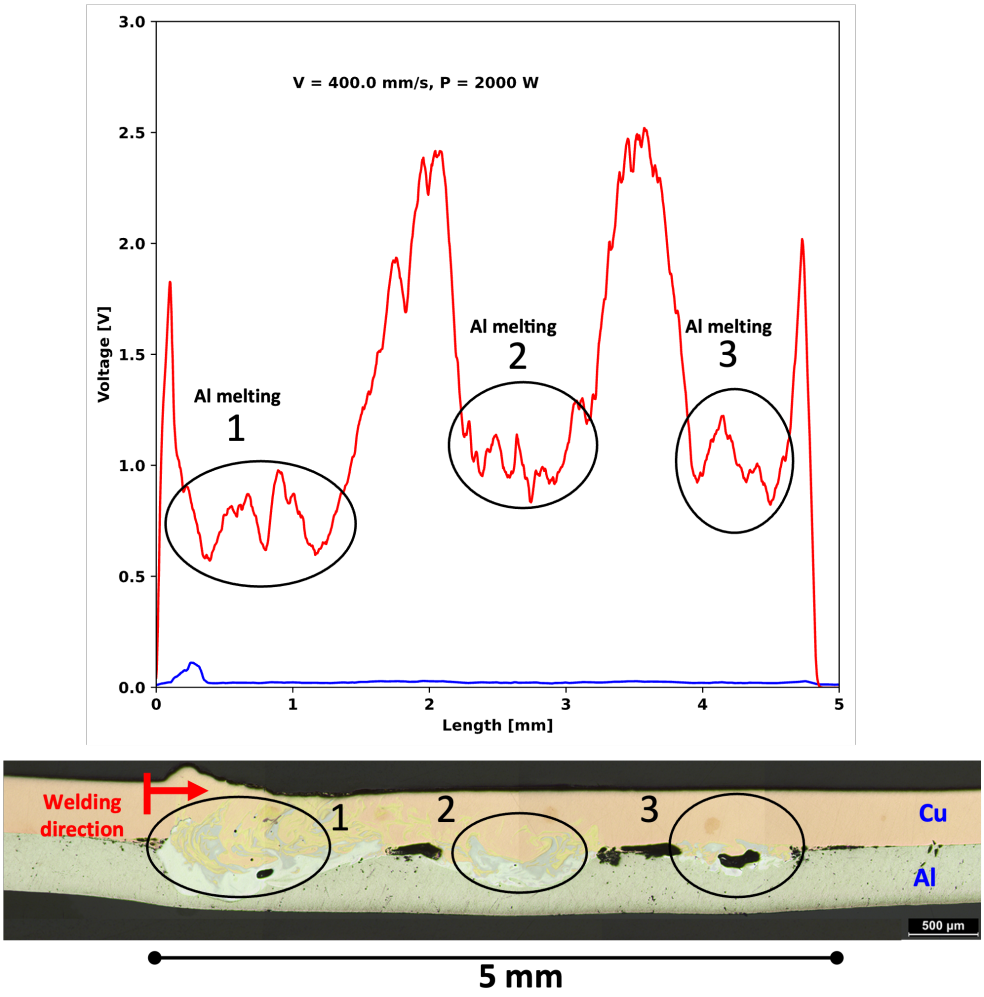

Figure 7.4: The plot of Cu, Al signals and its corresponding longitudinal cross-sectional view for the laser power of 2000 W and velocity of 400 mm/s

The Cu and Al signals and their corresponding longitudinal cross-section welded with laser power of 2000 W and velocity of 100 mm/s are shown in figure 7.5. From the longitudinal cross-sectional images it can be seen that the Cu and Al melted in the fusion zone is significantly higher for 100 mm/s (figure 7.5) in comparison to that of the longitudinal cross-sections of the welded sample at 400 mm/s (figure 7.4). The laser irradiation resulted in full penetration and complete melting of Al sheet thickness. Higher mixing of Cu and Al happened in the fusion zone. Because of the increased melting in the fusion zone, large detrimental phases and cracks are formed. There is an excessive melting of Cu and Al (location 1 in figure 7.5, marked with a black circle on the longitudinal cross-sectional image) at the end of the weld in comparison to the beginning of the weld due to heat accumulation at the end of the weld.

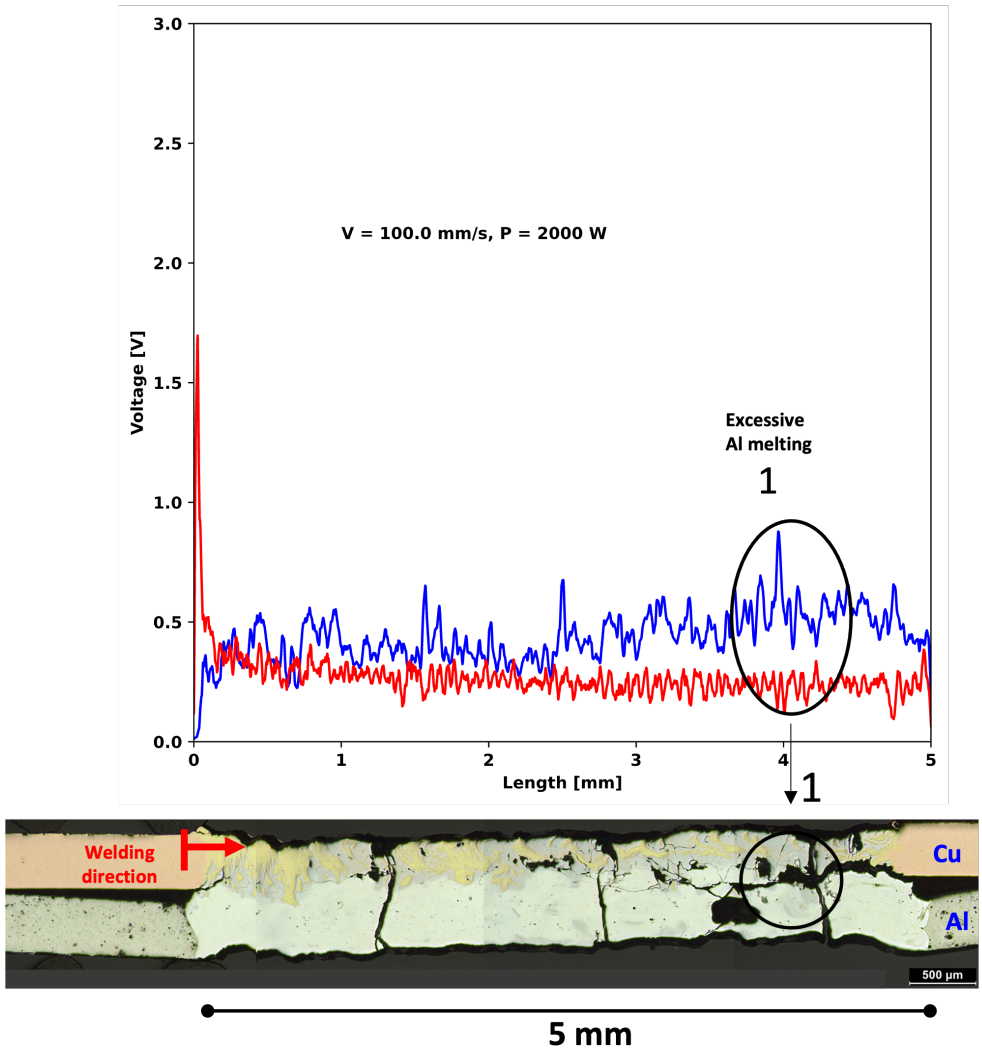

Figure 7.5: The plot of Cu, Al signal and its corresponding longitudinal cross-sectional view for the laser power of 2000 W and velocity of 100 mm/s.

Similarly, the excessive weld at the end can be identified from the increasing Al signal at 4 mm and conversely decreasing Cu signal value. The laser irradiation in this condition resulted in a deeper penetration into the Al sheet and this is the reason for the higher Al signal from the bottom of the sheet in comparison to the Cu signal. As shown in the figure 7.5 at location 1, the Al signal from the bottom sheet is a very good representation of excessive weld condition.

Therefore, it can be concluded from the longitudinal cross-section analysis that the decrease in the Cu signal can be used to represent the Al melting and is an indication that the laser melting is deeper in the Cu sheet. On the contrary, for an increase in the Al signal from the bottom sheet represents an increase in Al melting and the laser melting is deeper in the Al sheet.

7.4 Welding signals of the spiral trajectory

7.4.1 Effect of welding signal for different laser power

The photodiode signal during welding of Cu-Al with spiral laser trajectory for different laser powers and constant velocity of 300 mm/s is shown in subplots in figure 7.6 and figure 7.7.

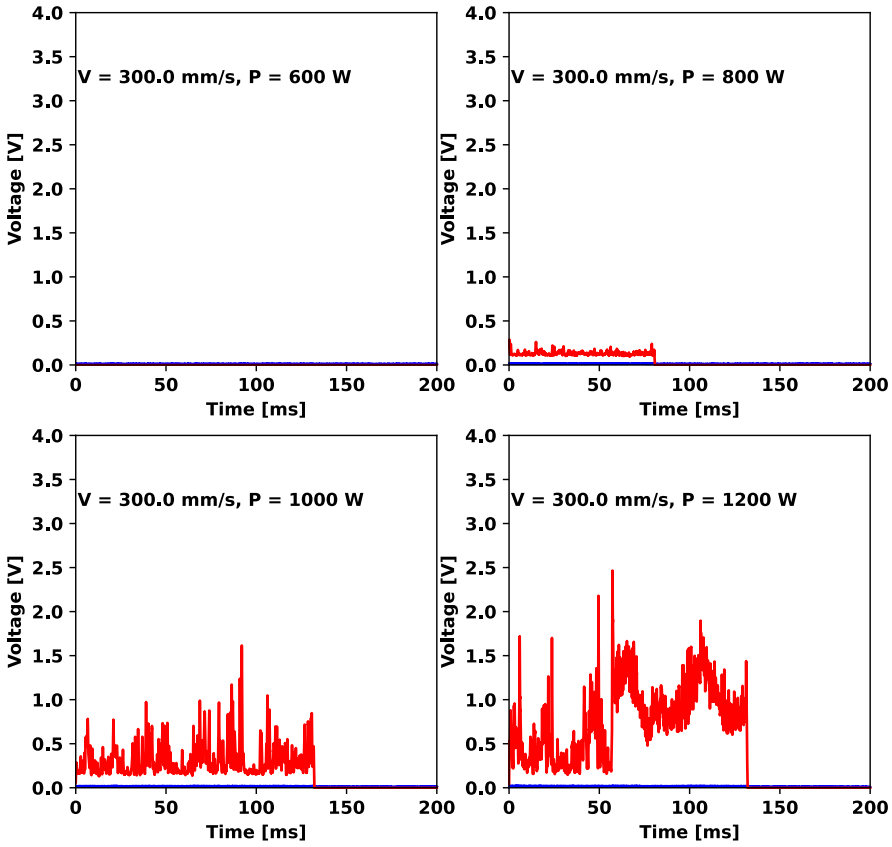

Figure 7.6: Cu and Al signals for the velocity of 300 mm/s and different laser power of 600 W, 800 W, 1000 W and 1200 W.

The Cu signal at 578 nm is plotted with a red colour line and the plot with the blue colour line is the Al signal at 396 nm from the bottom sheet. For laser power of 600 W, there is no Cu and Al signal, which shows that the laser power was not sufficient to vaporize the Cu. Increasing the laser power to 800 W, the Cu signal was recorded with the signal value of about 0.15 V. Further increasing the laser power to 1000 W and 1200 W, a higher value of the Cu signal in the range of 0.5 to 1.0 V is obtained.

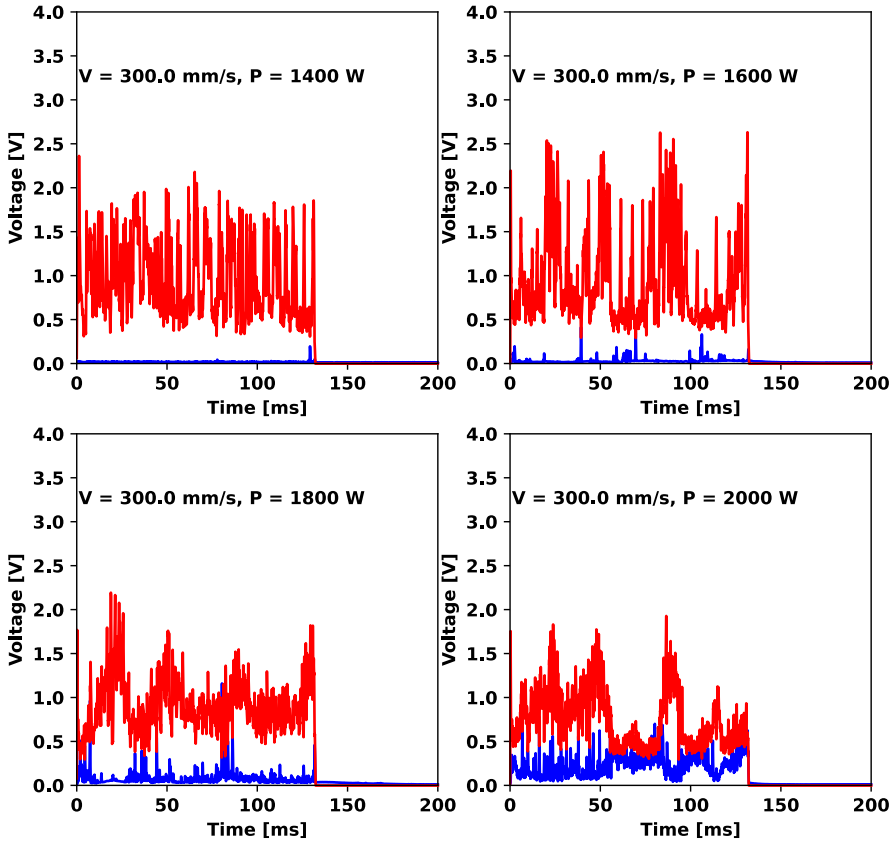

Figure 7.7: Cu and Al signals for the velocity of 300 mm/s and different laser power of 1400 W, 1600 W, 1800 W and 2000 W.

The subplots in figure 7.7 show the Al and Cu signals for laser powers of 1400 W, 1600 W, 1800 W and 2000 W. For laser power of 1400 W in figure 7.7, the Cu signal value further increases to a maximum value of about 2 V and the signal fluctuates between 0.5 V to 1.5 V. However, no significant Al signal is obtained except at the end of the weld around 130 ms. At laser power of 1600 W, the signal value further increases to a maximum value of 2.5 V and the signal value fluctuates between 0.5 V to 2.5 V. Correspondingly the Al signal was obtained for this condition with a maximum voltage of about 0.5 V. Further increasing the laser power to 1800 W the Cu signal value reduces. The signal amplitude value changes between 0.5 V to 1.5 V. However the Al signal value is increased to a maximum value of about 1 V and a denser melting of Al is recorded in comparison to the laser power of 1600 W. For maximum laser power of 2000 W, the Cu signal further decreases while the Al signal increases in comparison to laser power of 1800 W.

The mean value of the signal voltage for the Cu signal at 578 nm and Al signal at 396 nm is plotted in figure 7.8 for different laser powers. At laser power of 800 W, the mean value of the Cu signal is 0.18 V. As the laser power is increased to 1000 W and 1200 W, the mean value of the Cu

signal increases to a value of about 0.35 V and 0.8 V respectively. The maximum mean value of the Cu signal is obtained for the laser power of 1400 W and for further increasing the laser power to 1600 W and 1800 W, the mean value of the Cu signal decreases. For maximum laser power of 2000 W, the mean value of the Cu signal decreases significantly below 0.8 V. Therefore the mean value of the Cu signal increases as the laser power increases until 1400 W. After reaching a maximum value at 1400 W, the mean value of Cu signal then decreases as the laser power is increased until the maximum power of 2000 W. However, the mean value of the Al signal has an increasing trend as the laser power increases. For increasing the laser power until 1400 W there is no significant change in the mean value of the Al signal. For laser power of 1600 W, 1800 W and 2000 W the mean value of the Al signal increases significantly. Increasing the laser power value above 1400 W the mean value of the Al increases while the mean value of the Cu signal decreases.

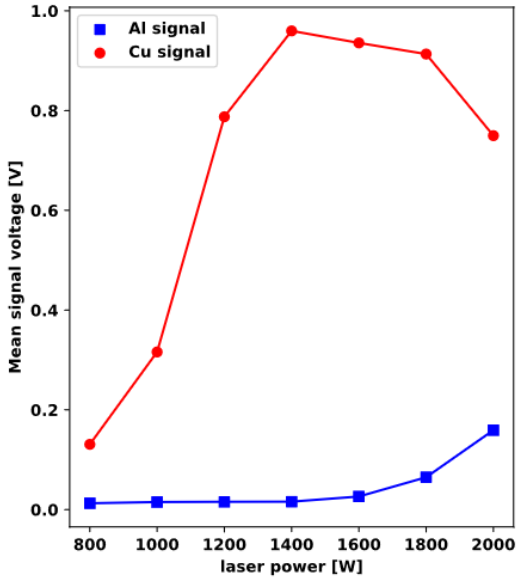

Figure 7.8: The plot of mean Cu and Al signal value [V] for different laser power

7.4.2 Effect of welding signal for different laser velocity

The welding signals for different velocities and laser power of 1800 W is shown in figure 7.9. The corresponding images of the weld seams on the top of Cu and bottom of Al are shown in figure 7.10. For a high laser speed of 600 mm/s, the Cu signal value changes between 2 V to 3 V. However no significant change in Al signal value is observed except for the small-signal peak in the beginning. For the same time period of the peak value in the Al signal, the value of the Cu signal is lower (0.8 V) in comparison to other regions. It is expected in welding with the spiral trajectory that the beginning of the welding results in higher melting due to the fact that the initial curves of the spirals

are closer as shown in figure 7.10 (a) and (b) (marked in dotted circles). Due to this reason at the beginning of the welding, a good melting of both the Al and Cu metals occurs even at a high speed of 600 mm/s (figure 7.10 (a)). The signals of Al and Cu are able to capture this condition precisely. Decreasing the velocity of welding to 500 mm/s, the Cu signal value changes between 1.8 V to 2.5 V and there is no significant change in the Al signal. Further decreasing the velocity to 400 mm/s and 300 mm/s, the Cu signal value changes between 0.75 V to 2.0 V and 0.5 to 1.2 V respectively. For 400 mm/s the Al signal has small peaks of value 1 V in the time interval of 50 ms to 100 ms. However, for 300 mm/s, a continuous Al signal is obtained for the entire duration of welding with a maximum value of 0.4 V.

Therefore decreasing the laser velocity leads to decreasing Cu signal value and increasing Al signal value.

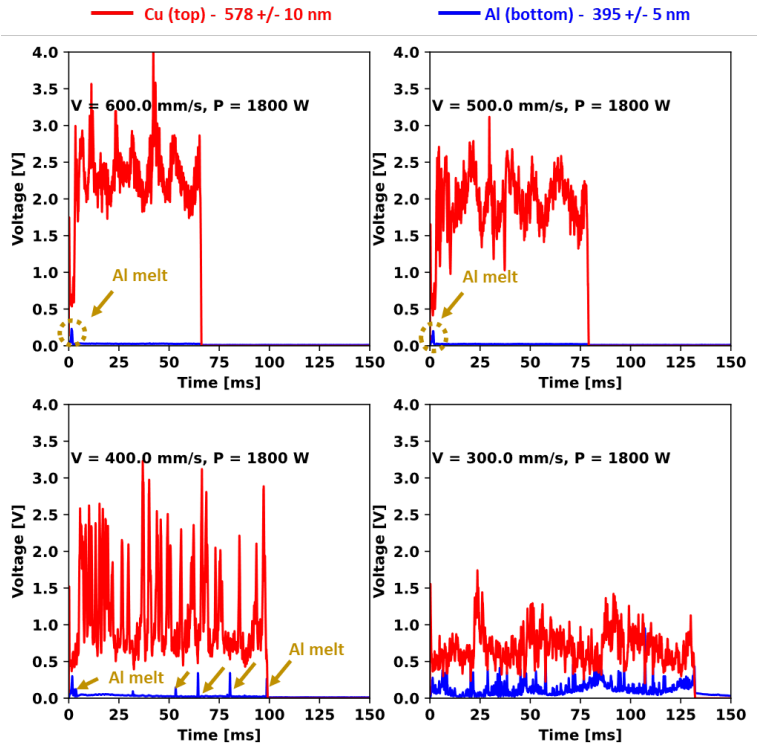

Figure 7.9: Cu and Al signals for the laser power of 1800 W and different velocities of 600 mm/s, 500 mm/s, 400 mm/s and 300 mm/s.

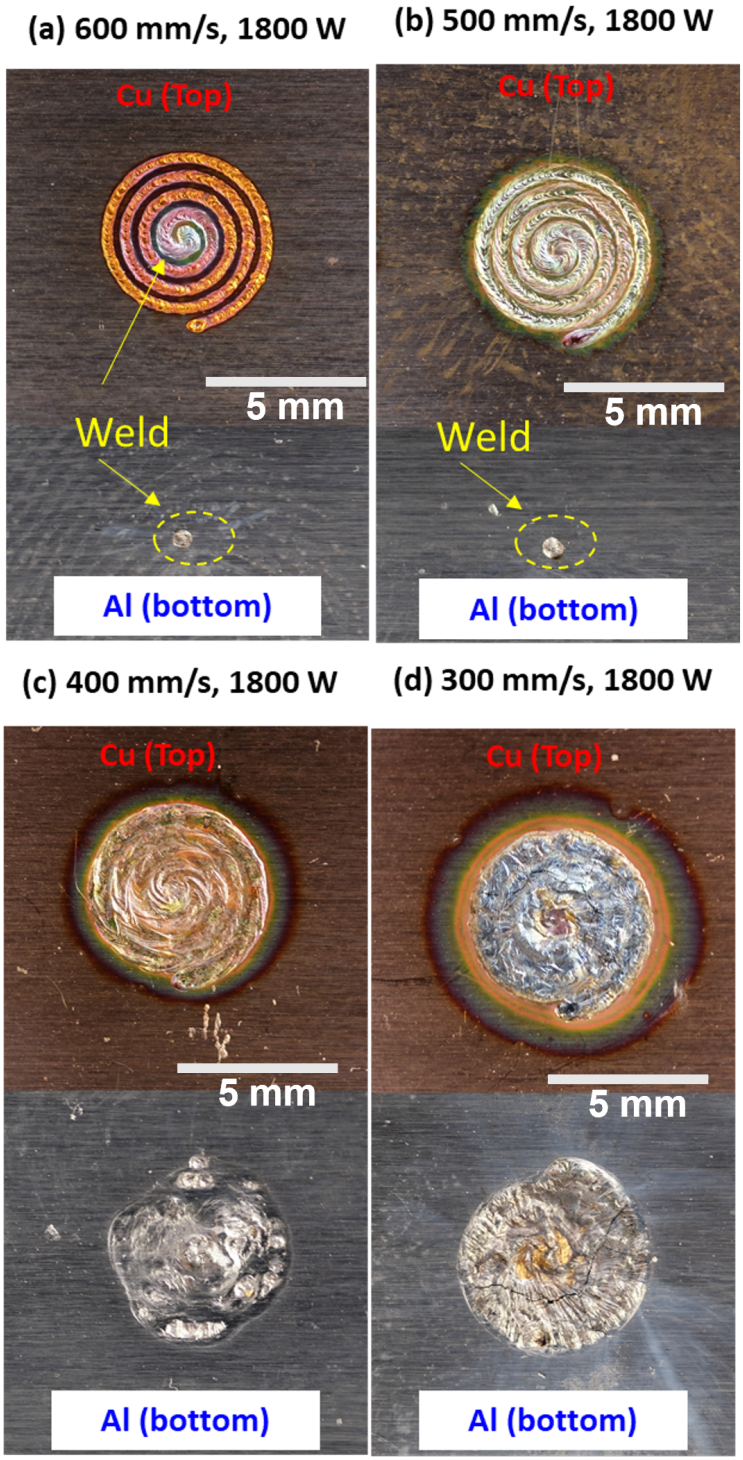

Figure 7.10: Top and bottom views of Cu and Al sheets for the laser power of 1800 W and velocities of 600 mm/s, 500 mm/s, 400 mm/s and 300 mm/s.

The plot in the figure 7.11 shows the effect of velocity on the mean signal value of Cu and Al

for laser power of 1800 W. As the velocity is increased (decreasing the laser energy per unit length) from 200 mm/s to 600 mm/s, the mean value of the Cu signal increases from 0.4 V to 2.3 V. On the contrary, the mean value of the Al signal decreases from 0.4 V to 0.1 V as the velocity is increased from 200 mm/s to 600 mm/s.

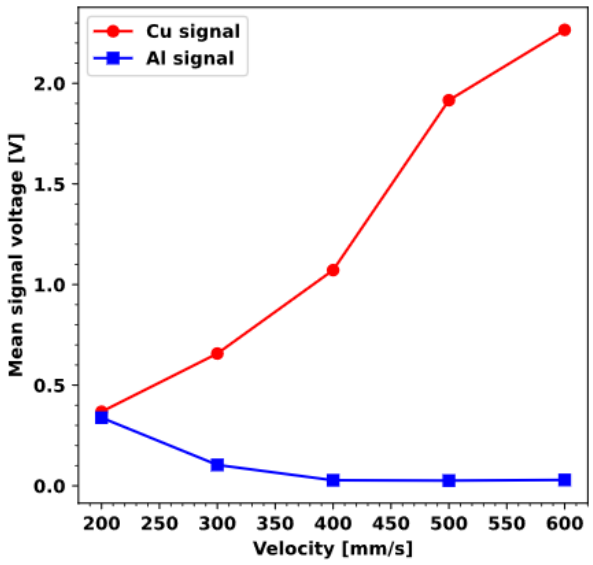

Figure 7.11: The plot of mean signal values of Cu and Al for different velocity

The following interpretations are made based on the (Al, Cu) welding signals and the images taken from the top and bottom of Cu and Al sheets.

- Corresponding to the Al and Cu signal values, the weld images show a clear relation to the amount of Al and Cu melted on the top and bottom respectively.
- High Cu signal and low Al signal result in the insufficient weld as shown in figure 7.10 (a)
- Low Cu signal and high Al signal results in an excessive weld with cracks and excessive Al melt in the fusion zone as shown in figure 7.10 (d)
- Optimum melt as shown in figure 7.10 (c) can be identified based on the Cu and Al welding signals

7.5 Identification of weld class

The mean value of the welding signal from the top of Cu at 578 nm and Al from the bottom at 396 nm is plotted in figure 7.12. As the mean value of the Cu signal increases, the mean value of

the Al signal decreases. The high value of mean Al signal value greater than 0.25 V represents high Al melting during the welding process and results in an excessive weld condition. On the contrary high value of the mean Cu signal greater than 1.5 V indicates low Al melting and high Cu melting on the top, which results in insufficient weld condition. There is a strong negative correlation of the mean Al signal to the mean Cu signal. The decrease in the Cu signal and increase in the Al signal indicates that the resulting vapour plume is ejected out of the welding zone. For the high value of Cu signal, the laser irradiation results in melting of Cu sheet (i.e., shallow depth) on the top creating a strong Cu plume.

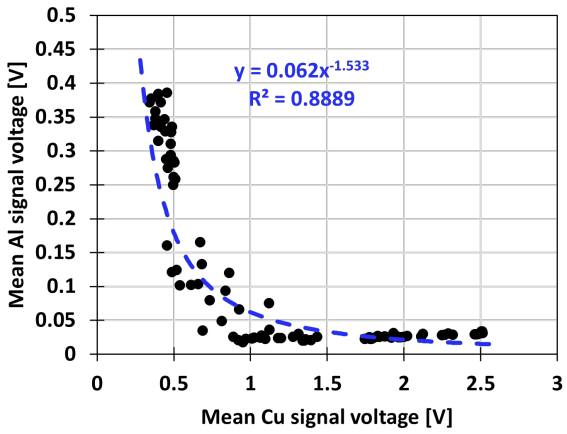

Figure 7.12: The plot of mean Al signal value over mean Cu signal value

Based on the mean value of Cu and Al signals, different welding classes such as insufficient weld (class 1), good weld/acceptable weld (class 2) and excessive weld (class 3) are identified. From the cross-sectional view of the class 1 weld shown in figure 7.13, the melted Al in the fusion zone is very small and the laser irradiation mainly melted the Cu metal. The mean signal value of Cu in this condition was greater than 1.5 V, which concludes that the weld is formed mainly due to melting of Cu and less Al melting. Therefore the low weld or insufficient weld class is rich in Cu signal and the weld plume is present on the top of the Cu sheet.

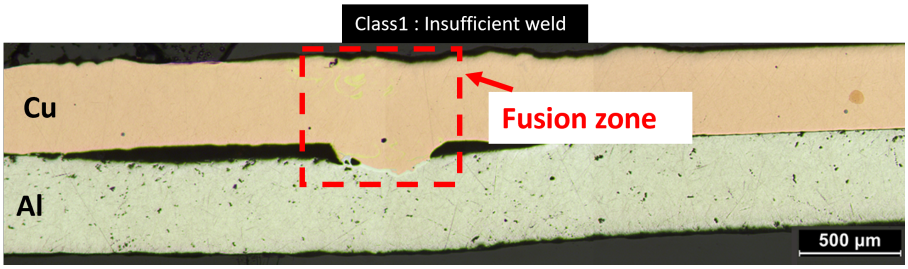

Figure 7.13: Cross-sectional view of insufficient weld condition (class 1) for Cu-Al spiral weld

The cross-sectional view of the class 2 weld is shown in the figure 7.14. In the class 2 weld, the Al melted in the fusion zone is increased in comparison to the class 1 weld. In this case, the mean signal value of Cu on the top decreased below 1.5 V and the mean Al signal value on the bottom sheet increased up to 0.1 V. For class 2 welds the irradiated laser is absorbed deeper into the Cu sheet and the weld signal for Cu is decreased in comparison to the class 1 weld. This is also confirmed by the increase in the mean value of the Al melting signal obtained from the bottom sheet. Therefore, in this condition (class 2) the melting of both Al and Cu is indicated by the increase in Al signal and a decrease in Cu signal as the laser radiation is penetrated deep into the Cu and Al sheets.

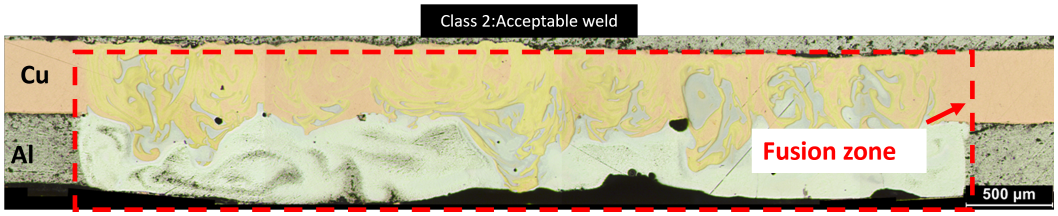

Figure 7.14: Cross-sectional view of the good/acceptable weld (class 2) for Cu-Al spiral weld

The excessive weld condition is shown in the cross-sectional view in figure 7.15. The irradiated laser in this case penetrates deep into the Al sheet thereby melting both Cu and Al sheets. The fusion zone for class 3 weld is a complete mixture of Cu and Al resulting in excessive intermixing and results in several large intermetallic phases and cracks. As the laser is penetrated deeper into the bottom of the Al sheet, the Al metal plume is formed in the bottom sheet, which is seen from the increase of the mean value of the Al signal and decrease in the mean value of the Cu signal.

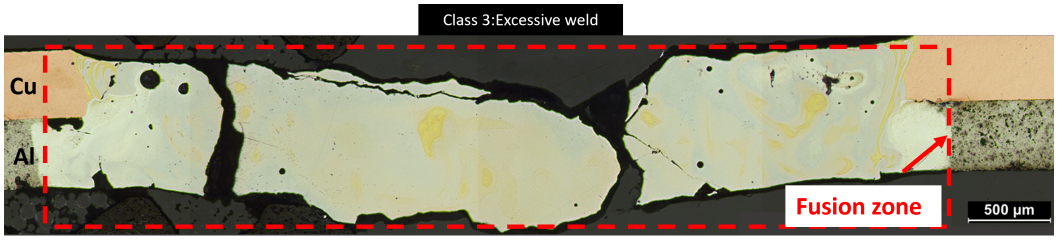

Figure 7.15: Cross-sectional view of excessive weld condition (class 3) for Cu-Al spiral weld

Therefore, the melting of Cu and Al in the fusion zone such as an insufficient weld, good/acceptable weld and excessive weld can be identified from the mean value of Cu and Al signal from the top and bottom sheets respectively.

Based on the previous discussions in section 7.3 and 7.4 with line and spiral weld trajectories regarding the welding signals for Cu (on the top sheet) and Al (bottom sheet) for different laser power and velocities, a schematic of the plume formation on the top of Cu sheet and the bottom of

Al sheet is summarized in the figure 7.16. However, the exact representation of the plasma plume/ plasma shape is not intended in the schematic diagram, since the study of plasma and keyhole formation is not intended for this research and a dedicated study is required.

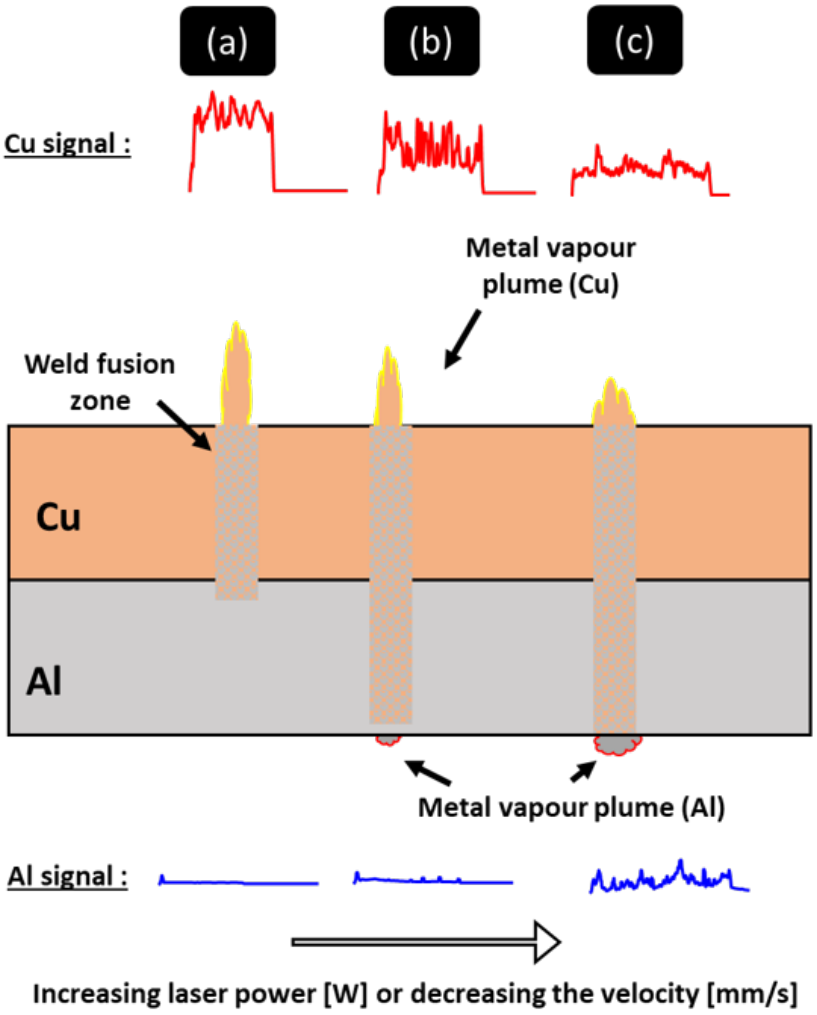

Figure 7.16: Schematic of weld plume based on the Cu and Al welding signals, as the weld depth into the base metal changes

For the shallow weld depth into Al sheet (case (a) in figure 7.16), the plume is present on the top of Cu and a higher Cu signal is obtained. For a deeper weld into the Al sheet (case (b) in figure 7.16), the Cu signal decreases since the melting of Al also happens. The plume on the top further sinks into the material as the keyhole is deeper into the Al sheet. For an excessive weld (case (c) in figure 7.16), the Cu plume further sinks into the base metal and the Al plume from the bottom of the base metal is stronger.

The plot in figure 7.17 shows the mean value of Al and Cu signals for laser powers of 1600 W,

1800 W and 2000 W. The respective weld classes such as class 1, class 2 and class 3 are shown in different marker colours. For each subplot in figure 7.17 minimum of 23 welds were used.

For 1600 W, the class 1 weld/ insufficient weld can be identified as the mean value of Cu signal greater than 1.25 V and mean value of Al less than 0.1 V. The class 3 weld can be identified as a mean value of Al signal greater than 0.2 V and mean value of Cu signal less than 0.6 V. The acceptable weld has the mean value of Cu signal in the range of 1.25 V - 0.8 V and mean value of Al signal below 0.1 V.

As the laser power is increased to 1800 W, the mean Cu signal value in class 1 increases to the range of 1.8 - 2.5 V in comparison to 1600 W. In contrast to the class 3 welds at 1800 W, the Al signal value decreased to 0.1 V. The acceptable weld has the mean value of Cu signal in the range of about 1.25 - 0.6 V and mean value of Al signal less than 0.1 V.

Similarly, as the laser power is increased to 2000 W, the class 1 weld reached a mean value of Cu signal as high as 2.5 V. The class 3 weld on the contrary has increased mean value of Al signal greater than 0.2 V. The acceptable weld (class 2) is found between the mean value of Cu signal at 1.1 V and mean value of Al signal at 0.2 V as marked in the dotted circle in plots.

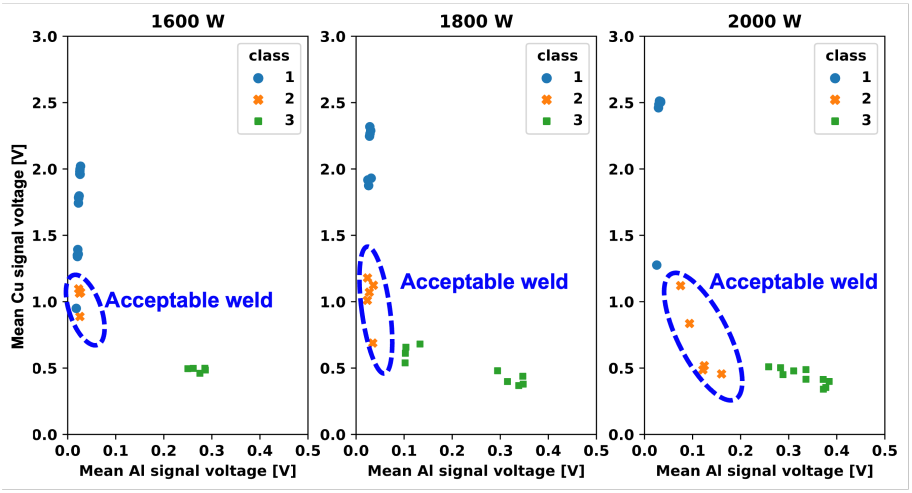

Figure 7.17: Plots of mean Cu signal value over mean Al signal value for different laser power of 1600 W, 1800 W and 2000 W.

Therefore, based on the applied laser power, the mean value of Cu signal and mean value of Al signal, weld classes such as insufficient weld (class 1), acceptable weld (class 2) and excessive weld (class 3) can be identified.

7.6 Convolutional neural network model for identification of weld classes

It was shown in the previous section 7.5 that based on the mean value of the welding signals, the weld class can be identified. In this section, a 1-dimensional CNN model is proposed for the prediction of the weld classes from the welding signal itself rather than the mean value of the signal. The 1-dimensional CNN model is proposed as an alternative approach because it can automatically extract the relevant information from the welding signal based on the provided data/examples. For this approach, the welding signal is split into a time frame of 30 ms or a length of 3000 (0.03 s $\times$ 100000 Hz). The plot in figure 7.18 shows the example of the Cu signals for weld class 1, class 2 and class 3. Such a signal of length 3000 (30 ms) is used as input for the 1D CNN model.

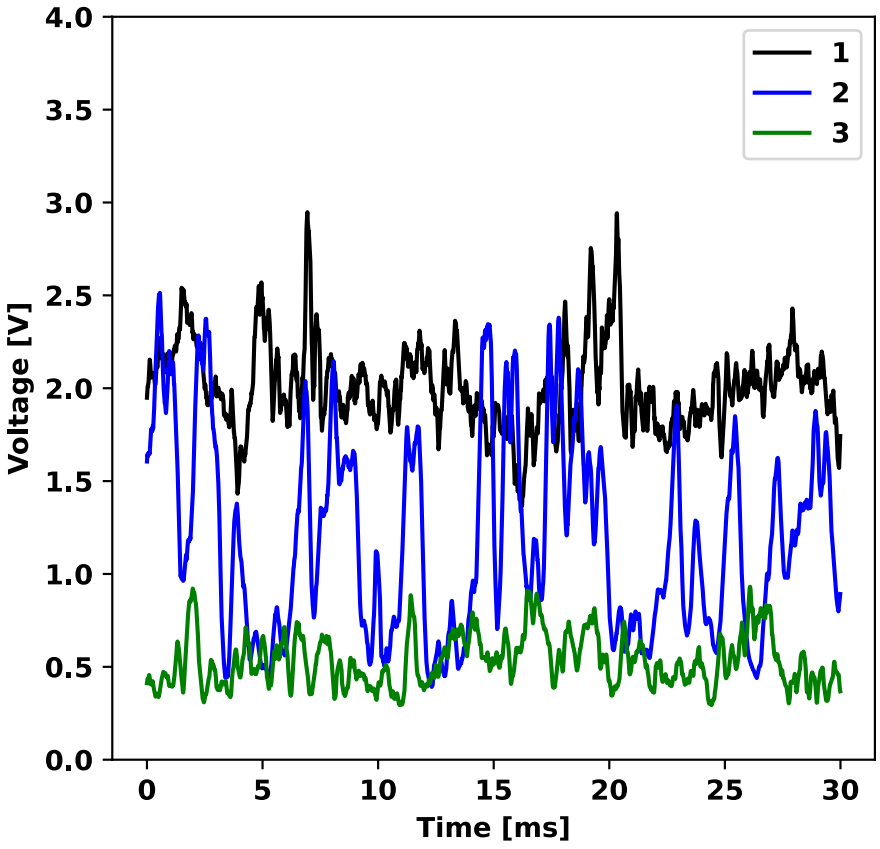

Figure 7.18: Example of input signals for CNN network model

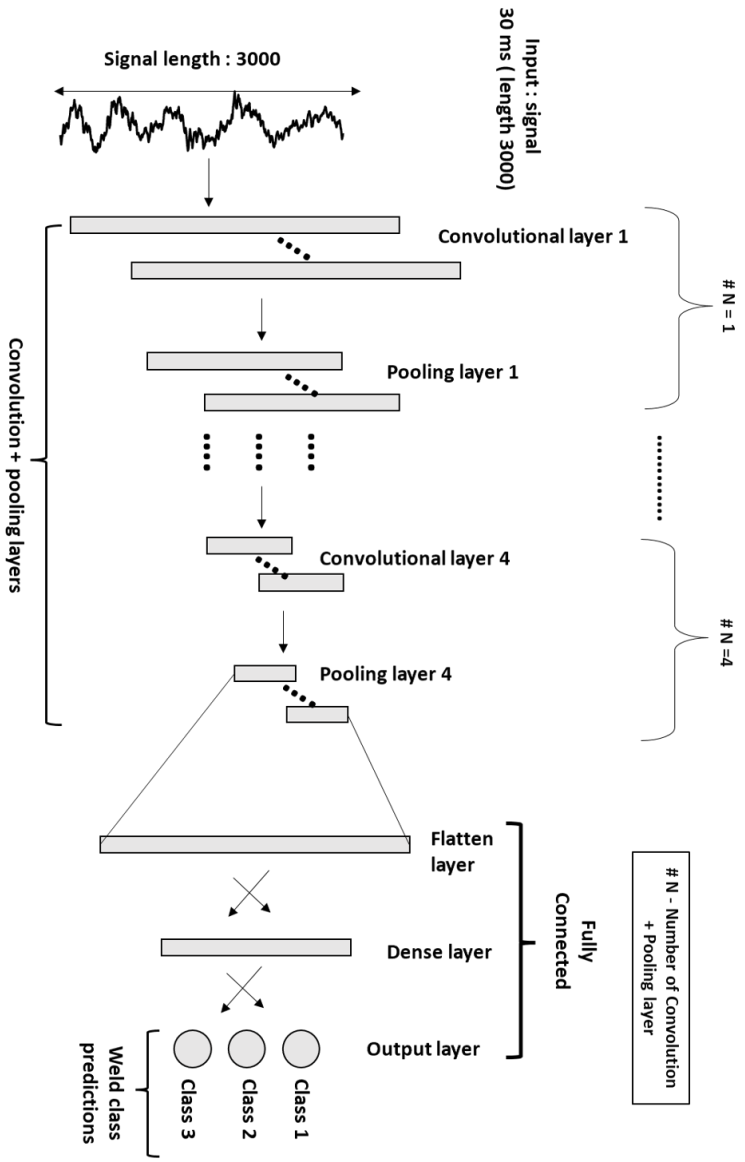

Figure 7.19: Schematic of the 1-dimensional CNN architecture with four convolutional and pooling layers (N=4) for identification of weld class using the weld signal as input

The schematic of the 1-dimensional CNN architecture with four convolutional and pooling layers is shown in the figure 7.19. The data in this context is one dimensional signal in contrast to the weld images in chapter 6. In the convolutional layer, the input data is convoluted with a filter of size 5. For all convolutional layers, the number of filters used is 64. The output of the convolutional layer is the input to the max-pooling layer. In the max-pooling layer, the maximum value of each patch (patch size = 2) is calculated. After the sequence convolution and pooling operations, the output is flattened in the flattened layer and fed into a dense layer of size 64. The final output

layer is of size 3 to predict the three weld classes such as class 1 ("insufficient weld"), acceptable weld (class 2) and excessive weld (class 3). Each of the convolutional layers is activated with a rectified linear unit activation function ("ReLU" in Keras). The final dense layer is activated with a softmax activation function to normalize the output (prediction of the weld class) of the network to a probability distribution over the predicted output classes. For training the model, the "Adam" optimizer and the loss function "sparse categorical crossentropy" [2, 17] is used. The overview of the 1-dimensional CNN model is shown in the table 7.1. After training the model for 25 iterations, the model was able to predict the weld classes with an accuracy of 90% on the new unseen data.

Description	Value
Model input	1-dimensional signal
Signal length	30 ms
Model output	Class 1, Class 2, Class 3
Number of training samples	123
Number of validation samples	53
Validation accuracy	90 %

Table 7.1: Overview of the 1-dimensional CNN model

The objective of the 1-dimensional CNN approach in this thesis was to show that using the welding signal, the weld classes can be predicted. Based on the proposed approach further extension of this model to detect the anomaly is suggested for future works.

7.7 Summary

The optical emission (plume wavelength of 396 nm and 578 nm) during the welding process was collected and analysed. The Cu signal value on the top of the weld seam decreased as the laser power increased and the velocity decreased. Conversely, the Al signal value from the bottom sheet increased when the laser power increased and the velocity decreased. The keyhole/ weld depth is very influential on the plasma plume formation and the welding signal. Using the mean values of the Al and Cu signals the weld status such as low weld, acceptable weld and excessive weld conditions can be identified in real-time. Furthermore, the 1-dimensional CNN approach was shown to predict the weld class based on the welding signal as input. With these insights, closed-loop control of the process can also be developed in future.

- The Cu and Al signals acquired during the welding process were successfully utilized for identification of different weld types such as insufficient weld, good weld (acceptable weld) and excessive weld.

Chapter 8

Summary and outlook

Laser welding of Copper and Aluminium, starting from the highly reflective copper side was studied and summarised in this thesis. Laser welding of Copper is difficult due to the physical phenomenon of laser processing (high reflection of copper for infrared light) and from the metallurgical aspect due to the formation of brittle intermetallic compounds.

With high power laser wavelength of 1030 mn (power intensity of 1×10^7 W/cm^2) welding of Cu in keyhole mode was possible. The spiral laser trajectory allowed to creation of a circular weld profile that appears like a spot weld. The spiral trajectory movement was advantageous in enlarging the weld seam diameter and provides sufficient melting of Cu and Al in the fusion zone. High diffusion of Al and Cu occurred considering the high heat input required for melting copper. In theory, this favours the formation of intermetallic compounds of Al-Cu that are brittle. However, because of melting from the Cu sheet, a higher Al can be melted. Since the Cu has a higher solubility for Al (18.5 %) in comparison to the solubility of Al for Cu (2.5 %). Moreover, the laser trajectory in form of spirals was utilized to impact the metallurgical reaction. The idea of increasing the intermixing to form a fully diffused Cu-Al weld resulted in a combination of large ductile and small brittle phases in the fusion zone. The interface of intermetallic compounds are displaced away into the bulk of Al and Cu material and a wavy interface was obtained in the fusion. The most brittle phases are identified in the range of 50-80 at% of Cu. Such a brittle interface is intermixed and is small. This leads to a stronger joint which was shown with microstructure analysis, tensile shear test and failure analysis. From the EDS composition analysis, the formation of Cu solid solution and two-phase region $Al{+}CuAl_2$ in the joint was found to be beneficial, which is one of the most ductile phases for the Al-Cu combination. Therefore, the study shows the possibility of using fusion joining of Cu and Al to obtain a stronger joint by promoting good phase compositions in the joint.

For a strong joint defined amount of Al and Cu melt is required in the fusion zone. An automatic

non-destructive approach to identify the weld conditions such as no-weld, low weld, good weld (ok weld) and high weld was investigated using the optical images taken from the top of the weld seam. The proposed CNN model was able to identify the weld classes with an accuracy of over 92 %. Further, it was shown that the model was able to extract specific features related to the individual weld classes.

For real-time analysis, photodiodes at a sampling rate of 100 kHz were used to study the process signals. The optical emission during the welding process at wavelengths of 396 nm and 578 nm was found to correlate to the laser process parameters such as laser power and velocity. The Cu and Al welding signals were able to locate the regions of higher Al melting. In addition, different degrees of Al and Cu melting in the welding direction (lateral cross-sections) were detected using the Cu and Al welding signals in real-time. The Cu signal value on the top of the weld seam decreased as the laser power increased and the velocity decreased. Conversely, the Al signal value from the bottom sheet increased when the laser power increased and the velocity decreased. The keyhole/ weld depth was very influential on the plasma plume formation and the welding signal value. The mean values of the Al and Cu signals were used to identify the weld status such as a low weld, acceptable weld (good weld) and excessive weld.

In conclusion, this thesis provided an alternative strategy to weld Cu-Al with a spiral trajectory that is analogous to an enlarged spot weld. For the chosen trajectory an automatic non-destructive method using the CNN model (convolutional neural network) was proposed to identify different weld statuses (weld classes). Finally using photodiodes the possibility of real-time indication of weld status was shown.

The presented work was disseminated in journal publication/conference proceeding (7) and conference presentation (9) (as detailed on pages 120 and 121).

Chapter 9

Future works

The future works to continue based on the current results is described in this section. The following areas are identified for future work based on the fusion welding technique put forward in this thesis.

- Based on the proposed spiral trajectory and post-process analysis techniques, other dissimilar combinations can also be carried out as future work. Some of the other interesting material combinations to weld for industrial applications are Cu-Steel, Cu- Titanium, Al- Steel.
- The laser power of the green laser (515 nm) and blue laser (480 nm) is improving due to increasing demand to weld Copper, welding Cu-Al with other lasers sources could be studied.
- The future work can be carried out to extend the Neural Network model with alternative network configurations and utilize the graphical processing unit (GPU) or high-performance computing.
- Increasing the size of data and utilizing high-speed camera recording for inline processing.
- A multi-sensor approach using optical emission, acoustic emission, and image processing is also proposed. This can lead to an improved automatic inspection system for laser welding. It is also suggested to use an automatic laser cabin for welding to improve productivity.

List of publications:

1. K. Mathivanan and P. Plapper, "Correlation of optical signal during laser fusion welding of copper to aluminum," J. Laser Appl., vol. 33, no. 1, p. 012037, 2021, doi: 10.2351/7.0000314

2. K. Mathivanan and P. Plapper, "Prediction of Cu-Al weld status using convolutional neural network," in Conference proceeding of Lasers in Manufacturing (LiM), 2021,

3. K. Mathivanan and P. Plapper, "Artificial neural network to predict the weld status in laser welding of copper to aluminum," Procedia CIRP, vol. 103, pp. 61–66, Jan. 2021, doi: 10.1016/j.procir.2021.10.009.

4. K. Mathivanan and P. Plapper, "Welding copper to aluminium with green laser wavelength of 515 nm," Proc. Int. Congr. Appl. Lasers Electro-Optics 2020

5. K. Mathivanan and P. Plapper, "Laser welding of dissimilar copper and aluminum sheets by shaping the laser pulses," Procedia Manuf., vol. 36, pp. 154–162, 2019 doi:10.1016/j.promfg.2019.08.021.

6. K. Mathivanan and P. Plapper, "Laser overlap joining from copper to aluminum and analysis of failure zone," in Conference proceeding of Lasers in Manufacturing (LiM), 2019, pp. 1–11.

7. P. Schmalen, K. Mathivanan, and P. Plapper, "Metallographic Studies of Dissimilar Al-Cu Laser-Welded Joints Using Various Etchants," Metallogr. Microstruct. Anal., 2018, doi: https://doi.org/10.1007/s13632-018-0501-y.

List of conference presentations:

1. Laser Welding of Copper to Aluminum with Spiral Trajectory and Identification of Excessive Aluminum Melting, ICALEO 2021, USA, 2021

2. Prediction of Cu-Al weld status using convolutional neural network, Lasers in Manufacturing (LiM), Munich, 2021

3. Artificial neural network to predict the weld status in laser welding of copper to aluminum, CIRPe 2021, 2020

4. Correlation of optical signal during laser fusion weld-ing of Copper to Aluminum, ICALEO 2020, USA, 2020

5. Welding Copper to Aluminum with green laser wave-length of 515 nm, ICALEO 2020, USA, 2020

6. Laser welding of dissimilar copper and aluminum sheets by shaping the laser pulses, NOLAMP17, Norway, 2019

7. Laser overlap joining from copper to aluminum and analysis of failure zone, Lasers in Manufacturing - LiM , Munich, 2019

8. Laser beam joining of copper to aluminum sheet Advanced Battery Power , Aachen, 2019

9. Autogenous Laser welding of copper to aluminium , ICPEPA 11 , Lithuania, 2018

Bibliography

[1] B. J. Aalderink, R. G. K. M. Aarts, B. Jonker, and J. Meijer. Weld Plume Emissions During Nd : YAG Laser Welding. *Third International WLT-Conference on Lasers in Manufacturing 2005,Munich*, 1:413–417, 2005.

[2] M. Abadi, P. Barham, J. Chen, Z. Chen, A. Davis, J. Dean, M. Devin, S. Ghemawat, G. Irving, and M. Isard. Tensorflow: A system for large-scale machine learning. 1:265–283, 2016.

[3] M. Abbasi, A. Karimi Taheri, and M. T. Salehi. Growth rate of intermetallic compounds in Al/Cu bimetal produced by cold roll welding process. *Journal of Alloys and Compounds*, 319(1-2):233–241, 2001.

[4] J. Alonso. The Factors Influencing Solid Solubility in Metallic Alloys. *Revista Latinoamericana de Metalurgia y Materiales*, 5(4):1, 1985.

[5] S. Amorosi, T. Sidler, R. P. Salathé, H. P. Schwob, and J. Hertzberg. Laser microspot welding of copper. *Journal of Laser Applications*, 16(3):134–139, 2004.

[6] S. T. Auwal, S. Ramesh, F. Yusof, and S. M. Manladan. A review on laser beam welding of copper alloys. *The International Journal of Advanced Manufacturing Technology*, (February):1–16, 2018.

[7] Y. M. Baqer, S. Ramesh, F. Yusof, and S. M. Manladan. Challenges and advances in laser welding of dissimilar light alloys: Al/Mg, Al/Ti, and Mg/Ti alloys. *International Journal of Advanced Manufacturing Technology*, 95(9-12):4353–4369, 2018.

[8] C. A. Biffi, K. Mathivanan, and A. Tuissi. Laser-Induced Superelasticity in NiTinol Stent Strut. *Shape Memory and Superelasticity*, 2018.

[9] G. Bradski. The OpenCV Library. *Dr. Dobb's Journal of Software Tools*, 2000.

[10] M. J. Brand, P. A. Schmidt, M. F. Zaeh, and A. Jossen. Welding techniques for battery cells and resulting electrical contact resistances. *Journal of Energy Storage*, 1(1):7–14, 2015.

[11] M. Braunovic, L. Rodrigue, and D. Gagnon. Nanoindentation study of intermetallic phases in Al-Cu bimetallic system. *Electrical Contacts, Proceedings of the Annual Holm Conference on Electrical Contacts*, 1:270–275, 2008.

[12] M. S. Brown and C. B. Arnold. Laser Precision Microfabrication. 135:91–120, 2010.

[13] W. Cai, P. Jiang, L. Shu, S. Geng, and Q. Zhou. Real-time laser keyhole welding penetration state monitoring based on adaptive fusion images using convolutional neural networks. *Journal of Intelligent Manufacturing*, 1:1–15, 2021.

[14] W. W. Cai. *Ultrasonic Welding of Lithium-Ion Batteries*. ASME Press, 03 2017.

[15] W. Callister and D. Rethwisch. *Materials Science and Engineering: An Introduction*. Wiley, 2018.

[16] H. B. Cary and S. C. Helzer. *Modern welding technology*. Prentice-Hall Upper Saddle River, NJ, 1979.

[17] F. Chollet. *Deep learning with Python*. Simon and Schuster, 2021.

[18] S. S. Ciobanu, C. Negutu, M. Stafe, I. Vladoiu, V. Pais, V. Stancalie, and N. N. Puscas. Spectroscopic studies of laser induced aluminium and copper plasmas in air. *35th EPS Conference on Plasma Phys.*, 32(June):2–5, 2008.

[19] D. Colombo, B. M. Colosimo, and B. Previtali. Comparison of methods for data analysis in the remote monitoring of remote laser welding. *Optics and Lasers in Engineering*, 51(1):34–46, 2013.

[20] G. Colonna, A. Laricchiuta, and L. D. Pietanza. Modeling plasma heating by ns laser pulse. *Spectrochimica Acta Part B: Atomic Spectroscopy*, 141:85–93, 2018.

[21] J. Dai, X. Wang, L. Yang, J. Huang, Y. Zhang, and J. Chen. Study of plasma in laser welding of magnesium alloy. *The International Journal of Advanced Manufacturing Technology*, 73(1-4):443–447, 2014.

[22] A. Das, D. Li, D. Williams, and D. Greenwood. Joining Technologies for Automotive Battery Systems Manufacturing. *Evs30*, (c):1–12, 2017.

[23] A. Das, D. Li, D. Williams, and D. Greenwood. Weldability and shear strength feasibility study for automotive electric vehicle battery tab interconnects. *Journal of the Brazilian Society of Mechanical Sciences and Engineering*, 41(1), 2019.

[24] S. Engel. Sourcebook on applications of the laser in metalworking. *Ed.: Metzbower, EA Metals Park, American Society for Metals*, 1981.

[25] S. Engler, R. Ramsayer, and R. Poprawe. Process studies on laser welding of copper with brilliant green and infrared lasers. *Physics Procedia*, 12(PART 2):342–349, 2011.

[26] I. C. Ezenwa, R. A. Secco, W. Yong, M. Pozzo, and D. Alfè. Electrical resistivity of solid and liquid Cu up to 5 GPa: Decrease along the melting boundary. *Journal of Physics and Chemistry of Solids*, 110(April):386–393, 2017.

[27] R. Fabbro. Scaling laws for the laser welding process in keyhole mode. *Journal of Materials Processing Technology*, 264(September 2018):346–351, 2019.

[28] R. Fabbro, M. Dal, P. Peyre, F. Coste, M. Schneider, and V. Gunenthiram. Analysis and possible estimation of keyhole depths evolution, using laser operating parameters and material properties. *Journal of Laser Applications*, 30(3):032410, 2018.

[29] M. Faucon, A. Laffitte, J. Lopez, and R. Kling. Surface blackening by laser texturing with high repetition rate femtosecond laser up to 1MHz. *Proc. of SPIE*, 8972(February):89721M, 2014.

[30] F. Fetzer, M. Jarwitz, P. Stritt, R. Weber, and T. Graf. Fine-tuned remote laser welding of aluminum to copper with local beam oscillation. *Physics Procedia*, 83:455–462, 2016.

[31] A. Fortunato and A. Ascari. Laser Welding of Thin Copper and Aluminum Sheets: Feasibility and Challenges in Continuous-Wave Welding of Dissimilar Metals. *Lasers in Manufacturing and Materials Processing*, 6(2):136–157, 2019.

[32] B. Fotovvati, S. F. Wayne, G. Lewis, and E. Asadi. A Review on Melt-Pool Characteristics in Laser Welding of Metals. *Advances in Materials Science and Engineering*, 2018, 2018.

[33] I. Galvão, J. Oliveira, A. Loureiro, and D. Rodrigues. Formation and distribution of brittle structures in friction stir welding of aluminium and copper: influence of process parameters. *Science and Technology of Welding and Joining*, 16(8):681–689, 2011.

[34] J. Gedicke, B. Mehlmann, A. Olowinsky, and A. Gillner. Laser Beam Welding of Electrical Interconnections for Lithium-Ion. *Icaleo*, 844(2010):844–849, 2010.

[35] M. Harooni and R. Kovacevic. Laser welding of magnesium alloys: Issues and remedies. In *Magnesium Alloys*. IntechOpen, 2017.

[36] C. R. Harris, K. J. Millman, S. J. van der Walt, R. Gommers, P. Virtanen, D. Cournapeau, E. Wieser, J. Taylor, S. Berg, N. J. Smith, R. Kern, M. Picus, S. Hoyer, M. H. van Kerkwijk, M. Brett, A. Haldane, J. F. del Río, M. Wiebe, P. Peterson, P. Gérard-Marchant, K. Sheppard, T. Reddy, W. Weckesser, H. Abbasi, C. Gohlke, and T. E. Oliphant. Array programming with NumPy. *Nature*, 585(7825):357–362, Sept. 2020.

[37] A. Heider, J. Sollinger, F. Abt, M. Boley, R. Weber, and T. Graf. High-speed X-ray analysis of spatter formation in laser welding of copper. *Physics Procedia*, 41(January 2016):112–118, 2013.

[38] K. M. Hong and Y. C. Shin. Prospects of laser welding technology in the automotive industry: A review. *Journal of Materials Processing Technology*, 245:46–69, 2017.

[39] C. K. Hu and B. Luther. Electromigration in two-level interconnects of Cu and Al alloys. *Materials Chemistry & Physics*, 41(1):1–7, 1995.

[40] S. Huber, J. Glasschroeder, and M. Zach. Analysis of the Metal Vapour during Laser Beam Welding. *Physics Procedia*, 12:712–719, 2011.

[41] M. Jarwitz, F. Fetzer, R. Weber, and T. Graf. Weld Seam Geometry and Electrical Resistance of Laser-Welded, Aluminum-Copper Dissimilar Joints Produced with Spatial Beam Oscillation. *Metals*, 8(7):510, 2018.

[42] G. Ji and J.-P. Morniroli. Electron diffraction characterization of a new metastable Al ₂ Cu phase in an Al–Cu friction stir weld. *Journal of Applied Crystallography*, 46(2):430–442, 2013.

[43] K. Kamimuki, T. Inoue, K. Yasuda, M. Muro, T. Nakabayashi, and A. Matsunawa. Behaviour of monitoring signals during detection of welding defects in YAG laser welding. Study of monitoring technology for YAG laser welding (Report 2). *Welding International*, 17(3):203–210, 2003.

[44] M. Kang, T. Park, C. Kim, and J. Kim. Laser Welding Characteristics of Aluminum and Copper Sheets for Lithium-ion Batteries. 31(6):58–64, 2013.

[45] H. Ki, P. S. Mohanty, and J. Mazumder. Modeling of laser keyhole welding: Part I. Mathematical modeling, numerical methodology, role of recoil pressure, multiple reflections, and free surface evolution. *Metallurgical and Materials Transactions A: Physical Metallurgy and Materials Science*, 33(6):1817–1830, 2002.

[46] H. J. Kim, J. Y. Lee, K. W. Paik, K. W. Koh, J. H. Won, S. H. Choi, J. Lee, J. T. Moon, and Y. J. Park. Effects of Cu/Al intermetallic compound (IMC) on copper wire and aluminum pad bondability. *Advances in Electronic Materials and Packaging 2001*, (May 2013):44–51, 2001.

[47] C. Knaak, U. Thombansen, P. Abels, and M. Kröger. Machine learning as a comparative tool to determine the relevance of signal features in laser welding. *Procedia CIRP*, 74:623–627, 2018.

[48] A. R. Konuk, R. G. K. M. Aarts, A. J. Huis, T. Sibillano, and D. Rizzi. Process Control of Stainless Steel Laser Welding using an Optical Spectroscopic Sensor. 12:744–751, 2011.

[49] M. H. Kouters, G. H. Gubbels, and O. Dos Santos Ferreira. Characterization of intermetallic compounds in Cu-Al ball bonds: Mechanical properties, interface delamination and thermal conductivity. *Microelectronics Reliability*, 53(8):1068–1075, 2013.

[50] O. Kwon, H. G. Kim, W. Kim, G. H. Kim, and K. Kim. A convolutional neural network for prediction of laser power using melt-pool images in laser powder bed fusion. *IEEE Access*, 8:23255–23263, 2020.

[51] S. Lee. *Process and Quality Characterization for Ultrasonic Welding of Lithium-Ion Batteries.* PhD thesis, University of Michigan, United States, 2013.

[52] S. J. Lee, H. Nakamura, Y. Kawahito, and S. Katayama. Effect of welding speed on microstructural and mechanical properties of laser lap weld joints in dissimilar Al and Cu sheets. *Science and Technology of Welding and Joining*, 19(2):111–118, 2014.

[53] S. S. Lee, T. H. Kim, S. J. Hu, W. W. Cai, and J. A. Abell. Joining Technologies for Automotive Lithium-Ion Battery Manufacturing: A Review. *ASME 2010 International Manufacturing Science and Engineering Conference, Volume 1*, (May):541–549, 2010.

[54] A. Leitz. *Laserstrahlschweißen von Kupfer- und Aluminiumwerkstoffen in Mischverbindung*, volume 91. 2015.

[55] F. Lerra, A. Ascari, and A. Fortunato. The influence of laser pulse shape and separation distance on dissimilar welding of Al and Cu films. *Journal of Manufacturing Processes*, 45(April):331–339, 2019.

[56] J. Li, R. N. Raoelison, T. Sapanathan, G. Racineux, and M. Rachik. Assessing the influence of fieldshaper material on magnetic pulse welded interface of Al/Cu joints. *Procedia Manufacturing*, 29(April):337–344, 2019.

[57] J. C. Lippold. *Welding metallurgy and weldability*. John Wiley & Sons, 2014.

[58] A. Mannucci, I. Tomashchuk, V. Vignal, P. Sallamand, and M. Duband. Parametric study of laser welding of copper to austenitic stainless steel. *Procedia CIRP*, 74:450–455, 2018. 10th CIRP Conference on Photonic Technologies [LANE 2018].

[59] K. Mathivanan and P. Plapper. Laser welding of dissimilar copper and aluminum sheets by shaping the laser pulses. *Procedia Manufacturing*, 36:154–162, 2019.

[60] K. Mathivanan and P. Plapper. Welding copper to aluminium with green laser wavelength of 515 nm. *Proceedings of the International Congress of Applications of Lasers and Electro-Optics 2020*, 2020.

[61] K. Mathivanan and P. Plapper. Correlation of optical signal during laser fusion welding of copper to aluminum. *Journal of Laser Applications*, 33(1):012037, 2021.

[62] K. Mathivanan and P. Plapper. Prediction of Cu-Al weld status using convolutional neural network. In *Conference proceeding of Lasers in Manufacturing (LiM), 2021*. WLT, 2021.

[63] K. Mathivanan and P. Plapper. Laser welding of copper to aluminum with spiral trajectory and identification of excessive aluminum melting. *Journal of Laser Applications*, 34(1):012023, 2022.

[64] J. Mazumder. Laser Welding: State of the Art Review. *Jom*, 34(7):16–24, 1982.

[65] W. Meng, X. Yin, J. Fang, L. Guo, Q. Ma, and Z. Li. Dynamic features of plasma plume and molten pool in laser lap welding based on image monitoring and processing techniques. *Optics and Laser Technology*, 109(October 2017):168–177, 2019.

[66] M. Miyagi, H. Wang, R. Yoshida, Y. Kawahito, H. Kawakami, and T. Shoubu. Effect of alloy element on weld pool dynamics in laser welding of aluminum alloys. *Scientific Reports*, 8(1), 2018.

[67] L. Mrňa, P. Horník, P. Jedlička, and J. Pavelka. Study of laser wobbling welding process through the radiation of plasma plume. In *Lasers in Manufacturing Conference 2017*, 2017.

[68] M. P. Mubiayi, E. T. Akinlabi, and M. E. Makhatha. Microstructure evolution and statistical analysis of Al/Cu friction-stir spot welds. *Materiali in Tehnologije*, 51(5):861–869, 2017.

[69] J. L. Murray. The aluminium-copper system. *International Metals Reviews*, 30(1):211–234, 1985.

[70] M. Naeem, A. Montello, and C. Rasmussen. Experimental studies of fiber laser welding of a range of dissimilar material combinations. In *Lasers in Manufacturing (LiM) conference proceeding, Germany*, 2015.

[71] E. C. Ozkat, P. Franciosa, and D. Ceglarek. A Framework for Physics-driven in-process Monitoring of Penetration and Interface Width in Laser Overlap Welding. *Procedia CIRP*, 60(May):44–49, 2017.

[72] E. C. Ozkat, P. Franciosa, and D. Ceglarek. A Framework for Physics-driven in-process Monitoring of Penetration and Interface Width in Laser Overlap Welding. *Procedia CIRP*, 60:44–49, 2017.

[73] L. Pan, P. Li, X. Hao, J. Zhou, and H. Dong. Inhomogeneity of microstructure and mechanical properties in radial direction of aluminum/copper friction welded joints. *Journal of Materials Processing Technology*, 255(January 2018):308–318, 2018.

[74] R. Patwa, H. Herfurth, S. Heinemann, H. Pantsar, B. Regaard, N. Golam, and M. Hailat. Laser Welding and Process Monitoring Applications for Advanced Manufacturing of Batteries and Fuel Cells. *Sheet Metal Welding Conference XIV*, (3):1–14, 2010.

[75] R. Pelzer, M. Nelhiebel, R. Zink, S. Wöhlert, A. Lassnig, and G. Khatibi. High temperature storage reliability investigation of the Al-Cu wire bond interface. *Microelectronics Reliability*, 52(9-10):1966–1970, 2012.

[76] J. E. Pinto-Lopera, J. M. S. Motta, and S. C. A. Alfaro. Real-time measurement of width and height of weld beads in GMAW processes. *Sensors (Switzerland)*, 16(9):1–14, 2016.

[77] N. Ponweiser, C. L. Lengauer, and K. W. Richter. Re-investigation of phase equilibria in the system Al-Cu and structural analysis of the high-temperature phase η1-Al1-δCu. *Intermetallics*, 19(11):1737–1746, 2011.

[78] R. Poprawe. Tailored light 2. *Aachen: Springer Verlag*, 2011.

[79] R. N. Raoelison, T. Sapanathan, N. Buiron, and M. Rachik. Magnetic pulse welding of Al/Al and Al/Cu metal pairs: Consequences of the dissimilar combination on the interfacial behavior during the welding process. *Journal of Manufacturing Processes*, 20(September):112–127, 2015.

[80] J. F. Ready. *Industrial applications of lasers*. Elsevier, 1997.

[81] A. Regensburg, F. Petzoldt, T. Benss, and J. P. Bergmann. Liquid interlayer formation during friction stir spot welding of aluminum/copper. *Welding in the World*, 63(1):117–125, 2019.

[82] A. Regensburg, F. Petzoldt, R. Schürer, P. Hellwig, and J. P. Bergmann. Effect of local preheating during ultrasonic welding of Al-Cu joints on strand compaction and bond formation. *Welding in the World*, 61(3):443–451, 2017.

[83] J. Rudlin, P. D. Bono, and S. Majidnia. Inspection of laser welded electrical connections for car batteries using eddy currents. *11th European Conference on Non-Destructive Testing*, 2014.

[84] T. Sakagawa, S. I. Nakashiba, and H. Hiejima. Laser micro welding system and its application to seam welding of rechargeable battery. *Physics Procedia*, 12(PART 1):6–10, 2011.

[85] P. Schmalen. *Post-process and in-process analysis methods for laser welding of aluminum-copper*. PhD thesis, University of Luxembourg, Luxembourg, 2019.

[86] P. Schmalen and P. Plapper. Spectroscopic studies of dissimilar al-cu laser welding. In *International Manufacturing Science and Engineering Conference*, volume 51364. American Society of Mechanical Engineers, 2018.

[87] F. Schmitt, B. Mehlmann, J. Gedicke, A. Olowinsky, A. Gillner, and R. Poprawe. Laser beam micro welding with high brilliant fiber lasers. *Journal of Laser Micro Nanoengineering*, 5(3):197–203, 2010.

[88] O. Seffer, R. Pfeifer, A. Springer, and S. Kaierle. Investigations on laser beam welding of different dissimilar joints of steel and aluminum alloys for automotive lightweight construction. *Physics Procedia*, 83:383–395, 2016.

[89] M. Seibold, K. Schricker, and J. P. Bergmann. Characterization of optical spectrum in laser beam welding of dissimilar aluminum-copper joints and time-dependent correlation to process stages. 11144:111440U, 2019.

[90] Seiji Katayama. *Handbook of laser welding technologies*. Woodhead Publishing series in electronic and optical materials ; no. 41. 2013.

[91] L. H. Shah, A. Gerlich, and Y. Zhou. Design guideline for intermetallic compound mitigation in Al-Mg dissimilar welding through addition of interlayer. *International Journal of Advanced Manufacturing Technology*, 94(5-8):2667–2678, 2018.

[92] G. Shannon and W. Steen. Investigation of keyhole and melt pool dynamics during laser butt welding of sheet steel using a high speed camera. 1992(1):130–138, 1992.

[93] P. G. Slade. *Electrical contacts: principles and applications*. CRC press, 2017.

[94] W. Sokolowski, J. Beersiek, and E. Beyer. Control of the laser welding process by means of spectroscopic data. (10):505–512, 1992.

[95] T. Solchenbach. *Laserbasierters Schweißlöten von artungleichen Aluminium-Kupfer-Verbindungen*. PhD thesis, University of Luxembourg, Luxembourg, 2014.

[96] T. Solchenbach and P. Plapper. Mechanical characteristics of laser braze-welded aluminium-copper connections. *Optics and Laser Technology*, 54:249–256, 2013.

[97] T. Solchenbach, P. Plapper, M. Greger, J.-L. Biagi, J. Bour, and J. A. S. Bomfim. Thermal and electrical aging of laser braze-welded aluminum–copper interconnects. *Translational Materials Research*, 1(1):015001, 2014.

[98] J. Stavridis, A. Papacharalampopoulos, and P. Stavropoulos. Quality assessment in laser welding: a critical review. *The International Journal of Advanced Manufacturing Technology*, (May), 2017.

[99] A. Stern, V. Shribman, A. Ben-Artzy, and M. Aizenshtein. Interface Phenomena and Bonding Mechanism in Magnetic Pulse Welding. *Journal of Materials Engineering and Performance*, 23(10):3449–3458, 2014.

[100] P. Stritt, C. Hagenlocher, C. Kizler, R. Weber, C. Rüttimann, and T. Graf. Laser spot welding of copper-aluminum joints using a pulsed dual wavelength laser at 532 and 1064 nm. *Physics Procedia*, 56(C):759–767, 2014.

[101] J. Svenungsson, I. Choquet, and A. F. Kaplan. Laser Welding Process - A Review of Keyhole Welding Modelling. *Physics Procedia*, 78(August):182–191, 2015.

[102] P. Taheri, S. Hsieh, and M. Bahrami. Investigating electrical contact resistance losses in lithium-ion battery assemblies for hybrid and electric vehicles. *Journal of Power Sources*, 196(15):6525–6533, 2011.

[103] F. Teichmann, S. Müller, and K. Dilger. On the occurrence of weld bead porosity during laser vacuum welding of high pressure aluminium die castings. *Procedia CIRP*, 74:438–441, 2018.

[104] G. Van Rossum and F. L. Drake Jr. *Python reference manual*. Centrum voor Wiskunde en Informatica Amsterdam, 1995.

[105] B. D. R. Veitía, A. E. Hernández, L. O. Villarinho, M. S. Orozco, A. S. Roca, H. C. Fals, and E. J. Macias. Deep learning for quality prediction in dissimilar spot welding DP600-AISI304, using a convolutional neural network and infrared image processing. *32nd European Modeling and Simulation Symposium, EMSS 2020*, (November):393–399, 2020.

[106] L. Wang, M. Gao, C. Zhang, and X. Zeng. Effect of beam oscillating pattern on weld characterization of laser welding of AA6061-T6 aluminum alloy. *Materials and Design*, 108(July):707–717, 2016.

[107] L. Wang, X. Gao, and Z. Chen. Status analysis of keyhole bottom in laser-mag hybrid welding process. *Opt. Express*, 26(1):347–355, Jan 2018.

[108] X. Wu, T. Liu, and W. Cai. Microstructure, welding mechanism, and failure of Al/Cu ultrasonic welds. *Journal of Manufacturing Processes*, 20:321–331, 2015.

[109] B. Xue, B. Chang, and D. Du. Multi-output monitoring of high-speed laser welding state based on deep learning. *Sensors*, 21(5):1–16, 2021.

[110] L. Yang, B. Mi, L. Lv, H. Huang, X. Lin, and X. Yuan. Formation sequence of interface intermetallic phases of cold rolling Cu/Al clad metal sheet in annealing process. *Materials Science Forum*, 749:600–605, 2013.

[111] Y. Yang, H. Chen, and M. Li. Dissimilar copper-aluminum joint processed by low-temperature nickel electroplating. *Journal of Materials Processing Technology*, 242(April):68–76, 2017.

[112] D. Y. You, X. D. Gao, and S. Katayama. Review of laser welding monitoring. *Science and Technology of Welding and Joining*, 19(3):181–201, 2013.

[113] Y. Zhai, G. Huang, Y. Zhou, and X. Zhou. *High speed imaging analysis of laser welding*, volume 142. 2016.

[114] S. Zhang, J. Sun, M. Zhu, L. Zhang, P. Nie, and Z. Li. Fiber laser welding of hsla steel by autogenous laser welding and autogenous laser welding with cold wire methods. *Journal of Materials Processing Technology*, 275:116353, 2020.

[115] Y. Zhang, D. You, X. Gao, C. Wang, Y. Li, and P. P. Gao. Real-time monitoring of high-power disk laser welding statuses based on deep learning framework. *Journal of Intelligent Manufacturing*, 31(4):799–814, 2020.

[116] Z. Zhang, K. Wang, J. Li, Q. Yu, and W. Cai. Investigation of Interfacial Layer for Ultrasonic Spot Welded Aluminum to Copper Joints. *Scientific Reports*, 7(1):1–6, 2017.

[117] N. Zhao, W. Li, W. W. Cai, and J. A. Abell. A Fatigue Life Study of Ultrasonically Welded Lithium-Ion Battery Tab Joints Based on Electrical Resistance. *Journal of Manufacturing Science and Engineering*, 136(5):051003, 2014.

[118] X. Zhou, G. Zhang, Y. Shi, M. Zhu, and F. Yang. Microstructures and mechanical behavior of aluminum-copper lap joints. *Materials Science and Engineering A*, 705(August):105–113, 2017.

[119] O. Zobac, A. Kroupa, A. Zemanova, and K. W. Richter. Experimental Description of the Al-Cu Binary Phase Diagram. *Metallurgical and Materials Transactions A: Physical Metallurgy and Materials Science*, 2019.

Chapter 10

Appendix

10.1 Summary of the CNN models used

In this appendix the summary of CNN models used in chapter 6 and their shapes after each layer is shown.

Model: N=2 (Two convolutional and pooling layers)

Layer (type)	Output Shape	Param #
conv2d (Conv2D)	(None, 540, 550, 64)	1792
activation (Activation)	(None, 540, 550, 64)	0
max_pooling2d (MaxPooling2D)	(None, 270, 275, 64)	0
conv2d_1 (Conv2D)	(None, 270, 275, 64)	36928
activation_1 (Activation)	(None, 270, 275, 64)	0
max_pooling2d_1 (MaxPooling2	(None, 135, 137, 64)	0
flatten (Flatten)	(None, 1183680)	0
dense (Dense)	(None, 64)	75755584
dense_1 (Dense)	(None, 5)	325
activation_2 (Activation)	(None, 5)	0

Total params: 75,794,629
Trainable params: 75,794,629
Non-trainable params: 0

Figure 10.1: Summary of CNN architecture with two convolutional and poling layers

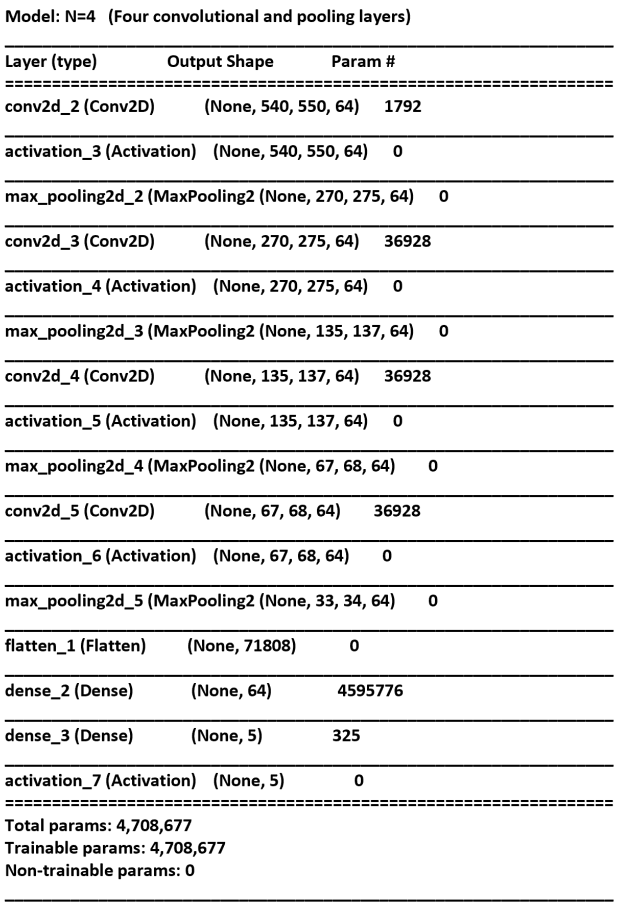

Figure 10.2: Model summary of CNN architecture with four convolutional and poling layers

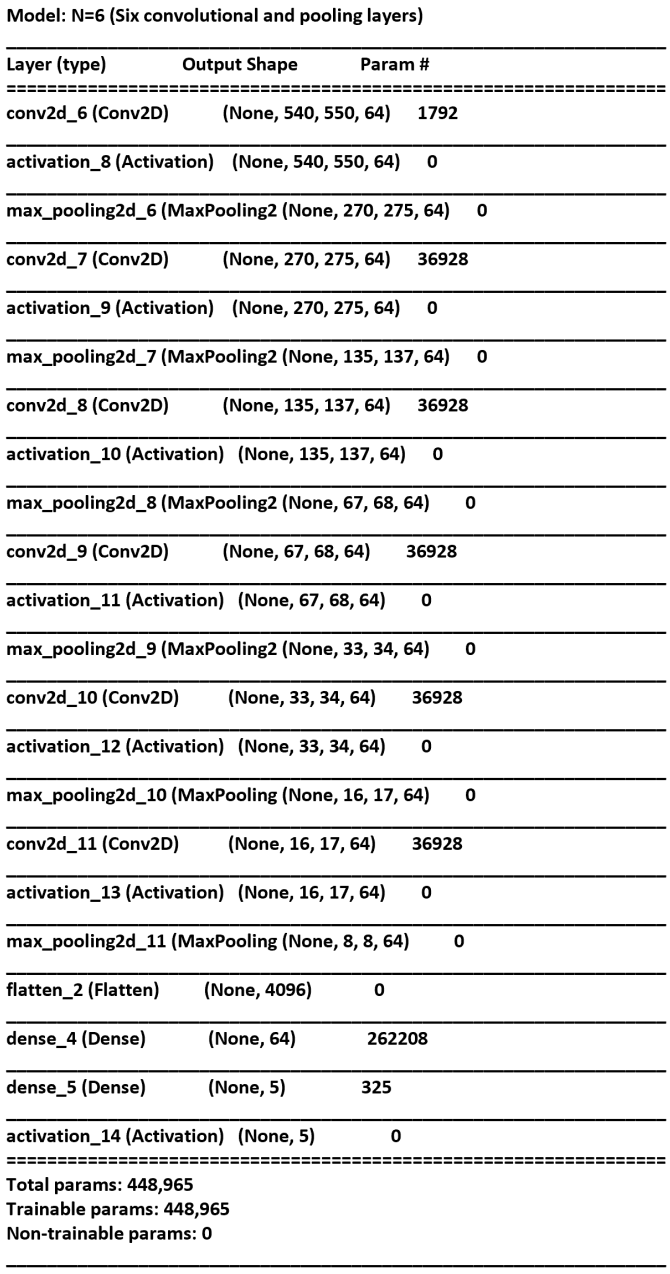

Figure 10.3: Model summary of CNN architecture with six convolutional and poling layers

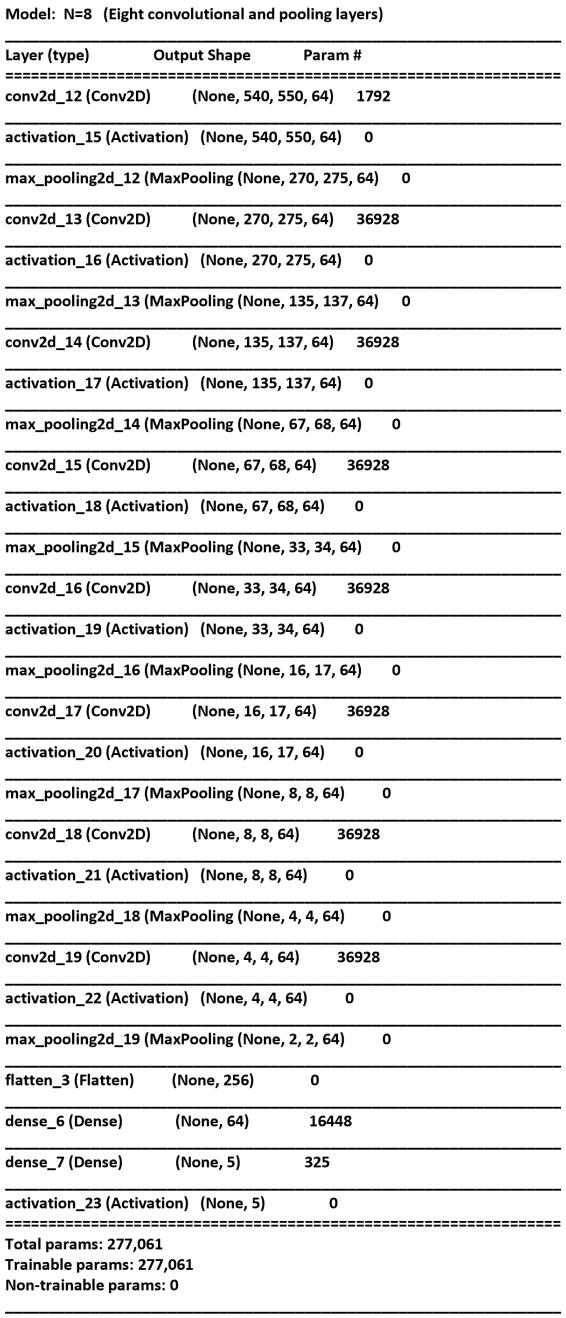

Figure 10.4: Model summary of CNN architecture with eight convolutional and poling layers

10.2 Area and width of the spiral weld at the cross-section

The schematic of the width and area of the weld measured at the cross-section is shown in figure 10.5. The effect of the weld width for different laser velocities is shown in figure 10.6. The effect

of the weld area for different laser velocities is shown in figure 10.7. The width and the area of the weld decrease as the velocity is increased.

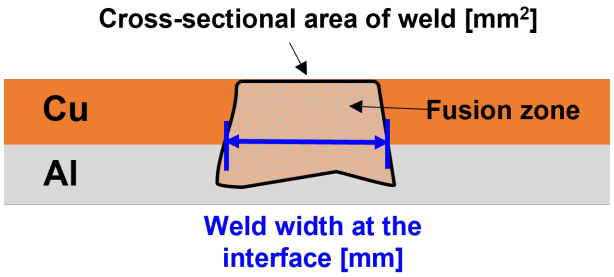

Figure 10.5: Schematic showing the weld area and interface width measured at the weld cross-section

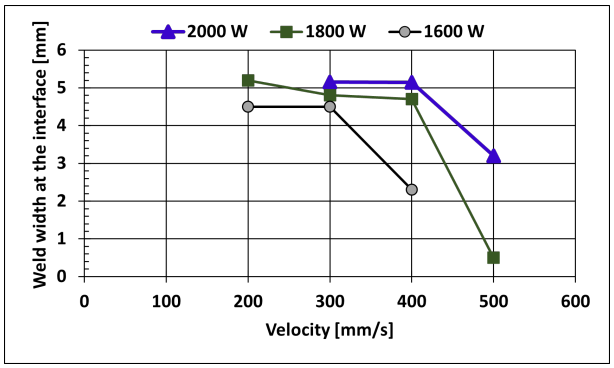

Figure 10.6: Plot of interface width for different laser power and velocity

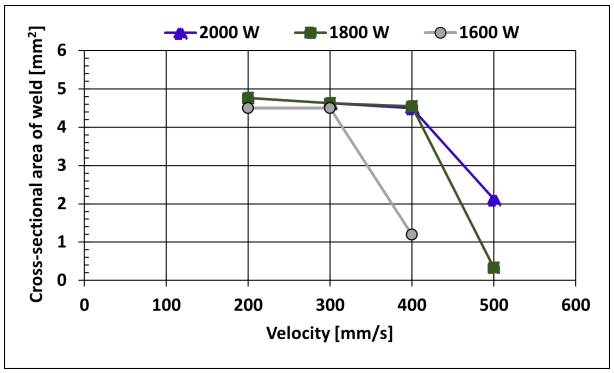

Figure 10.7: Plot of weld area for different laser power and velocity